Title

Designing Vanadium Oxide/Graphene Composite Electrodes for Aqueous Energy Storage Systems

Author

Huang, Ailun

Publication Date

2023

Peer reviewed|Thesis/dissertation

UNIVERSITY OF CALIFORNIA

Los Angeles

Designing Vanadium Oxide/Graphene Composite Electrodes for Aqueous Energy Storage Systems

A dissertation submitted in partial satisfaction of the requirements for the degree Doctor of Philosophy in Chemistry

by

Ailun Huang

2023

ABSTRACT OF THE DISSERTATION

Designing Vanadium Oxide/Graphene Composite Electrodes

for Aqueous Energy Storage Systems

by

Ailun Huang

Doctor of Philosophy in Chemistry

University of California, Los Angeles

Professor Richard B. Kaner, Chair

Energy storage technologies have emerged as a critical component in the sustainable development of the global energy landscape. Aqueous energy storage systems are considered to be a promising solution to reliably store the energy generated from renewable sources and deliver electricity to the grid on demand. From bulk storage to uninterrupted power supply, large-scale energy storage systems of various power capacity and discharge frequency are needed, requiring rational designs of different electrochemical systems. In this work, unconventional high-energy-density supercapacitors and innovative fast-charging batteries are explored. Utilizing a facile laser scribing fabrication approach, earth-abundant, low-cost, electrochemically active vanadium oxides are incorporated onto highly conductive graphene scaffold. Symmetric supercapacitors based on this composite electrode exhibit high energy densities that are close to conventional batteries.

Furthermore, with synthetic modifications, the vanadium oxides/graphene composite is applied as the cathode material in a zinc-ion battery, leading to state-of-the-art rate capability and high-rate cycling stability. Moreover, the synthesis and charge storage mechanism of the pseudocapacitive electrode are further investigated in an aqueous hybrid Li-ion battery.

The dissertation of Ailun Huang is approved.

Xiangfeng Duan

William M. Gelbart

Chong Liu

Richard B. Kaner, Committee Chair

University of California, Los Angeles

2023

Dedicated to my dearest parents

Table of Contents

List of Figures

List of Tables

Acknowledgement

First of all, I would like to express my sincere gratitude to my research advisor, Prof. Richard Kaner for always supporting my work and encouraging me to purse my research interests. I would also like to thank my committee members Prof. Xiangfeng Duan, Prof. Willam Gelbart, and Prof. Chong Liu for their advice and gudiance througout my PhD journey.

I am very grateful to Dr. Maher El-Kady, Dr. Mit Muni and Dr. Haosen Wang for their generous help when I started on my initial projects in the Kaner Lab. I would also like to thank Xueying Chang and Dr. Cheng-Wei Lin for being my wonderful friends and collegues. My gratitude also goes to my coauthors Dr. Mackenzie Anderson, Dr. Chris Turner and Zhiyin Yang for kindly helping me with my research projects. I am also thankful to my collaborators Bo Liu and Prof. Yuzhang Li for working with me on the zinc-ion battery project. I would like also to thank Dr. Ignacio Martini and Dr. Sergey Prikhodko who have provided me with training and support for multiple characterization tools.

Additionally, I would like to thank the Department of Chemistry and Biochemistry and UCLA Graduate Division for the finnancial support in the forms of Jim and Barbara Tsay Excellence in Second Year Research and Academics Award and Dissertation Year Fellowship.

Finally, I would like to thank my parents who have always encourged me to purse my dreams and supported me unconditionally.

Chapter 2 is reprinted (adapted) from Huang, A.; El-Kady, M. F.; Chang, X.; Anderson, M.; Lin, C.-W.; Turner, C. L.; Kaner, R. B. (2021). Facile Fabrication of Multivalent VO_x/Graphene Nanocomposite Electrodes for High-Energy-Density Symmetric Supercapacitors. *Advanced Energy Materials*, *11*(26), 2100768. https://doi.org/10.1002/aenm.202100768. Copyright (2021) John Wiley and Sons. A.H. collected most of the data and wrote the initial manuscript. All authors contributed to this work.

Chapter 3 is a version of Liu, B.; Huang, A; Yuan, X.; Chang, X.; Yang, Z; Lyle, K.; Kaner, R. B.; Li, Y. "A Laser-Scribed Vanadium Oxide Cathode for Ultra-Fast Zinc-Ion Energy Storage". B.L. and A.H. contributed equally to this work. B.L, A.H., R.B.K., and Y.L. conceived the ideas and wrote the manuscript. B.L. and A.H. designed the research under the guidance of R.B.K. and Y.L. and performed data analysis. B.L. carried out the electrochemical experiments, collected TEM and XRD data. A.H. designed and performed the synthesis of materials, and did the Raman, SEM and TGA measurements. X.Y. helped with the electrochemical experiments, TEM, XPS, and Raman. X.C. collected the XPS data. X.Y. and X.C. were involved in general discussions. Z.Y. helped with the synthesis of materials. K.L. prepared samples for characterizations.

Chapter 4 is a version of Huang, A; Yang, Z; Chang, X.; Lin, C.-W.; Kaner, R. B.; Li, Y. "Nanoengineered Vanadium Oxide Composite as High-performance Anode for Aqueous Li-ion Hybrid Battery ". A.H. and Z.Y. contributed equally to this work. A.H. designed the experiments and collected SEM, XRD and Raman data. Z.Y. carried out the synthesis and the electrochemical experiments. X.C. collected the XPS data. C.-W.L. collected TEM data. All authors were involved in discussions about this work. A.H. and R.B.K. wrote the manuscript.

Vita

2018 - 2023	Graduate Student with Prof. Richard B. Kaner
	University of California, Los Angeles
	Los Angeles, California
2022 - 2023	Dissertation Year Fellowship
	University of California, Los Angeles
	Los Angeles, California
2021	Excellence in Second Year Research and Academics Award
	University of California, Los Angeles
	Los Angeles, California
2014 - 2018	Master of Natural Sciences and Bachelor of Arts
	University of Cambridge
	Cambridge, United Kingdom

List of Publications

1. Chang, X.; Yang, Z.; Huang, A.; Katsuyama, Y.; Lin, C.; El-Kady, M. F.; Wang, C.; Kaner, R. B. Understanding the Degradation Mechanisms of Conducting Polymer Supercapacitors. *Macromol. Rapid Commun.* **2023**, *135* (4). https://doi.org/10.1002/marc.202300237.
2. Chang, X.; Lin, C. W.; Huang, A.; El-Kady, M. F.; Kaner, R. B. Molecular Engineering of Hierarchical Conducting Polymer Composites for Highly Stable Supercapacitors. *Nano Lett.* **2023**. https://doi.org/10.1021/acs.nanolett.3c00284.
3. Chang, X.; El-Kady, M. F.; Huang, A.; Lin, C. W.; Aguilar, S.; Anderson, M.; Zhu, J. Z. J.; Kaner, R. B. 3D Graphene Network with Covalently Grafted Aniline Tetramer for Ultralong-Life Supercapacitors. *Adv. Funct. Mater.* **2021**, *31* (32), 2102397. https://doi.org/ 10.1002/adfm.202102397.
4. Huang, A.; El-Kady, M. F.; Chang, X.; Anderson, M.; Lin, C.; Turner, C. L.; Kaner, R. B. Facile Fabrication of Multivalent VO x /Graphene Nanocomposite Electrodes for High-Energy-Density Symmetric Supercapacitors. *Adv. Energy Mater.* **2021**, *11* (26), 2100768. https://doi.org/10.1002/aenm.202100768.
5. Wang, C.; Muni, M.; Strauss, V.; Borenstein, A.; Chang, X.; Huang, A.; Qu, S.; Sung, K.; Gilham, T.; Kaner, R. B. Graphene's Role in Emerging Trends of Capacitive Energy Storage. *Small*. December 28, 2021, p 2006875. https://doi.org/10.1002/smll.202006875.
6. Kasap, H.; Achilleos, D. S.; Huang, A.; Reisner, E. Photoreforming of Lignocellulose into H 2 Using Nanoengineered Carbon Nitride under Benign Conditions. *J. Am. Chem. Soc.* **2018**, *140* (37), 11604–11607. https://doi.org/10.1021/jacs.8b07853.
7. Reeve, H. A.; Ash, P. A.; Park, H.; Huang, A.; Posidias, M.; Tomlinson, C.; Lenz, O.; Vincent, K. A. Enzymes as Modular Catalysts for Redox Half-Reactions in H 2 -Powered

Chemical Synthesis: From Biology to Technology. *Biochem. J.* **2017**, *474* (2), 215–230. https://doi.org/10.1042/BCJ20160513.

Chapter 1. Introduction

Fossil fuels have been the predominant energy source of human activities for hundreds of years. In December 2021, the 26th United Nations Climate Change Conference (COP26) in Glasgow historically called for the accelerated phasing-out of nonrenewable fossil fuels, emphasizing the scientific imperative to switch to clean energy structures.[1] Unfortunately, many types of renewable energy such as solar, wind, and geothermal power are easily affected by unforeseen weather conditions and their generation cannot be synchronized with demand; therefore, it is critical to couple suitable energy storage technologies with these power sources to enable timely and ample energy supplies. Currently, pumped hydropower remains the primary gird-scale energy storage technology owing to its large power capacity and its low cycle cost; however, due to restraints such as large capital cost, long lead time, and large land usage, alternative solutions are being actively explored.[2–5] Among recent installations, electrochemical energy storage systems, led by the most mature lithium-ion battery (LIB) technologies, have emerged as the most popular choice.[6–9] In contrast to mobile energy storage requirements, low cost, and high safety are the most valued criteria for stationary energy storage. Thus, there is a pressing need for the development of high-performance aqueous electrochemical energy storage systems.

Based on power capacity and discharge time, the utilization of electrochemical energy storage systems can be roughly divided into the following: uninterrupted power supply (UPS), transmission and distribution grid support, and bulk power management.[10] Traditionally, energy storage devices are categorized into capacitor-type and battery-type systems where the former possess high specific power, but low specific energy, while the latter can obtain high specific energy, but low specific power. High-energy-density supercapacitors and fast-charging aqueous batteries are considered to bridge the gap between the two extremes. For both systems, it is critical

to rationally design electrodes with high specific capacitance/capacity and fast charge storage kinetics. In this work, vanadium oxides are extensively explored as a promising candidate for aqueous supercapacitors, zinc ion batteries (ZIBs), and LIBs. Vanadium oxides are attractive electrode materials due to their abundance in the earth's crust, diverse crystal structures, and multiple accessible oxidation states.[11] The availability of +2 to +5 valence states can potentially enable multielectron redox couples, showing great potential for capacitance/capacity. Nevertheless, vanadium oxides have a high intrinsic resistance, and the diffusion in the bulk structure is slow; hence, integration with conductive materials and design of favorable nanostructures are the essential strategies to improve the electrochemical performance of vanadium oxides. Prior work by former lab members showed that a mixture of a transition metal chloride precursor with graphite oxide can be made into transition metal oxide nanoparticles on a reduced graphene oxide (rGO) scaffold upon exposure to a laser.[12–14] The previous electrodes created from attempts with transition metals such as Ru, Fe, and Co exhibited high capacitance as supercapacitor electrodes. Herein, starting from this established synthetic approach, vanadium oxides/rGO composites are extensively explored as high-performance electrode materials in supercapacitor,[15] ZIB and aqueous LIB systems.

Chapter 2 attempts to address one of the major challenges in supercapacitors, which is their relatively low energy densities.[16–19] A hybrid electrode based on multivalent vanadium oxides (VO_x) and a graphene network was designed and synthesized via a modified laser-scribing process. The graphene/VO_x electrodes exhibited a large potential window with a high three-electrode specific capacitance of 1110 F g^{-1}, and the aqueous symmetric supercapacitors (SSCs) can reach a high energy density of 54 Wh kg^{-1} with virtually no capacitance loss after 20,000 cycles. Moreover, the SSC is readily compatible with polymer gel electrolytes and the voltage window of the quasi-

solid-state device can be further extended to 1.5 V, resulting in a remarkable energy density of 72 Wh kg^{-1}, or 7.7 mWh cm^{-3}, outperforming many commercial devices. With a charge transfer resistance of < 0.02 Ω and Coulombic efficiency close to 100%, these flexible SSCs can retain 92% of their capacitance after 20,000 cycles. This designed synthetic approach enables the direct fabrication of electrochemically active films that can be integrated with essentially any substrate including silicon wafers and large-area flexible substrates, showing great promise for next-generation large-area flexible displays and wearable electronic devices.

Aqueous zinc-ion batteries are promising solutions for grid-scale energy storage, but it remains difficult to find high-performance cathodes that simultaneously possess high specific capacity, fast charging capability, and long cycle life.[20–23] In **Chapter 3**, a laser-scribed nano-vanadium oxide (LNVO) was designed as a ZIB cathode material. The charge-storage processes of the LNVO are confined to the surface due to its small grain size and fast kinetics, and Faradaic responses are observed in electrochemical measurements. The LNVO/Zn battery shows a high specific capacity of 490 mAh g^{-1} at 0.5 A g^{-1} and impressively 54% (264 mAh g^{-1}) can be retained at 100 A g^{-1} within a 10 s cycle, showing excellent rate capability. An outstanding cycle life of >90% capacity retention after 3000 cycles was reached at 30 A g^{-1}, and remarkable high energy (396 Wh kg^{-1}) and power densities (56,306 W kg^{-1}) were obtained. The mechanism of the system was also thoroughly studied, revealing a hydronium-ion-facilitated zinc ion co-insertion. Furthermore, the system showed great temperature tolerance, and mechanical flexibility can be achieved when integrated with a polymer gel electrolyte. Overall, the LNVO/Zn system demonstrates great promise for practical large-scale energy storage applications.

Chapter 4 further investigates the electrochemical behaviors of pseudocapacitive electrodes when they are applied in a battery system. With developed manufacturing processes, aqueous LIBs are

attractive solutions for stationary energy storage; however, the advance of aqueous LIBs is hindered by lack of anode materials with high capacity.[24–28] A pseudocapacitive V_2O_5/graphene composite synthesized via a novel laser-scribing/calcination approach was studied as a highly functional anode material for aqueous LIBs. The V_2O_5/graphene anode shows an outstanding specific capacity of 158 mAh g^{-1} in three-electrode measurements. When the V_2O_5/graphene anode is paired with an $LiMn_2O_4$ cathode, the charge storage mechanism of the full cell is revealed to be predominantly surface-controlled, resulting in remarkable rate performance. Specifically, the full cell can reach a specific capacity of 151 and 107 mAh (g anode)$^{-1}$ at C/6 and 2 C, respectively. Moreover, this hybrid battery can achieve high power and an energy density of 650 W kg^{-1} (at 15.6 Wh kg^{-1}) and 81.5 Wh kg^{-1} at (13.6 W kg^{-1}), respectively, outperforming most aqueous LIBs reported in the literature. This innovative strategy provides a pathway to incorporate pseudocapacitive electrodes for improving aqueous lithium-ion storage systems, enabling safe operations of large-scale energy storage without compromising electrochemical performance.

References

(1) United Nations Climate Change Conference. *COP26 The Glasgow Climate Pact*; Glasgow, 2021. https://ukcop26.org/wp-content/uploads/2021/11/COP26-Presidency-Outcomes-The-Climate-Pact.pdf.

(2) Kebede, A. A.; Kalogiannis, T.; Van Mierlo, J.; Berecibar, M. A Comprehensive Review of Stationary Energy Storage Devices for Large Scale Renewable Energy Sources Grid Integration. *Renewable and Sustainable Energy Reviews* **2022**, *159*, 112213. https://doi.org/10.1016/J.RSER.2022.112213.

(3) Li, X.; Wang, S. A Review on Energy Management, Operation Control and Application Methods for Grid Battery Energy Storage Systems. *CSEE Journal of Power and Energy Systems* **2019**, *7* (5), 1026–1040. https://doi.org/10.17775/CSEEJPES.2019.00160.

(4) Castillo, A.; Gayme, D. F. Grid-Scale Energy Storage Applications in Renewable Energy Integration: A Survey. *Energy Convers Manag* **2014**, *87*, 885–894. https://doi.org/10.1016/J.ENCONMAN.2014.07.063.

(5) Argyrou, M. C.; Christodoulides, P.; Kalogirou, S. A. Energy Storage for Electricity Generation and Related Processes: Technologies Appraisal and Grid Scale Applications. *Renewable and Sustainable Energy Reviews* **2018**, *94*, 804–821. https://doi.org/10.1016/j.rser.2018.06.044.

(6) Schoenfisch, M.; Dasgupta, A. *Grid-Scale Storage*. IEA. https://doi.org/License: CC BY 4.0.

(7) Lawder, M. T.; Suthar, B.; Northrop, P. W. C.; De, S.; Hoff, C. M.; Leitermann, O.; Crow, M. L.; Santhanagopalan, S.; Subramanian, V. R. Battery Energy Storage System (BESS) and Battery Management System (BMS) for Grid-Scale Applications. *Proceedings of the IEEE* **2014**, *102* (6), 1014–1030. https://doi.org/10.1109/JPROC.2014.2317451.

(8) Zhu, Z.; Jiang, T.; Ali, M.; Meng, Y.; Jin, Y.; Cui, Y.; Chen, W. Rechargeable Batteries for Grid Scale Energy Storage. *Chem Rev* **2022**, *122* (22), 16610–16751. https://doi.org/10.1021/acs.chemrev.2c00289.

(9) Liu, J.; Zhang, J.-G.; Yang, Z.; Lemmon, J. P.; Imhoff, C.; Graff, G. L.; Li, L.; Hu, J.; Wang, C.; Xiao, J.; Xia, G.; Viswanathan, V. V.; Baskaran, S.; Sprenkle, V.; Li, X.; Shao, Y.; Schwenzer, B. Materials Science and Materials Chemistry for Large Scale Electrochemical Energy Storage: From Transportation to Electrical Grid. *Adv Funct Mater* **2013**, *23* (8), 929–946. https://doi.org/10.1002/adfm.201200690.

(10) Dunn, B.; Kamath, H.; Tarascon, J.-M. Electrical Energy Storage for the Grid: A Battery of Choices. *Science (1979)* **2011**, *334* (6058), 928–935. https://doi.org/10.1126/science.1212741.

(11) Xu, X.; Xiong, F.; Meng, J.; Wang, X.; Niu, C.; An, Q.; Mai, L.; Xu, X.; Xiong, F.; Meng, J.; Niu, C.; An, Q.; Mai, L.; Wang, X. Vanadium-Based Nanomaterials: A Promising Family for Emerging Metal-Ion Batteries. *Adv Funct Mater* **2020**, *30* (10), 1904398. https://doi.org/10.1002/ADFM.201904398.

(12) Hwang, J. Y.; El-Kady, M. F.; Li, M.; Lin, C. W.; Kowal, M.; Han, X.; Kaner, R. B. Boosting the Capacitance and Voltage of Aqueous Supercapacitors via Redox Charge

Contribution from Both Electrode and Electrolyte. *Nano Today* **2017**, *15*, 15–25. https://doi.org/10.1016/j.nantod.2017.06.009.

(13) Li, M.; El-Kady, M. F.; Hwang, J. Y.; Kowal, M. D.; Marsh, K.; Wang, H.; Zhao, Z.; Kaner, R. B. Embedding Hollow Co3O4 Nanoboxes into a Three-Dimensional Macroporous Graphene Framework for High-Performance Energy Storage Devices. *Nano Res* **2018**, *11* (5), 2836–2846. https://doi.org/10.1007/s12274-017-1914-7.

(14) Hwang, J. Y.; El-Kady, M. F.; Wang, Y.; Wang, L.; Shao, Y.; Marsh, K.; Ko, J. M.; Kaner, R. B. Direct Preparation and Processing of Graphene/RuO2 Nanocomposite Electrodes for High-Performance Capacitive Energy Storage. *Nano Energy* **2015**, *18*, 57–70. https://doi.org/10.1016/j.nanoen.2015.09.009.

(15) Huang, A.; El-Kady, M. F.; Chang, X.; Anderson, M.; Lin, C.; Turner, C. L.; Kaner, R. B. Facile Fabrication of Multivalent VO x /Graphene Nanocomposite Electrodes for High-Energy-Density Symmetric Supercapacitors. *Adv Energy Mater* **2021**, *11* (26), 2100768. https://doi.org/10.1002/aenm.202100768.

(16) Poonam; Sharma, K.; Arora, A.; Tripathi, S. K. Review of Supercapacitors: Materials and Devices. *J Energy Storage* **2019**, *21*, 801–825. https://doi.org/10.1016/j.est.2019.01.010.

(17) Simon, P.; Gogotsi, Y.; Dunn, B. Where Do Batteries End and Supercapacitors Begin? *Science*. American Association for the Advancement of Science March 14, 2014, pp 1210–1211. https://doi.org/10.1126/science.1249625.

(18) Noori, A.; El-Kady, M. F.; Rahmanifar, M. S.; Kaner, R. B.; Mousavi, M. F. Towards Establishing Standard Performance Metrics for Batteries, Supercapacitors and Beyond. *Chem Soc Rev* **2019**, *48* (5), 1272–1341. https://doi.org/10.1039/C8CS00581H.

(19) Shao, Y.; El-Kady, M. F.; Sun, J.; Li, Y.; Zhang, Q.; Zhu, M.; Wang, H.; Dunn, B.; Kaner, R. B. Design and Mechanisms of Asymmetric Supercapacitors. *Chem Rev* **2018**, *118* (18), 9233–9280. https://doi.org/10.1021/acs.chemrev.8b00252.

(20) Yan, M.; Ni, H.; Pan, H. Rechargeable Mild Aqueous Zinc Batteries for Grid Storage. *Advanced Energy and Sustainability Research* **2020**, *1* (1), 2000026. https://doi.org/10.1002/aesr.202000026.

(21) Fang, G.; Zhou, J.; Pan, A.; Liang, S. Recent Advances in Aqueous Zinc-Ion Batteries. *ACS Energy Lett* **2018**, *3* (10), 2480–2501. https://doi.org/10.1021/acsenergylett.8b01426.

(22) Chen, D.; Lu, M.; Cai, D.; Yang, H.; Han, W. Recent Advances in Energy Storage Mechanism of Aqueous Zinc-Ion Batteries. *Journal of Energy Chemistry* **2021**, *54*, 712–726. https://doi.org/10.1016/j.jechem.2020.06.016.

(23) Shin, J.; Choi, J. W. Opportunities and Reality of Aqueous Rechargeable Batteries. *Adv Energy Mater* **2020**, *10* (28), 2001386. https://doi.org/10.1002/aenm.202001386.

(24) Zuo, W.; Li, R.; Zhou, C.; Li, Y.; Xia, J.; Liu, J. Battery-Supercapacitor Hybrid Devices: Recent Progress and Future Prospects. *Advanced Science* **2017**, *4* (7), 1600539. https://doi.org/10.1002/advs.201600539.

(25) Chen, S.; Zhang, M.; Zou, P.; Sun, B.; Tao, S. Historical Development and Novel Concepts on Electrolytes for Aqueous Rechargeable Batteries. *Energy Environ Sci* **2022**, *15* (5), 1805–1839. https://doi.org/10.1039/D2EE00004K.

(26) Ao, H.; Zhao, Y.; Zhou, J.; Cai, W.; Zhang, X.; Zhu, Y.; Qian, Y. Rechargeable Aqueous Hybrid Ion Batteries: Developments and Prospects. *J Mater Chem A Mater* **2019**, *7* (32), 18708–18734. https://doi.org/10.1039/C9TA06433H.

(27) Ju, Z.; Zhao, Q.; Chao, D.; Hou, Y.; Pan, H.; Sun, W.; Yuan, Z.; Li, H.; Ma, T.; Su, D.; Jia, B. Energetic Aqueous Batteries. *Adv Energy Mater* **2022**, *12* (27), 2201074. https://doi.org/10.1002/aenm.202201074.

(28) Wang, Y.; Yi, J.; Xia, Y. Recent Progress in Aqueous Lithium-Ion Batteries. *Adv Energy Mater* **2012**, *2* (7), 830–840. https://doi.org/10.1002/aenm.201200065.

Chapter 2. Facile Fabrication of Multivalent VO_x/Graphene Nanocomposite Electrodes for High-Energy-Density Symmetric Supercapacitors

Abstract

Supercapacitors have emerged as one of the leading energy-storage technologies due to their short charge/discharge time and exceptional cycling stability; however, the state-of-the-art energy density is relatively low. Hybrid electrodes based on transition metal oxides and carbon-based materials are considered as promising candidates to overcome this limitation. Herein, we propose a rational design of graphene/VO_x electrodes that incorporate vanadium oxides with multiple oxidation states onto highly conductive graphene scaffolds synthesized via a facile laser-scribing process. The graphene/VO_x electrodes exhibit a large potential window with a high three-electrode specific capacitance of 1110 F/g. The aqueous graphene/VO_x symmetric supercapacitors (SSCs) can reach a high energy density of 54 Wh/kg with virtually no capacitance loss after 20,000 cycles. Moreover, the flexible quasi-solid-state graphene/VO_x SSCs can reach a very high energy density of 72 Wh/kg, or 7.7 mWh/cm^3, outperforming many commercial devices. With $R_{ct} < 0.02$ Ω and Coulombic efficiency close to 100%, these gel graphene/VO_x SSCs can retain 92% of their capacitance after 20,000 cycles. The process enables the direct fabrication of redox-active electrodes that can be integrated with essentially any substrates including silicon wafers and flexible substrates, showing great promise for next-generation large-area flexible displays and wearable electronic devices.

Introduction

Supercapacitors have been a prevalent area of research during the past decade due to their remarkable high power density and long cycle life.[1–5] Although supercapacitors are considered to bridge the gap between traditional capacitor-type and battery-type electrochemical charge storage devices, the relatively low energy density of supercapacitors remains as their major impediment to be widely utilized in commercial applications. The energy density of a device is directly proportional to its specific capacitance and the square of the operating voltage. Therefore, a rational design to efficiently improve supercapacitor energy density must aim to maximize both. Electric double-layer capacitance (EDLC) and pseudocapacitance are the two charge/discharge mechanisms that supercapacitors rely on. The former comes from the physical accumulation of electrostatic charge at the electrode-electrolyte interface, and the latter depends on fast Faradaic reactions that occur at or near the electrode surface. Thus, to achieve the best possible electrochemical performance, the electrode should be a hybrid material with not only a structure of high specific area, but also a redox-active chemical composition, taking advantage of both capacitive processes.

The theoretical specific capacitance of a pseudocapacitive electrode is proportional to the number of electrons involved in a specific redox reaction. Transition metal oxides with fast and reversible redox couples are excellent candidates for pseudocapacitors, and many have been verified to show pseudocapacitive behavior, such as RuO_2,[6] MnO_2,[7] Co_3O_4,[8] and Fe_3O_4.[9] While most transition metal oxides only have two interconvertible oxidation states, vanadium oxides possess four readily accessible valence states (II-V), making them especially promising for high pseudocapacitance. Among all types of vanadium oxides, V_2O_5 has been studied the most for energy storage

applications;[10–15] however, there are benefits to employing mixed-valence vanadium oxides (VO_x), since VO_2 and V_2O_3 have higher electrical conductivities than V_2O_5[16] and the pre-existing multiple oxidation states are likely to provide a larger electrochemical active potential window.[17,18] For example, Yu *et al.* reported a valence optimized VO_x electro-oxidized from V_2O_3 that increased its potential window from 0.5 V for pure V_2O_3 to 0.8 V after their electro-oxidized modification.[19] Although vanadium oxides are earth-abundant and economical, they still have relatively high resistivity in comparison to the much more expensive RuO_2. A common approach to compensate for the poor conductivity of pseudocapacitive vanadium oxides is the incorporation of carbon-based materials, e.g. reduced graphene oxide (rGO),[16,20–25] carbon nanotubes (CNT),[26,27] activated carbon,[17,28] etc. These highly conductive carbonaceous materials generally exhibit EDLC behavior, thus, it is favorable to adopt high porosity morphologies so that the specific active area for storing charge at the electrode surface can be maximized. The synthesis of a carbon-vanadium oxide composite is typically a multi-step process that involves either separate pre-functionalization of the carbon-based material or post-assembly high-temperature modification via solvothermal treatment or calcination. For instance, Wu *et al.* developed a micelle-assisted synthesis of V_2O_3@C composites in which the vanadate coats the pre-treated activated carbon and subsequently undergoes calcination, attaining a specific capacitance of 205 F g^{-1} with a 1 V window.[28] Despite the delicate core-shell designs, the electrode exhibited a large charge transfer resistance (R_{ct}) of 16.3 Ω, a long time constant of ~32 s, and the power density fell below 20 W kg^{-1} at the maximum energy density. Evidently, it is challenging to obtain a high-performance composite electrode with good electronic and ionic conductivity without a three-dimensional charge transfer network.[29] Li *et al.* reported a self-assembled rGO/V_2O_5 aerogel symmetric supercapacitor possessing 68 W h kg^{-1} at a power density of 250 W kg^{-1}; however, the synthesis required a 2-day gelation followed

by freeze-drying and thermal annealing.[30] Also, the addition of binder is required to maintain the structural integrity of the electrode and the electrochemical measurements were done in the voltage range of –1 V to 1 V, which is impractical for commercial devices. In our previous work, we showed a simple one-step laser-scribing process that can reliably produce porous laser-scribed graphene (LSG) thin films and simultaneously yield metal oxides.[31,32] The as-synthesized LSG network can provide a highly conductive EDLC scaffold for the nanosized VO_x particles, due to its electrical semi-metallicity and mechanical rigidity.

In this work, we report an LSG/VO_x nanocomposite hybrid electrode synthesized via a facile laser-scribing process from graphite oxide (GO) and VCl_3 precursors. Mediated by the Coulombic attraction between the negatively charged oxygen surface groups and positively charged vanadium cations, the VO_x nanoparticles are directly anchored onto the 3D LSG scaffold. This enables both the pseudocapacitive and the EDLC components to be readily accessible to the electrolyte. The high local temperature generated during laser-scribing simultaneously accomplishes the reduction of GO and the entropy-driven formation of multivalent VO_x. By starting from the low-valent V(III) precursor, the composition of the as-synthesized VO_x is dominated by the relatively less resistive V_2O_3, and with the incorporation of the LSG network, the LSG/VO_x nanocomposite electrode can obtain a high specific capacitance of 1110 F g^{-1} with a very small R_{ct} in a three-electrode setup. The LSG/VO_x electrode has a large electrochemically active potential window and can be assembled into aqueous symmetric supercapacitors (SSCs) with a 1.3 V window, accredited to the presence of multiple oxidation states. The LSG/VO_x SSCs can attain a high energy density of 54 Wh kg^{-1} at a power density of 894 W kg^{-1} with outstanding capacitance retention of 112% after 20,000 cycles. Furthermore, quasi-solid-state LSG/VO_x SSCs with a gel electrolyte were also

fabricated to increase the operating voltage. With R_{ct} < 0.02 Ω and Coulombic efficiency close to 100% at all scan rates, the 1.5 V flexible gel LSG/VO_x SSC reached a high energy density of 72 Wh kg^{-1} at a power density of 370 W kg^{-1} with excellent capacitance retention of 92% after 20,000 cycles, placing it as one of the best-performing systems among those reported in the literature. Both LSG/VO_x SSCs also demonstrate superior volumetric energy storage behavior in comparison to commercial devices.

Results and Discussions

Fabrication of LSG/VO_x composite electrodes

The laser-scribed graphene (LSG)/VO_x composite was synthesized by a laser-scribing process in which the reduction of GO and the conversion of VCl_3 to VO_x take place simultaneously. A solution of precursor VCl_3 was gradually added to a GO suspension at a controlled rate through a syringe pump to create a stable mixture of GO/VCl_3. The GO acts as a framework to prevent the aggregation of vanadium species, while the vanadium particles serve as spacers to hinder the restacking of GO sheets due to the attractive Coulombic forces between V^{3+} and the negatively charged GO surfaces. The dried film then underwent laser-scribing by a CO_2 laser under ambient atmosphere, instantaneously yielding VO_x and structurally expanded LSG due to the locally induced heat that expels gaseous byproducts such as H_2O and CO_2.[33] The as-synthesized LSG/VO_x composite films were used as electrodes without further processing (**Figure 2-1.**a). The concentration of the VCl_3 solution was varied to find the optimal loading for the composite electrodes.

As shown in **Figure 2-1.b-c**, the LSG/VO_x composite can readily be scaled up and coated onto large-area substrates such as a silicon wafer and an A5-size graphite paper, enabling the design of micro-supercapacitor arrays as previously reported.[29] To contrast the composite film before and after laser irradiation, the mixture was coated onto a clear polyethylene terephthalate (PET) substrate, illustrating that the dark violet film turns completely black upon exposure to the laser (**Figure 2-1.d**).

Material characterization of LSG/VO_x composite

The structure and morphology of the LSG/VO_x composite were characterized by scanning electron microscopy (SEM) and transmission electron microscopy (TEM). In comparison to the SEM images of the unprocessed GO/VCl_3 film (**Figure S2-1.**), **Figure 2-2.a** and **Figure S2-2.** show the typical morphology of rGO with flakes and wrinkles, confirming the successful reduction of GO by the laser-scribing process. Under higher magnification, **Figure 2-2.b** demonstrates that the VO_x particles are uniformly coated over the 3D LSG scaffold, providing numerous pathways for charge transfer. The network that is created upon laser reduction provides diffusion pathways for the intercalation of electrolyte cations. It is also evident that the restacking of rGO sheets is effectively inhibited by the VO_x nano-spacers. As revealed by TEM images, the evenly distributed VO_x particles are tightly bonded to the LSG surfaces; this is expected as the vanadium cations are attracted to the negatively charged LSG oxygen functional groups. Although the density of the VO_x particles on the LSG sheet is high, the highly conductive graphene surfaces remain accessible for charge transfer from/to the electrolyte (**Figure 2-2.c**). While some VO_x exists as individual nanoparticles with a mean size of ~25 nm (**Figure S2-3.**), a significant proportion of them exist as

connected networks of VO_x (**Figure 2-2.d**). This is likely the result of both the high concentration of VCl_3 precursor and the high local temperature induced by the CO_2 laser.

The vanadium valence states present in the LSG/VO_x composite were analyzed by X-ray powder diffraction (XRD) and X-ray photoelectron spectroscopy (XPS). The strong diffraction peaks in the XRD pattern (**Figure 2-2.e**) of the LSG/VO_x nanocomposite suggest the presence of vanadium oxides. Specifically, the sharp peaks at 24.4°, 33.2°, 36.4°, and 54.2° can be indexed to the (012), (104), (110) and (116) of karelianite V_2O_3 with the rhombohedral corundum-type structure, indicating that it is the major vanadium oxide species present. There is also a much smaller amount of VO_2 present, and the remaining proportion consists of several non-stoichiometric vanadium oxides. Compared to the weakly diffracting GO/VCl_3 mixture that only shows a significant (002) graphitic peak at 26.4° (**Figure S2-1.d**), the transformation of VCl_3 to VO_x during the laser-scribing process is verified by the XRD patterns. As shown by the XPS spectrum (**Figure 2-2.f**), the broad V 2p peaks indicate the presence of multiple vanadium valence states. The profile fits indicate that the V $2p_{3/2}$ V(III) peak at 514.9 eV accounts for 69.9 at. % of all the vanadium present. This suggests that the major oxidation state is +3, consistent with the predominant peaks of V_2O_3 in the XRD patterns. The V $2p_{3/2}$ V(IV) peak at 516.5 eV, representing 14.3% of the total vanadium content, can be attributed to VO_2. The non-stoichiometric vanadium oxides as well as the defects in V_2O_3 and VO_2 also give rise to the V $2p_{3/2}$ V(II) and V(V) peaks at 512.9 eV and 517.9 eV, respectively. The O 1s region shows not only a C-O peak, but also a metal oxide peak at 529.9 eV, confirming the formation of VO_x (**Figure S2-4.a**). The C 1s peak is dominated by the sp^2 contribution with residual oxygen-containing groups present, confirming the reduction of GO (**Figure S2-4.b**). In summary, all evidence from SEM, TEM, XPS, and XRD indicates the

simultaneous formation of VO_x and LSG during the laser-scribing process, as described by **Figure 2-1.a**.

Vanadium loading optimization and electrochemical characterization of LSG/VO_x electrodes

The electrochemical properties of the LSG/VO_x electrodes were evaluated in a three-electrode setup with an Ag/AgCl reference electrode and a graphite counter electrode in 10 M LiCl electrolyte. First, the starting VCl_3:GO precursor mass ratio was varied to find the optimal content of vanadium in the nanocomposite in terms of capacitive performance. The galvanostatic charge/discharge (GCD) curves at 1 mA cm^{-2} for the LSG/VO_x nanocomposites with different VCl_3:GO ratios are shown in **Figure 2-3.a**. At a low current density, all samples can be steadily charged from –1.4 V to 0.8 V (vs. Ag/AgCl) with observable redox plateaus, except for those with VCl_3:GO = 1 and no VCl_3 that have smaller potential windows of –1.3 V to 0.7 V (vs. Ag/AgCl) and –0.6 V to 0.7 V (vs. Ag/AgCl). This indicates that the large electrochemically active voltage window can be attributed to the high VO_x loading in the electrode. **Figure 2-3.b** summarizes the capacitance that is calculated based on cyclic voltammetry (CV) curves at a range of scan rates and normalized to the active material mass of the electrodes made from the different VCl_3:GO ratios. All electrodes with any addition of VCl_3 have increasing capacitance as the scan rate falls, suggesting that the capacitance is dominated by the pseudocapacitive contribution from the redox reactions of VO_x. At scan rates below 1 V s^{-1}, the nanocomposite electrode with VCl_3:GO = 4 has the highest gravimetric capacitance, and this ratio is therefore determined to be the optimal precursor ratio and used in later device fabrication. At 20 mV s^{-1}, the highest specific capacitance of 1110 F g^{-1} was achieved (with areal mass loading of 0.302 mg cm^{-2}), which is nearly 20 times higher than the LSG with no vanadium content. This remarkable improvement can be ascribed to

the LSG framework within which the pseudocapacitive VO_x nano-spacers are anchored. This results in improved migration of electrolyte ions into active sites, enabling the VO_x pseudocapacitance to be efficiently exploited. It is not surprising that the nanocomposite with VCl_3:GO = 4 is the best-performing electrode because there exists a favorable balance where the VO_x content is sufficiently high to provide substantial pseudocapacitance, while not so excessive that access to the LSG scaffold is compromised due to significant VO_x aggregations. As shown in **Figure 2-3.c**, the electrochemical behaviors of the LSG/VO_x nanocomposite electrodes with the optimized VCl_3:GO = 4 ratio were further investigated by CV. At scan rates from 200 mV s^{-1} to 5 mV s^{-1}, the CV curves adopt a distorted rectangular shape with two pairs of broad redox peaks, suggesting pseudocapacitive behavior, which will be further discussed later. Furthermore, control experiments were carried out to simulate the scenario where all vanadium content in the LSG/VO_x electrode dissolve in the electrolyte. As shown in **Figure S2-6**, neither the LSG nor the graphite paper substrate contribute significant capacitance in vanadium-containing electrolytes, confirming that the LSG/VO_x electrode is the only significant source of the high capacitance.

To demonstrate the advantages of the one-step laser process, the performance of the LSG/VO_x electrode is compared to an electrode made simply from an rGO/V_2O_3 mixture. As shown in **Figure 2-4.a**, the laser scribing of the LSG/VCl_3 mixture not only creates a network for charge transfer, but also provides nano-size vanadium oxides of various oxidation states and/or phases, compared to the rGO/V_2O_3 physical mixture made by conventional means. The cross-sectional SEM image of an rGO/V_2O_3 film on a PET substrate shows a completely stacked structure with no observable pores or layers (**Figure 2-4.b**). On the other hand, **Figure 2-4.c** illustrates the expanded and porous LSG scaffold supplying numerous pathways for charge transport. As shown

by the orange curve in **Figure 2-4.d**, at a very low scan rate of 1 mV s^{-1}, it is revealed that there are multiple redox couples involved in the charge/discharge of the LSG/VO_x electrode, which can be assigned to the near-surface Faradaic processes of multistep electrochemical exchanges among different vanadium valence states of VO_x[17,34] and Li ion insertion into various probable VO_x phases.[35–37] The possible reaction involved can be represented by the following equation:

$$VO_x + nLi^+ + ne^- \leftrightarrow Li_nVO_x \quad (1)$$

The asymmetric peaks in the positive potential region represent an irreversible redox reaction and can be attributed to the formerly reported chemical dissolution of vanadium(V) oxide forming yellow colored soluble species such as $H_2VO_4^-$ and/or HVO_4^{2-},[38] which was also observed in our experiments (**Figure S2-5.b**). Note that the major pseudocapacitive contributions are from the region between –1.3 V and 0.2 V (vs. Ag/AgCl), corroborating that V(III) is the primary vanadium oxidation state in the nanocomposite. Thus, in an ideal scenario, the aqueous LSG/VO_x symmetric supercapacitors are expected to achieve the best capacitance and long cycle life by operating in the voltage window between –1.3 V and 0.2 V (vs. Ag/AgCl). In contrast, the green CV curve of the rGO/V_2O_3 electrode at 1 mV s^{-1} shows no peak at all and a significantly smaller area, indicating a lack of diverse vanadium valence states or structural phases. This is consistent with the XRD pattern of the rGO/V_2O_3 electrode that solely matches $V_2O_5 \cdot 1.6\ H_2O$ (

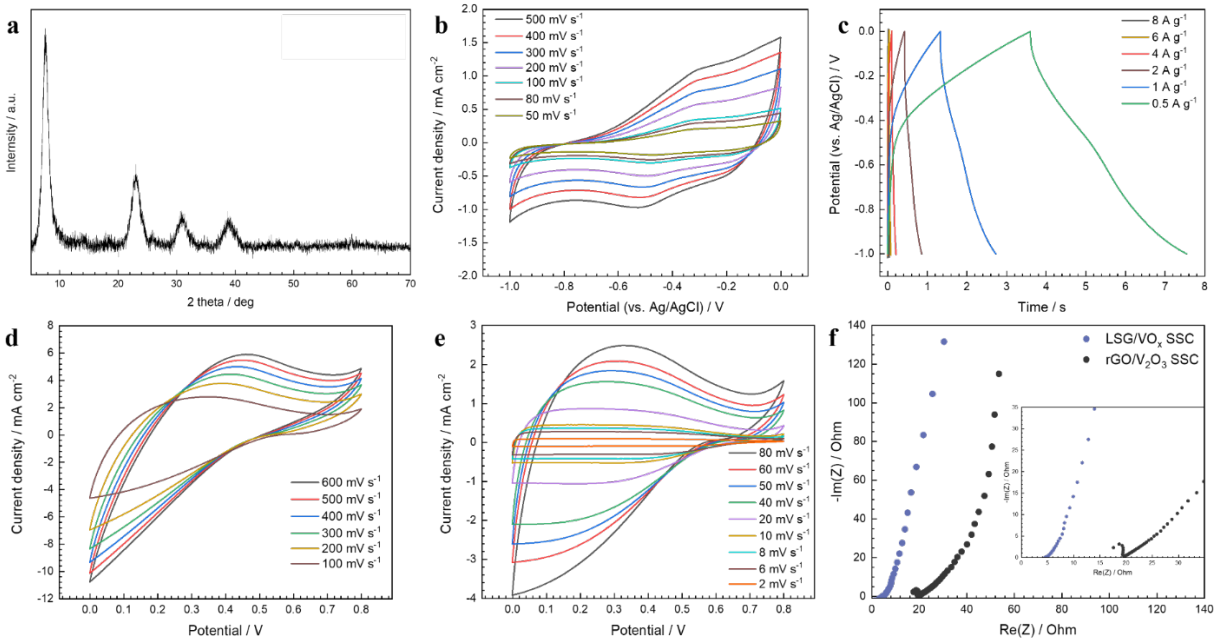

Figure S2-7.a), resulting from V_2O_3 oxidation in water.

Moreover, the electrochemical window of the rGO/V_2O_3 electrode is –1 V to 0 V vs. Ag/AgCl, which is dramatically smaller than that of the LSG/VO_x electrode, leading to a much smaller capacitance of 17 F g^{-1} at 1 mV s^{-1}, which is about 1/100 of that of the LSG/VO_x electrode. Furthermore, electrochemical impedance spectroscopy (EIS) was used to assess the charge transport properties of the LSG/VO_x and rGO/V_2O_3 electrodes (**Figure 2-4.e**). In **Figure 2-4.e**, the Nyquist plot (orange) of the LSG/VO_x possesses a semicircle in the high-frequency region and a steep straight line in the low-frequency region, signifying a resistive and a capacitive component in the equivalent circuit, respectively. On the other hand, the Nyquist plot (green) of the rGO/V_2O_3 electrode shows low phase angles that deviate from capacitive behavior even at high frequencies. As shown in the inset of **Figure 2-4.e**, the LSG/VO_x electrode has much smaller equivalent series resistance (ESR) and charge transfer resistance (R_{ct}) compared to the rGO/V_2O_3 electrode. The R_{ct} of the LSG/VO_x electrode is 0.28 Ω, based on the diameter of the semicircle, and the small R_{ct} can

be ascribed to the LSG scaffold that provides both high electronic and ionic conductivity. The Bode plot (**Figure S2-5.d**) shows a phase angle of -79° at low frequencies, close to -90° expected for an ideal capacitor. The tilt of the CV curves, as well as the sizable *iR* drop in the GCD curves, also suggest the higher resistivity of the rGO/V_2O_3 electrode (

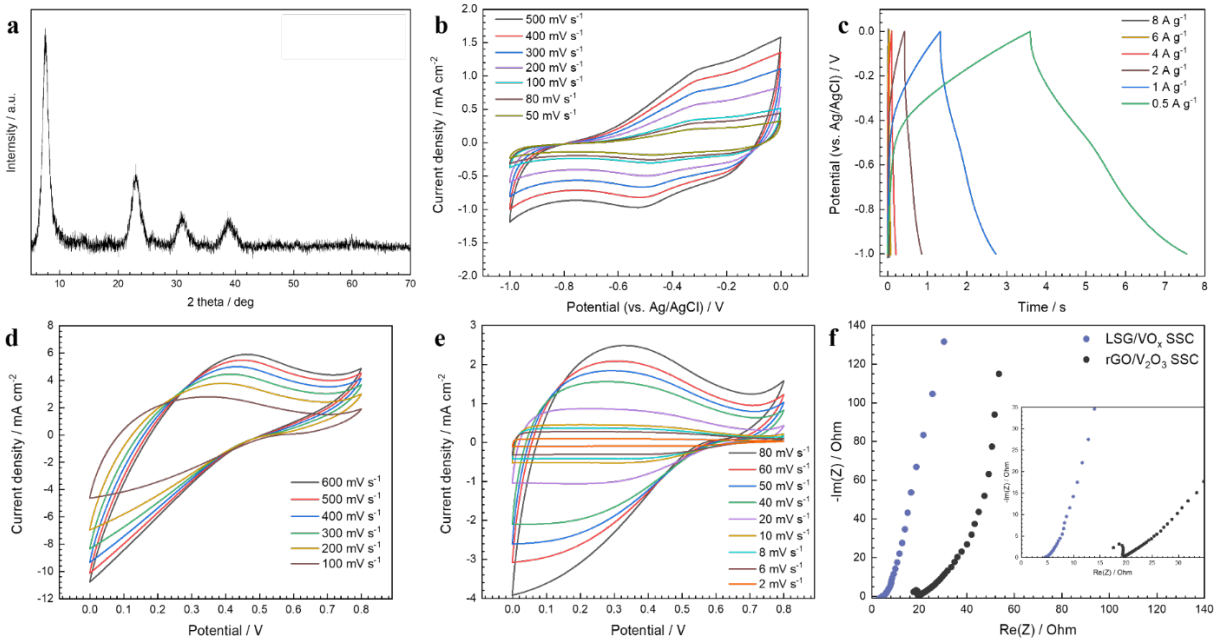

Figure S2-7.b-c). Overall, due to the well-structured LSG platform as well as the multi-valency and phase diversity of the VO_x nanoparticles, the LSG/VO_x electrodes synthesized by laser writing possess considerably improved electrochemical properties compared to the physically mixed rGO/V_2O_3.

Aqueous LSG/VO_x symmetric supercapacitors

To assess the electrochemical performance of the LSG/VO_x nanocomposite electrodes in a more practical setup, symmetric supercapacitors were fabricated from two LSG/VO_x electrodes

separated by a polymer separator in a 10 M LiCl electrolyte. The CV curves of the symmetric device show nearly rectangular shapes with a stable voltage window of 1.3 V and are consistent at different scan rates, indicating ideal energy storage behaviors (**Figure 2-5.a**). The GCD profiles also adopt triangular shapes with negligible *iR* drops and show that the devices can be steadily charged to 1.3 V even at a low current density of 0.5 A g^{-1}, confirming fast pseudocapacitive properties (**Figure 2-5.b**). **Figure 2-5.c-d** summarize the gravimetric device capacitance, energy density, and power density calculated from CV curves at scan rates ranging from 1000 mV s^{-1} to 1 mV s^{-1}. At 6 mV s^{-1}, the device gravimetric capacitance can reach 229 F g^{-1}, with an energy density and power density of 54 Wh kg^{-1} and 894 W kg^{-1}, respectively. At a high scan rate of 1000 mV s^{-1}, the symmetric supercapacitor can achieve a power density of 21 kW kg^{-1} (with an energy density of 2 Wh kg^{-1}). As demonstrated by **Figure 2-5.e**, LSG/VO_x symmetric devices can power a red light-emitting diode (LED) (2.1 V, 20 mA) when two of them are connected in series. The LED remained bright for greater than 10 minutes.

Unlike most supercapacitors based on vanadium oxides that can only retain their peak performance for the first few thousand cycles before suffering severe capacitance loss,[21,22,39] the LSG/VO_x symmetric supercapacitor (SSC) can retain 119% and 112% of its initial capacitance after continuously being charged and discharged at 40 A g^{-1} (12 mA cm^{-2}) for 10,000 and 20,000 cycles, respectively, as illustrated in **Figure 2-5.f**. An increase in capacitance of ~23% was observed in the first ~700 cycles, which was further investigated by measuring the respective voltages of the positive and negative electrode with an Ag/AgCl reference electrode. As shown in the inset to **Figure 2-5.f**, the potentials of both electrodes gradually shift in the negative direction. As a result, the 1.3 V voltage window moves from –0.5 – 0.8 V (vs. Ag/AgCl) to –0.7 – 0.6 V (vs. Ag/AgCl),

stepping into the more electrochemically active region where one or two sets of redox peaks are seen in **Figure 2-3.c** and **Figure 2-4.d**, accounting for the unusual sharp capacitance increase in the first few hundred cycles. Even if the cycling stability is calculated based on the peak capacitance, the capacitance retention can still reach 92% after 19,000 cycles.

Therefore, the aqueous LSG/VO_x SSCs can achieve a high energy density of 54 Wh kg^{-1} and a power density of 21 kW kg^{-1} with a reliable operating voltage of 1.3 V, outperforming most aqueous vanadium-based SSCs that typically have potential windows of 0.8 to 1 V.[21,40–43]

Quasi-solid-state LSG/VO_x symmetric supercapacitors

As it is desirable to increase the operating voltage of the LSG/VO_x SSCs for more practical applications, quasi-solid-state LSG/VO_x SSCs with a LiCl/PVA electrolyte were assembled and studied. Although vanadium possesses four (II-V) easily accessible oxidation states and its oxides are expected to have large stable electrochemically active voltage windows, the actual operating potential range is considerably constrained by the chemical dissolution and structural instability of the electrode material that both lead to a dramatic loss of capacitance during constant charge/discharge cycling in aqueous electrolytes.[37,44–46] The utilization of polymer gel electrolyte has been demonstrated to be a relatively simple strategy to surmount this problem,[38] in comparison to using flammable and toxic organic electrolytes[47] or introducing a protective layer.[48] The CV curves in **Figure 2-6.a** show a slightly distorted rectangular shape, confirming excellent supercapacitor behavior. Additionally, triangular GCD profiles also suggest that the capacitive mechanism of the gel LSG/VO_x SSC can be attributed to fast surface Faradaic reactions (**Figure 2-6.b-c**). Notably, the triangular shape holds even at an extremely low current density of 0.5 A g^{-1}, and the *iR* drop remains small even at a high current density of 40 A g^{-1}. As demonstrated in

Figure 2-6.d, the gravimetric and areal capacitances increase as the current density falls, indicating a dominant pseudocapacitive contribution in the charge storage process. Based on CV calculations, the gravimetric device capacitance, energy density, and power density can reach 208 F g^{-1}, 65 Wh kg^{-1}, and 156 W kg^{-1}, respectively, at 1 mV s^{-1} (**Figure 2-6.e**). As illustrated in **Figure 2-6.f**, the Coulombic efficiency of the quasi-solid-state LSG/VO_x SSCs is close to 100% at all scan rates ranging from 1000 mV s^{-1} to 5 mV s^{-1} and can still retain 85% at 1 mV s^{-1}, indicating outstanding cycling stability.

Figure 2-6.g compares the Nyquist plots of the aqueous and the gel LSG/VO_x SSCs. As demonstrated in the inset, the ESR of both devices are similar and below 5 Ω, and the semicircle signifying R_{ct} can hardly be observed in either device, suggesting very small R_{ct} and very fast surface Faradaic reactions as also verified by the small *iR* drops in the GCD measurements (**Figure S2-8.** and **Figure 2-6.b-c**). Although both Nyquist plots show high slopes at low frequencies representing almost ideal capacitive performance, a Warburg region inclined at 45° is observed for the solid-state LSG/VO_x SSC at higher frequencies, indicating that the charge transfer at the electrode-electrolyte interface is largely controlled by diffusion,[49] which is expected for the Li ion diffusion from the gel electrolyte to the electrode material.[50] **Figure 2-6.h** evaluates the capacitance retention during continuous charging and discharging between 0 V and 1.5 V. The quasi-solid-state LSG/VO_x SSC shows exceptional capacitance retention of ~100% and 90% after being continuously charged and discharged at 30 A g^{-1} (9 mA cm^{-2}) for 10,000 and 20,000 cycles, respectively, while the aqueous LSG/VO_x SSC can only retain 57% of its initial capacitance after cycling 10,000 times. In summary, the quasi-solid-state LSG/VO_x SSC with a cell voltage of 1.5 V can reach a high device capacitance, energy density, and power density and show extraordinarily

low capacitance loss that can be attributed to the limited chemical dissolution of the electrochemically active VO_x species. By connecting two of the quasi-solid-state LSG/VO_x SSCs in series, not only red LEDs, but also green (2.8 V, 20 mA) and blue (2.9 V, 20 mA) LEDs can be powered for over 10 minutes (**Figure 2-6.i**). The gel LSG/VO_x SSCs are also flexible, as evidenced by the unchanged CV profile when the device is bent (**Figure S2-9.**).

To explore the limit of the operating potential of devices based on the LSG/VO_x electrodes, LiCl/PVA gel LSG/VO_x SSCs with 1.7 V cell voltage, and aqueous rGO//LSG/VO_x asymmetric supercapacitors (ASCs) were assembled and tested. The 1.7 V quasi-solid-state LSG/VO_x SSC can reach a high energy density of 60 Wh kg^{-1} and a power density of 127 W kg^{-1} with satisfactory cycling stability of 75% capacitance retention after 10,000 cycles, although not outperforming the previously discussed 1.5 V device (**Figure S2-10.**). As hinted by the observable pair of redox peaks in the CV curves and the increased distortion of the GCD profiles, the deteriorating energy storage performance can be explained by the involvement of the highly unstable VO_x species that are seen in **Figure 2-4.d**. Similarly, while the cell voltage can be increased to 1.8 V by substituting rGO as the positive electrode, the behavior of the rGO//LSG/VO_x ASC deviates from ideal supercapacitors, as not only indicated by the substantial distortion of the CV curves, but also by signs of polarization observed at relatively high scan rates (Figure S2-10.). Additionally, since the rGO used was reduced chemically instead of undergoing laser-scribing, the gravimetric electrochemical parameters of the rGO//LSG/VO_x ASC are not as high as those of the LSG/VO_x SSC, the thin-film electrodes of which have much higher specific capacitance (**Figure 2-3.b**). In Error! Reference source not found.**a**, the operating voltage is plotted against the gravimetric device capacitance for SSCs (triangles)[51–54] and ASCs (circles)[34,55] of vanadium oxides or metal oxides. The performance

of the aqueous LSG/VO_x SSC (1.3 V, 229 F g^{-1}), the quasi-solid-state LSG/VO_x SSC (1.5 V, 231 F g^{-1}; 1.7 V, 150 F g^{-1}) and the aqueous rGO//LSG/VO_x ASC (1.8 V, 72 F g^{-1}) are all superior to the previously reported systems.

The energy storage performance of the aqueous and quasi-solid-state LSG/VO_x SSCs in this work are compared to previously reported vanadium oxides-based supercapacitors and to commercially available energy storage devices. Error! Reference source not found.**b** presents a Ragone plot of gravimetric energy and power density, in which the LSG/VO_x SSC data were calculated based on the total active material mass. The aqueous and gel LSG/VO_x SSCs can reach energy densities of 50 Wh kg^{-1} and 72 Wh kg^{-1} with power densities of 324 W kg^{-1} and 370 W kg^{-1} at 0.5 A g^{-1}, respectively, with the latter significantly outperforming other SSCs[17,51,52] (triangles) and ASCs (circles)[34,55,56] in the literature at similar power densities. Additionally, both LSG/VO_x SSCs can achieve high power densities of greater than 1000 W kg^{-1} with the corresponding energy densities still above 30 Wh kg^{-1}, demonstrating superior rate capability. The volumetric energy and power densities of the aqueous and quasi-solid-state LSG/VO_x SSCs were calculated based on the total volume of the electrodes, current collectors, separator, and electrolyte, and are compared with vanadium oxide systems in the literature[42,55,57,58] and commercially available energy storage devices[59,60] in Error! Reference source not found.**c**. The aqueous and gel LSG/VO_x SSCs can reach energy densities of 5.3 mWh cm^{-3} and 7.7 mWh cm^{-3} with power densities of 35 mW cm^{-3} and 39 mW cm^{-3} at 0.5 A g^{-1}, respectively. Both LSG/VO_x SSCs can achieve better electrochemical performance than previously reported systems and current commercial devices. In particular, both devices can attain similar energy densities to a 500 mAh/4 V lithium thin-film battery, with power densities almost 20 times higher. Additionally, the LSG/VO_x SSCs can achieve high power densities (> 1000 mW cm^{-3}) that are comparable to that of a 3 V/200 mF Al electrolytic capacitor,

while obtaining energy densities that are nearly four orders of magnitude higher. Thus, as indicated by the above results, the LSG/VO_x SSCs are promising candidates for future energy storage applications.

Conclusions

In summary, we report graphene/vanadium oxide-based thin-film symmetric supercapacitors with high energy density and excellent cycling stability. The LSG/VO_x nanocomposite electrodes can be produced in a facile laser-scribing process in which reduction of GO and formation of VO_x occur simultaneously leading to a high three-electrode specific capacitance of 1110 F g^{-1}. The presence of multiple easily accessible valence states in the VO_x particles formed provides a large electrochemically active potential window, and the LSG scaffold can supply fast charge transfer pathways. As a result, the aqueous LSG/VO_x SSC can reach a high energy density of 54 Wh kg^{-1} at a power density of 894 W kg^{-1} with essentially no capacitance loss after 20,000 cycles. Moreover, the voltage window can be extended to 1.5 V by employing a LiCl/PVA gel electrolyte with 90% capacitance retention. The flexible all solid-state LSG/VO_x SSC can reach a high energy density of 72 Wh kg^{-1} at a power density of 370 W kg^{-1} with extremely small charge transfer resistance and Coulombic efficiency close to 100% even at slow scan rates. Furthermore, not only does the gravimetric electrochemical performance of the LSG/VO_x SSCs outperform those of similar systems reported in the literature, but also the volumetric energy and power densities can achieve the standards of commercial energy storage devices. Overall, this work offers a promising strategy for the simple fabrication of high-performance supercapacitors that can be utilized in flexible, solid-state, wearable electronics.

Experimental Section

Material characterization: The scanning electron microscopy (SEM) images of the LSG/VO_x nanocomposite were collected using a JEOL JSM-67 Field Emission Scanning Electron Microscope. Transmission electron microscopy (TEM) was performed on a Tecnai G TF20 TEM (FEI Inc.), and the particle distribution was obtained from the analysis of TEM images using the ImageJ software. X-ray powder diffraction (XRD) was performed by a Panalytical X'Pert Pro X-ray powder diffractometer using Cu Kα radiation with a wavelength of 0.154 nm on a silicon zero-background plate. The X-ray photoelectron spectroscopy (XPS) spectra were acquired using a Kratos Axis Ultra DLD spectrometer equipped with a monochromatic Al Kα X-ray source. The mass of the active material on the electrode was measured using a Mettler Toledo MX5 microbalance with 0.001 mg sensitivity. Two or three electrodes were sampled from every batch and the mean areal loading was found to be 0.302 mg cm^{-2} with a standard deviation of 3.63%. The thickness of the electrodes (15 μm) was determined by cross-sectional SEM and those of the separator (7 μm) and current collectors (10 μm) were measured by a Mitutoyo digital micrometer.

Synthesis of LSG/VO_x: The graphite oxide (GO) was synthesized via a modified Hummer's method.[61] In a typical synthesis, 1.5 mL of 10 mg ml^{-1} GO stock was diluted with the addition of 0.6 mL DI water, and the required amount of VCl_3 was dissolved in 1.5 mL of DI water. The two separate solutions were sonicated for 2 hours. Next, the VCl_3 solution was slowly added to the GO suspension while stirring at a controlled rate via a syringe pump. 100 μL of the resulting mixture was then drop-cast onto graphite paper (Panasonic) making the electrode area 1 cm^2 and left to dry under ambient conditions. Finally, the dried film was laser-scribed using a 40 W Full Spectrum

Laser Muse 2D Vision Desktop CO_2 Laser Cutter with a 12% power setting. The as-made LSG/VO_x electrodes were used for electrochemical testing and characterization.

Fabrication of aqueous LSG/VO_x symmetric supercapacitors: The aqueous LSG/VO_x symmetric supercapacitors were fabricated from a pair of electrodes with active areas of 1 cm^{-2} sandwiched by a cellulose separator (Celgard) that was wetted in 10 M LiCl electrolyte. The current collectors were extended using 3M copper tape and the device was assembled using Kapton tape.

Fabrication of quasi-solid-state LSG/VO_x symmetric supercapacitors: To make the LiCl/PVA electrolyte, 1 g of PVA powder was added to 10 mL of DI water. The mixture was heated to 90 °C under stirring. After the powder was completely dissolved, 4.24 g of LiCl was added to the mixture and constantly stirred until a clear viscous solution formed. It was then cooled to room temperature. A drop of the LiCl/PVA electrolyte was added to each of the electrodes and the separator and left for 30 minutes. After the excess electrolyte was removed, the separator was sandwiched between the two electrodes, and the assembled device was dried at 40 °C overnight. Subsequently, the current collectors were extended using 3M copper tape and the device was assembled using Kapton tape. The quasi-solid-state LSG/VO_x SSC was then sealed using parafilm to prevent absorption of moisture.

Electrochemical testing: The electrochemical properties of the LSG/VO_x electrodes were assessed by cyclic voltammetry (CV), galvanostatic charge-discharge (GCD), and electrochemical impedance spectroscopy (EIS) measurements using a Biologic VMP3 electrochemical workstation

equipped with a 10-A current booster (VMP3b–10, USA Science Instrument). For potentiostatic EIS measurements (sinus amplitude 10 mV), 10 data points per decade were collected from 1 MHz to 1 mHz with, at the open circuit voltage. In three-electrode experiments, graphite paper and an Ag/AgCl electrode (BASi) were used as the counter and reference electrodes, respectively; and the electrodes were immersed in 10 M LiCl electrolyte. The potentials of individual electrodes during cycle life measurement were obtained by a three-channel measurement of a three-electrode system, with one channel carrying out charge/discharge of the LSG/VO_x electrodes and the other monitoring the potential of the anode and cathode against the Ag/AgCl reference electrode.

Acknowledgments

The authors thank National Science Foundation Grant DGE–1735325 (M.A.), Nanotech Energy (R.B.K.) and the Dr. Myung Ki Hong Endowed Chair in Materials Innovation (R.B.K.) for financial support.

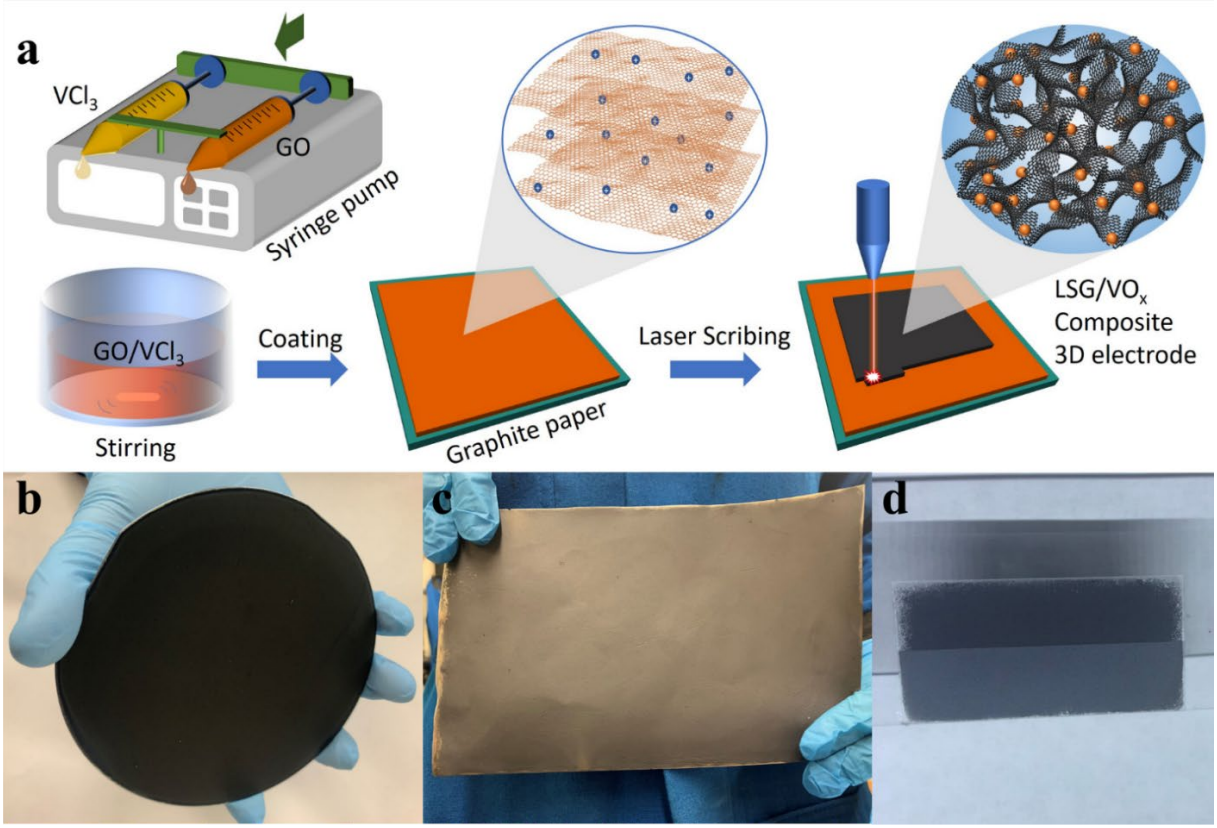

Figure 2-1. Fabrication of LSG/VO_x composite electrodes. (a) Schematic illustration of the electrode fabrication process. (b and c) Optical images of the LSG/VO_x film coated on a silicon wafer and a large sheet of graphite paper. (d) Optical image of an LSG/VO_x film on a transparent plastic substrate showing the composite before (bottom) and after (top) laser irradiation.

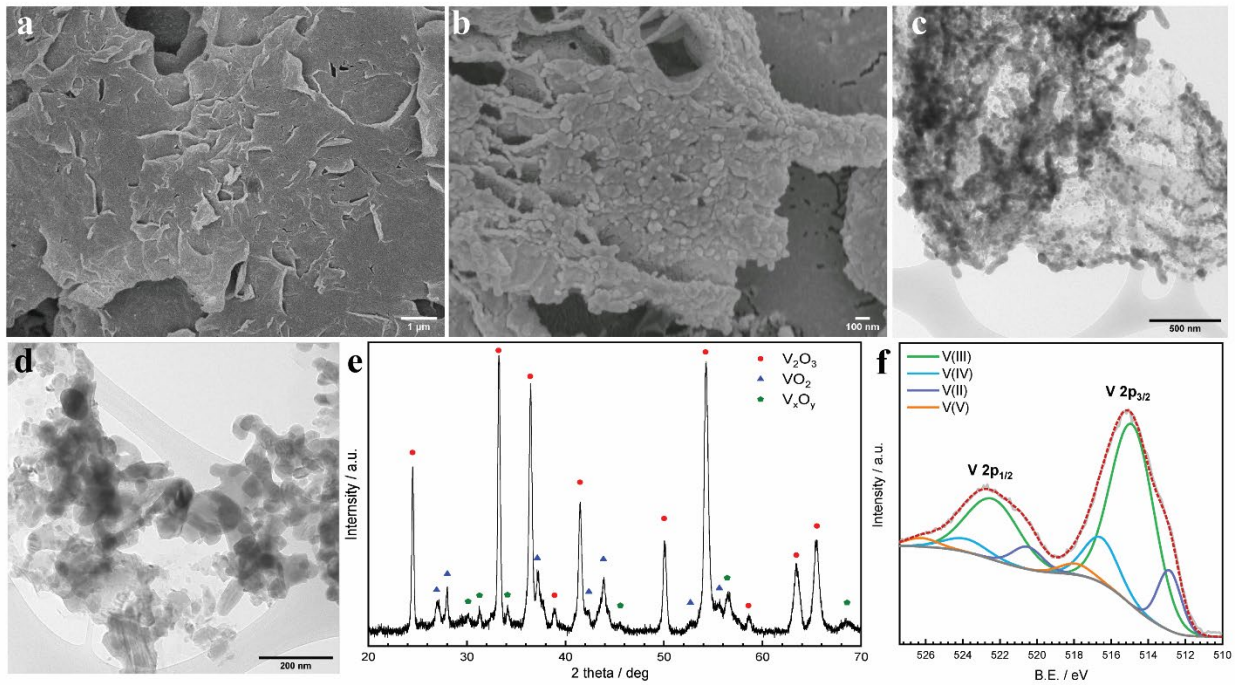

Figure 2-2. Microscopic and spectroscopic characterization of the LSG/VO_x composite (VCl_3:GO = 4:1). (a and b) Low- and high-magnification SEM images of the LSG/VO_x composite. (c) A TEM image showing the VO_x particles on graphene. (d) A high-magnification TEM image of the VO_x network. (e) XRD pattern of the composite matching V_2O_3 (JCPDS no. 34–0187), VO_2 (JCPDS no. 09–0142), and mixed-valence vanadium oxides. (f) XPS V 2p spectrum of the LSG/VO_x composite.

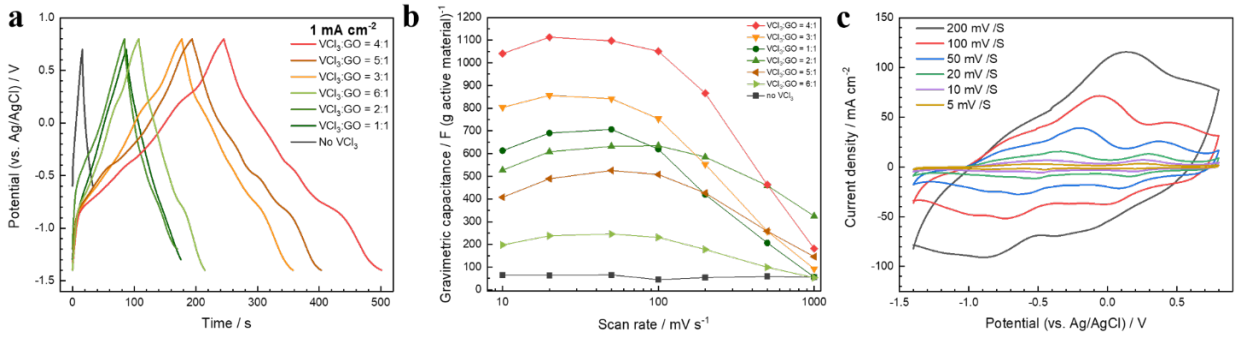

Figure 2-3. Electrochemical measurements of the LSG/VO_x composite in a three-electrode setup. (a) Galvanostatic charge/discharge (GCD) curves of LSG/VO_x with different VCl_3:GO ratios at 1 mA cm^{-2}. (b) The gravimetric capacitance of LSG/VO_x with different precursor VCl_3:GO ratios at a range of scan rates. (c) Cyclic voltammetry (CV) curves of LSG/VO_x at 5, 10, 20, 50, 100, 200 mV s^{-1}.

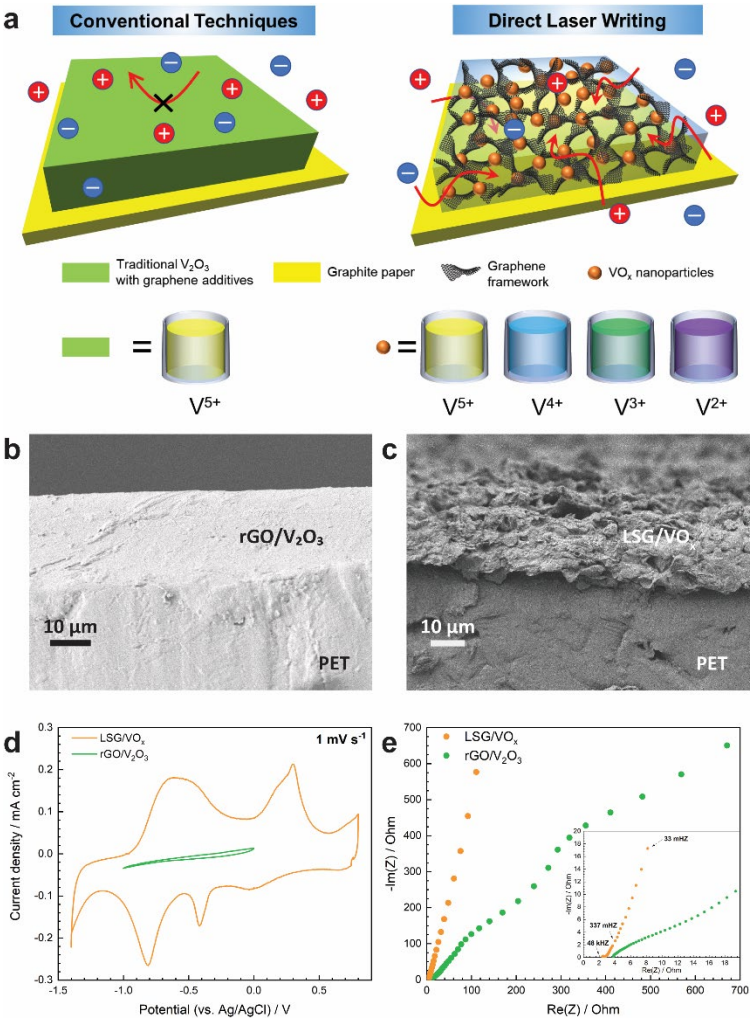

Figure 2-4. Comparison between the laser irradiated LSG/VO_x and traditional rGO/V_2O_3 electrodes. (a) A schematic contrasting conventional techniques and laser scribing for the preparation of redox-active composite electrodes based on vanadium oxides and graphene. (b and c) Cross-sectional SEM images of the rGO/V_2O_3 and LSG/VO_x electrodes. (d) CV curves of LSG/VO_x and rGO/V_2O_3 at 1 mV s^{-1} showing several redox peaks. (e) A Nyquist impedance plot of the LSG/VO_x and rGO/V_2O_3 electrodes with the high-frequency region in the inset.

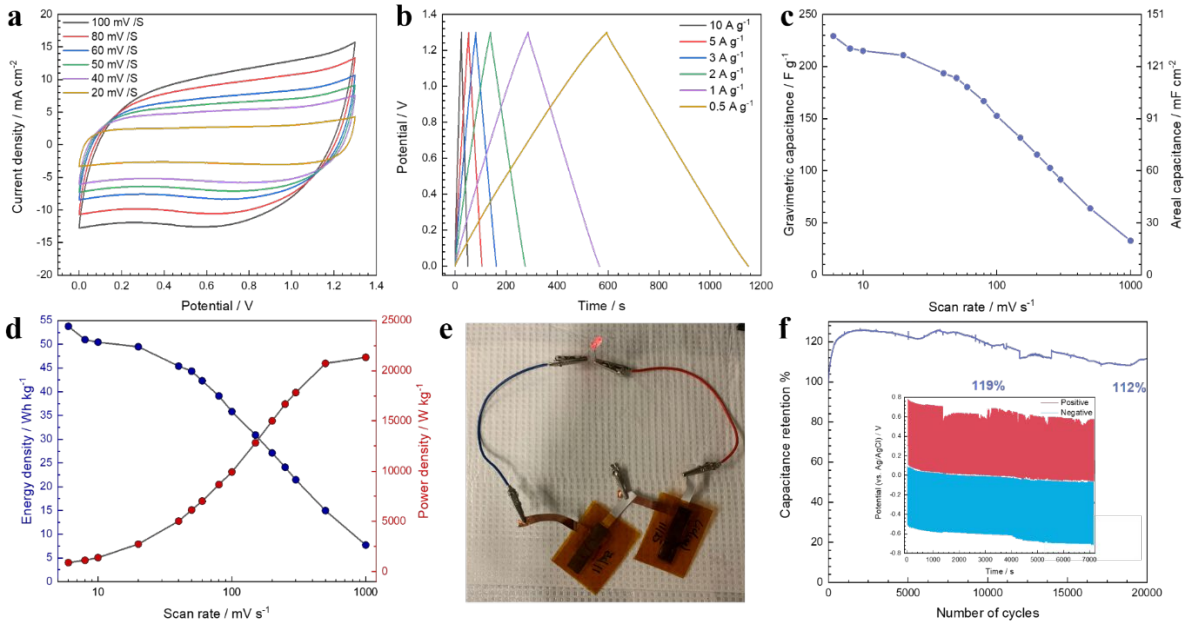

Figure 2-5. Electrochemical measurements of an aqueous 10 M LiCl LSG/VOx symmetric supercapacitor (SSC). (a) CV curves of an aqueous LSG/VOx SSC at 20, 40, 50, 60, 100 mV s–1. (b) GCD curves of an aqueous LSG/VOx SSC at 0.5, 1, 2, 3, 5, 10 A g–1. (c) Gravimetric and areal capacitance of an aqueous LSG/VOx SSC at various scan rates. (d) Gravimetric energy and power densities of an aqueous LSG/VOx SSC at various scan rates. (e) A photo showing that two aqueous LSG/VOx SSCs connected in series can power a red light-emitting diode (LED) for an extended period of time. (f) Long-term stability of an aqueous LSG/VOx SSC after 20,000 cycles.

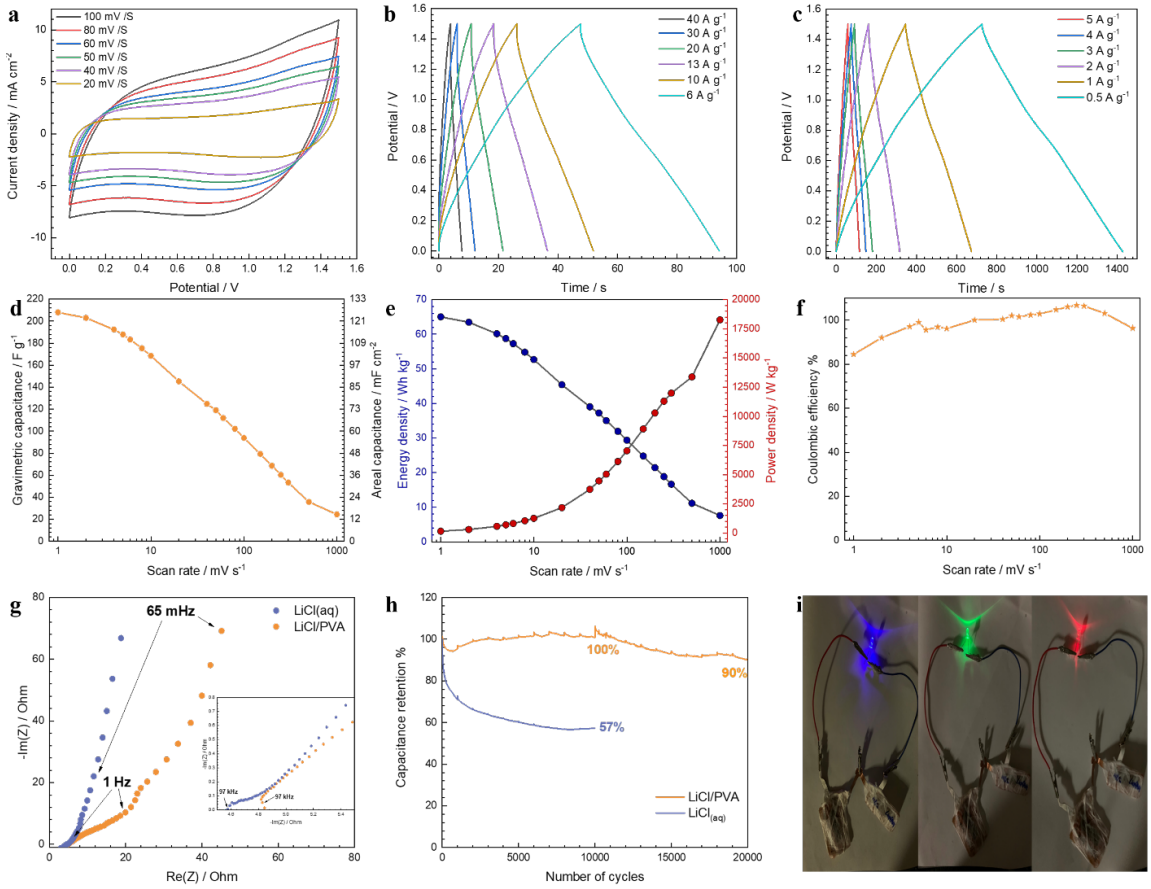

Figure 2-6. Electrochemical measurements of an LiCl/PVA quasi-solid-state LSG/VO_x symmetric supercapacitor. (a) CV curves of a gel LSG/VO_x SSC at 20, 40, 50, 60, 100 mV s^{-1}. (b-c) GCD curves of an aqueous LSG/VO_x SSC at 40, 30, 20, 13, 10, 6, 5, 4, 3, 2, 1 and 0.5 A g^{-1}. (d) Gravimetric and areal capacitance of a gel LSG/VO_x SSC at various scan rates. (e) Gravimetric energy and power densities of a gel LSG/VO_x SSC at various scan rates. (f) Coulombic efficiency of a gel LSG/VO_x SSC at various scan rates. (g) A Nyquist impedance plot comparing an aqueous and a gel LSG/VO_x SSC with the high-frequency region in the inset. (h) Long-term stability of a 1.5 V gel LSG/VO_x SSC after 10,000 cycles compared to an aqueous LSG/VO_x SSC. (i) Photos showing two gel LSG/VO_x SSCs connected in series can power blue, green, and red LEDs for extended periods of time.

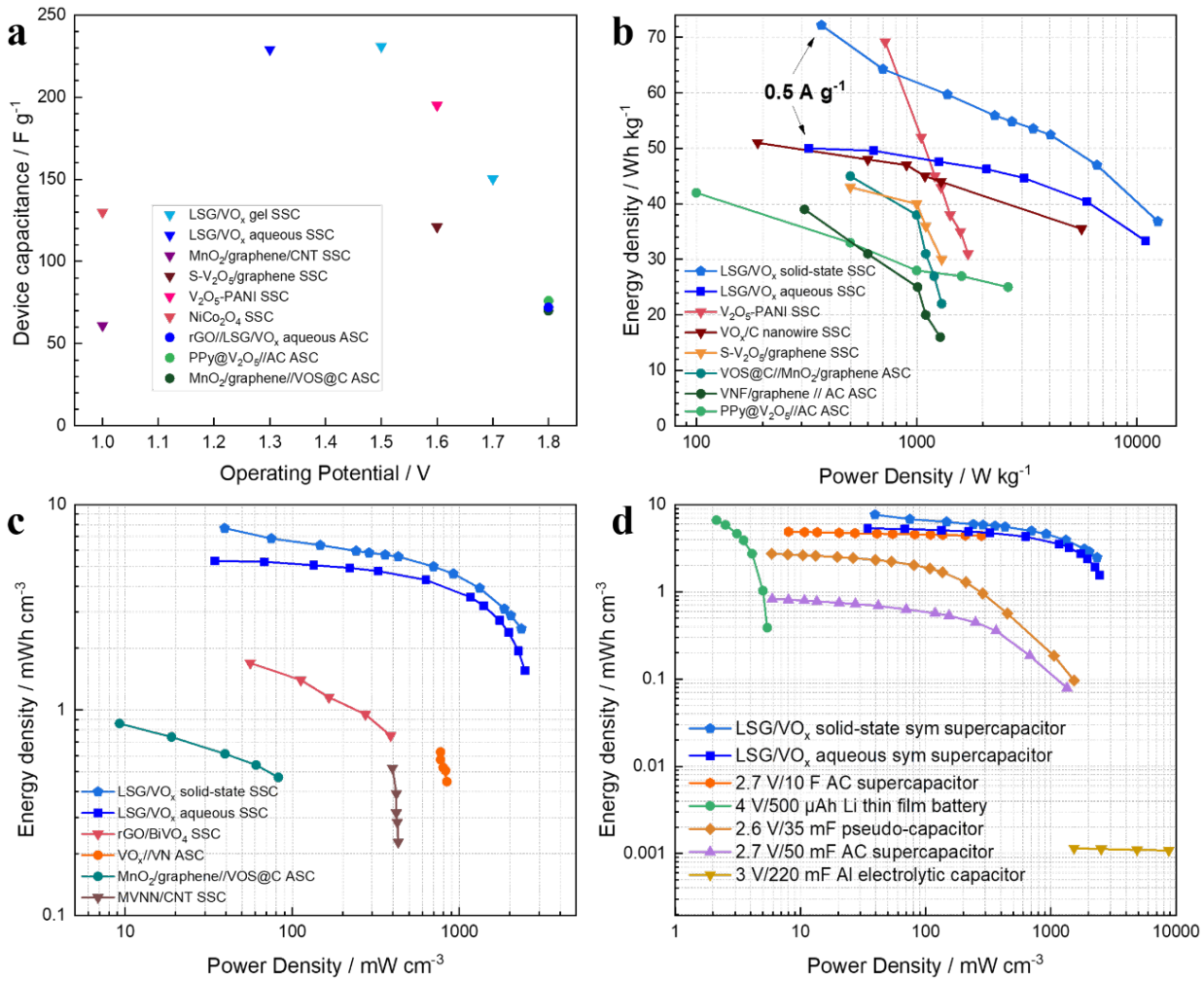

Figure 2-7. Comparing the performance of LSG/VOx supercapacitors with literature reports and commercially available energy storage devices. (a) Plot of operating potential and gravimetric capacitance comparing the LSG/VO_x devices to similar systems in the literature. (b) A Ragone plot comparing the gravimetric energy and power densities of LSG/VO_x symmetric supercapacitors (SSCs) to those of other vanadium oxide systems reported in the literature.[17,34,51,52,55,56,62] (c) A Ragone plot comparing the volumetric energy and power densities of LSG/VO_x symmetric supercapacitors to other vanadium oxide systems reported in the literature.[42,55,57,58] (d) A Ragone plot comparing the volumetric energy and power densities of LSG/VO_x symmetric supercapacitors to commercial energy storage devices.[59,60]

References

(1) Augustyn, V.; Simon, P.; Dunn, B. Pseudocapacitive Oxide Materials for High-Rate Electrochemical Energy Storage. *Energy Environ. Sci.* **2014**, *7* (5), 1597. https://doi.org/10.1039/c3ee44164d.

(2) Simon, P.; Gogotsi, Y. Materials for Electrochemical Capacitors. *Nat. Mater.* **2008**, *7* (11), 845–854. https://doi.org/10.1038/nmat2297.

(3) Wang, Y.; Shi, Z.; Huang, Y.; Ma, Y.; Wang, C.; Chen, M.; Chen, Y. Supercapacitor Devices Based on Graphene Materials. *J. Phys. Chem. C* **2009**, *113* (30), 13103–13107. https://doi.org/10.1021/jp902214f.

(4) Zhu, Y.; Murali, S.; Stoller, M. D.; Ganesh, K. J.; Cai, W.; Ferreira, P. J.; Pirkle, A.; Wallace, R. M.; Cychosz, K. A.; Thommes, M.; et al. Carbon-Based Supercapacitors Produced by Activation of Graphene. *Science.* **2011**, *332* (6037), 1537–1541. https://doi.org/10.1126/science.1200770.

(5) Shao, Y.; El-Kady, M. F.; Sun, J.; Li, Y.; Zhang, Q.; Zhu, M.; Wang, H.; Dunn, B.; Kaner, R. B. Design and Mechanisms of Asymmetric Supercapacitors. *Chem. Rev.* **2018**, *118* (18), 9233–9280. https://doi.org/10.1021/acs.chemrev.8b00252.

(6) Trasatti, S.; Buzzanca, G. Ruthenium Dioxide: A New Interesting Electrode Material. Solid State Structure and Electrochemical Behaviour. *J. Electroanal. Chem. Interfacial Electrochem.* **1971**, *29* (2), A1–A5. https://doi.org/10.1016/S0022–0728(71)80111–0.

(7) Lee, H. Y.; Goodenough, J. B. Supercapacitor Behavior with KCl Electrolyte. *J. Solid State Chem.* **1999**, *144* (1), 220–223. https://doi.org/10.1006/jssc.1998.8128.

(8) Xia, X.-H.; Tu, J.-P.; Wang, X.-L.; Gu, C.-D.; Zhao, X.-B. Mesoporous Co3O4 Monolayer Hollow-Sphere Array as Electrochemical Pseudocapacitor Material. *Chem. Commun.* **2011**, *47* (20), 5786. https://doi.org/10.1039/c1cc11281c.

(9) Wang, S.-Y.; Ho, K.-C.; Kuo, S.-L.; Wu, N.-L. Investigation on Capacitance Mechanisms of Fe[Sub 3]O[Sub 4] Electrochemical Capacitors. *J. Electrochem. Soc.* **2006**, *153* (1), A75. https://doi.org/10.1149/1.2131820.

(10) Lee, H. Y.; Goodenough, J. B. Ideal Supercapacitor Behavior of Amorphous V2O5·nH2O in Potassium Chloride (KCl) Aqueous Solution. *J. Solid State Chem.* **1999**, *148* (1), 81–84. https://doi.org/10.1006/jssc.1999.8367.

(11) Raju, V.; Rains, J.; Gates, C.; Luo, W.; Wang, X.; F. Stickle, W.; D. Stucky, G.; Ji, X. Superior Cathode of Sodium-Ion Batteries: Orthorhombic V2O5 Nanoparticles Generated in Nanoporous Carbon by Ambient Hydrolysis Deposition. *Nano Lett.* **2014**, *14* (7), 4119–4124. https://doi.org/10.1021/nl501692p.

(12) Tian, B.; Tang, W.; Su, C.; Li, Y. Reticular V 2 O 5 ·0.6H 2 O Xerogel as Cathode for Rechargeable Potassium Ion Batteries. *ACS Appl. Mater. Interfaces* **2018**, *10* (1), 642–650. https://doi.org/10.1021/acsami.7b15407.

(13) Chernova, N. A.; Roppolo, M.; Dillon, A. C.; Whittingham, M. S. Layered Vanadium and Molybdenum Oxides: Batteries and Electrochromics. *J. Mater. Chem.* **2009**, *19* (17), 2526. https://doi.org/10.1039/b819629j.

(14) Zhu, J.; Cao, L.; Wu, Y.; Gong, Y.; Liu, Z.; E. Hoster, H.; Zhang, Y.; Zhang, S.; Yang, S.; Yan, Q.; et al. Building 3D Structures of Vanadium Pentoxide Nanosheets and Application as Electrodes in Supercapacitors. *Nano Lett.* **2013**, *13* (11), 5408–5413.

https://doi.org/10.1021/nl402969r.

(15) Liang, S.; Hu, Y.; Nie, Z.; Huang, H.; Chen, T.; Pan, A.; Cao, G. Template-Free Synthesis of Ultra-Large V2O5 Nanosheets with Exceptional Small Thickness for High-Performance Lithium-Ion Batteries. *Nano Energy* **2015**, *13*, 58–66. https://doi.org/10.1016/j.nanoen.2015.01.049.

(16) Pan, X.; Ren, G.; Hoque, M. N. F.; Bayne, S.; Zhu, K.; Fan, Z. Fast Supercapacitors Based on Graphene-Bridged V 2 O 3 /VO x Core-Shell Nanostructure Electrodes with a Power Density of 1 MW Kg −1. *Adv. Mater. Interfaces* **2014**, *1* (9), 1400398. https://doi.org/10.1002/admi.201400398.

(17) Huang, Z.-H.; Song, Y.; Liu, X.-X. Boosting Operating Voltage of Vanadium Oxide-Based Symmetric Aqueous Supercapacitor to 2 V. *Chem. Eng. J.* **2019**, *358* (August 2018), 1529–1538. https://doi.org/10.1016/j.cej.2018.10.136.

(18) Khazaeli, A.; Godbille-Cardona, G.; Barz, D. P. J. A Novel Flexible Hybrid Battery–Supercapacitor Based on a Self-Assembled Vanadium-Graphene Hydrogel. *Adv. Funct. Mater.* **2020**, *30* (21), 1910738. https://doi.org/10.1002/adfm.201910738.

(19) Yu, M.; Zeng, Y.; Han, Y.; Cheng, X.; Zhao, W.; Liang, C.; Tong, Y.; Tang, H.; Lu, X. Valence-Optimized Vanadium Oxide Supercapacitor Electrodes Exhibit Ultrahigh Capacitance and Super-Long Cyclic Durability of 100 000 Cycles. *Adv. Funct. Mater.* **2015**, *25* (23), 3534–3540. https://doi.org/10.1002/adfm.201501342.

(20) Zhang, P.; Zhu, F.; Wang, F.; Wang, J.; Dong, R.; Zhuang, X.; Schmidt, O. G.; Feng, X. Stimulus-Responsive Micro-Supercapacitors with Ultrahigh Energy Density and Reversible Electrochromic Window. *Adv. Mater.* **2017**, *29* (7), 1604491.

https://doi.org/10.1002/adma.201604491.

(21) Majumdar, D.; Mandal, M.; Bhattacharya, S. K. V 2 O 5 and Its Carbon-Based Nanocomposites for Supercapacitor Applications. *ChemElectroChem* **2019**, *6* (6), 1623–1648. https://doi.org/10.1002/celc.201801761.

(22) Li, M.; Sun, G.; Yin, P.; Ruan, C.; Ai, K. Controlling the Formation of Rodlike V 2 O 5 Nanocrystals on Reduced Graphene Oxide for High-Performance Supercapacitors. *ACS Appl. Mater. Interfaces* **2013**, *5* (21), 11462–11470. https://doi.org/10.1021/am403739g.

(23) Wang, X.; Huang, Y.; Jia, D.; Kong Pang, W.; Guo, Z.; Du, Y.; Tang, X.; Cao, Y. Self-Assembled Sandwich-like Vanadium Oxide/Graphene Mesoporous Composite as High-Capacity Anode Material for Lithium Ion Batteries. *Inorg. Chem.* **2015**, *54* (24), 11799–11806. https://doi.org/10.1021/acs.inorgchem.5b01914.

(24) Zhao, H.; Pan, L.; Xing, S.; Luo, J.; Xu, J. Vanadium Oxides-Reduced Graphene Oxide Composite for Lithium-Ion Batteries and Supercapacitors with Improved Electrochemical Performance. *J. Power Sources* **2013**, *222*, 21–31. https://doi.org/10.1016/j.jpowsour.2012.08.036.

(25) Lv, W.; Yang, C.; Meng, G.; Zhao, R.; Han, A.; Wang, R.; Liu, J. VO2(B) Nanobelts/Reduced Graphene Oxide Composites for High-Performance Flexible All-Solid-State Supercapacitors. *Sci. Rep.* **2019**, *9* (1), 1–8. https://doi.org/10.1038/s41598–019-47266-6.

(26) Sathiya, M.; S. Prakash, A.; Ramesha, K.; Tarascon, J.; K. Shukla, A. V2O5-Anchored Carbon Nanotubes for Enhanced Electrochemical Energy Storage. *J. Am. Chem. Soc.* **2011**, *133* (40), 16291–16299. https://doi.org/10.1021/ja207285b.

(27) Perera, S. D.; Patel, B.; Nijem, N.; Roodenko, K.; Seitz, O.; Ferraris, J. P.; Chabal, Y. J.; Balkus, K. J. Vanadium Oxide Nanowire-Carbon Nanotube Binder-Free Flexible Electrodes for Supercapacitors. *Adv. Energy Mater.* **2011**, *1* (5), 936–945. https://doi.org/10.1002/aenm.201100221.

(28) Li, H.-Y.; Jiao, K.; Wang, L.; Wei, C.; Li, X.; Xie, B. Micelle Anchored in Situ Synthesis of V 2 O 3 Nanoflakes@C Composites for Supercapacitors. *J. Mater. Chem. A* **2014**, *2* (44), 18806–18815. https://doi.org/10.1039/C4TA04062G.

(29) El-Kady, M. F.; Ihns, M.; Li, M.; Hwang, J. Y.; Mousavi, M. F.; Chaney, L.; Lech, A. T.; Kaner, R. B. Engineering Three-Dimensional Hybrid Supercapacitors and Microsupercapacitors for High-Performance Integrated Energy Storage. *Proc. Natl. Acad. Sci.* **2015**, *112* (14), 4233–4238. https://doi.org/10.1073/pnas.1420398112.

(30) Wu, Y.; Gao, G.; Wu, G. Self-Assembled Three-Dimensional Hierarchical Porous V 2 O 5 /Graphene Hybrid Aerogels for Supercapacitors with High Energy Density and Long Cycle Life. *J. Mater. Chem. A* **2015**, *3* (5), 1828–1832. https://doi.org/10.1039/C4TA05537C.

(31) Hwang, J. Y.; El-Kady, M. F.; Li, M.; Lin, C. W.; Kowal, M.; Han, X.; Kaner, R. B. Boosting the Capacitance and Voltage of Aqueous Supercapacitors via Redox Charge Contribution from Both Electrode and Electrolyte. *Nano Today* **2017**, *15*, 15–25. https://doi.org/10.1016/j.nantod.2017.06.009.

(32) Hwang, J. Y.; El-Kady, M. F.; Wang, Y.; Wang, L.; Shao, Y.; Marsh, K.; Ko, J. M.; Kaner, R. B. Direct Preparation and Processing of Graphene/RuO2 Nanocomposite Electrodes for High-Performance Capacitive Energy Storage. *Nano Energy* **2015**, *18*, 57–70.

https://doi.org/10.1016/j.nanoen.2015.09.009.

(33) Wang, L. J.; El-Kady, M. F.; Dubin, S.; Hwang, J. Y.; Shao, Y.; Marsh, K.; McVerry, B.; Kowal, M. D.; Mousavi, M. F.; Kaner, R. B. Flash Converted Graphene for Ultra-High Power Supercapacitors. *Adv. Energy Mater.* **2015**, *5* (18), 1500786. https://doi.org/10.1002/aenm.201500786.

(34) Qu, Q.; Zhu, Y.; Gao, X.; Wu, Y. Core-Shell Structure of Polypyrrole Grown on V2O5 Nanoribbon as High Performance Anode Material for Supercapacitors. *Adv. Energy Mater.* **2012**, *2* (8), 950–955. https://doi.org/10.1002/aenm.201200088.

(35) Wu, H.; Qin, M.; Li, X.; Cao, Z.; Jia, B.; Zhang, Z.; Zhang, D.; Qu, X.; Volinsky, A. A. One Step Synthesis of Vanadium Pentoxide Sheets as Cathodes for Lithium Ion Batteries. *Electrochim. Acta* **2016**, *206*, 301–306. https://doi.org/10.1016/j.electacta.2016.04.169.

(36) Dewangan, K.; Sinha, N. N.; Chavan, P. G.; Sharma, P. K.; Pandey, A. C.; More, M. A.; Joag, D. S.; Munichandraiah, N.; Gajbhiye, N. S. Synthesis and Characterization of Self-Assembled Nanofiber-Bundles of V2O5: Their Electrochemical and Field Emission Properties. *Nanoscale* **2012**, *4* (2), 645–651. https://doi.org/10.1039/C1NR11444A.

(37) Liu, Y.; Clark, M.; Zhang, Q.; Yu, D.; Liu, D.; Liu, J.; Cao, G. V2O5 Nano-Electrodes with High Power and Energy Densities for Thin Film Li-Ion Batteries. *Adv. Energy Mater.* **2011**, *1* (2), 194–202. https://doi.org/10.1002/aenm.201000037.

(38) Wang, G.; Lu, X.; Ling, Y.; Zhai, T.; Wang, H.; Tong, Y.; Li, Y. LiCl/PVA Gel Electrolyte Stabilizes Vanadium Oxide Nanowire Electrodes for Pseudocapacitors. *ACS Nano* **2012**, *6* (11), 10296–10302. https://doi.org/10.1021/nn304178b.

(39) Panigrahi, K.; Howli, P.; Chattopadhyay, K. K. Three-Dimensional VO2@PANI Micro Flower Array for Flexible Supercapacitor. *Mater. Lett.* **2019**, *253*, 90–94. https://doi.org/10.1016/j.matlet.2019.06.034.

(40) Wang, F.; Li, Y.; Cheng, Z.; Xu, K.; Zhan, X.; Wang, Z.; He, J. Construction of 3D V2O5/Hydrogenated-WO3 Nanotrees on Tungsten Foil for High-Performance Pseudocapacitors. *Phys. Chem. Chem. Phys.* **2014**, *16* (24), 12214. https://doi.org/10.1039/c4cp01200c.

(41) Hua, L.; Ma, Z.; Shi, P.; Li, L.; Rui, K.; Zhou, J.; Huang, X.; Liu, X.; Zhu, J.; Sun, G.; et al. Ultrathin and Large-Sized Vanadium Oxide Nanosheets Mildly Prepared at Room Temperature for High Performance Fiber-Based Supercapacitors. *J. Mater. Chem. A* **2017**, *5* (6), 2483–2487. https://doi.org/10.1039/C6TA10619F.

(42) Xiao, X.; Peng, X.; Jin, H.; Li, T.; Zhang, C.; Gao, B.; Hu, B.; Huo, K.; Zhou, J. Freestanding Mesoporous VN/CNT Hybrid Electrodes for Flexible All-Solid-State Supercapacitors. *Adv. Mater.* **2013**, *25* (36), 5091–5097. https://doi.org/10.1002/adma.201301465.

(43) Cheng, C.-J.; Bao, S.-J.; Li, C. M. A Facile and Well-Tailored Vanadium Oxide Porous Network for High-Capacity Electrochemical Capacitive Energy Storage. *Mater. Lett.* **2014**, *120*, 283–286. https://doi.org/10.1016/j.matlet.2014.01.111.

(44) Mai, L.; Xu, X.; Han, C.; Luo, Y.; Xu, L.; Wu, Y. A.; Zhao, Y. Rational Synthesis of Silver Vanadium Oxides/Polyaniline Triaxial Nanowires with Enhanced Electrochemical Property. *Nano Lett.* **2011**, *11* (11), 4992–4996. https://doi.org/10.1021/nl202943b.

(45) Wei, D.; Scherer, M. R. J.; Bower, C.; Andrew, P.; Ryhänen, T.; Steiner, U. A

Nanostructured Electrochromic Supercapacitor. *Nano Lett.* **2012**, *12* (4), 1857–1862. https://doi.org/10.1021/nl2042112.

(46) Lee, S.-H.; Cheong, H. M.; Liu, P.; Tracy, C. E. Improving the Durability of Amorphous Vanadium Oxide Thin-Film Electrode in a Liquid Electrolyte. *Electrochem. Solid-State Lett.* **2003**, *6* (6), A102. https://doi.org/10.1149/1.1567533.

(47) Liu, Z.; Zhang, H.; Yang, Q.; Chen, Y. Graphene / V2O5 Hybrid Electrode for an Asymmetric Supercapacitor with High Energy Density in an Organic Electrolyte. *Electrochim. Acta* **2018**, *287*, 149–157. https://doi.org/10.1016/j.electacta.2018.04.212.

(48) Liu, D.; Liu, Y.; Candelaria, S. L.; Cao, G.; Liu, J.; Jeong, Y.-H. Atomic Layer Deposition of Al 2 O 3 on V 2 O 5 Xerogel Film for Enhanced Lithium-Ion Intercalation Stability. *J. Vac. Sci. Technol. A Vacuum, Surfaces, Film.* **2012**, *30* (1), 01A123. https://doi.org/10.1116/1.3664115.

(49) Noori, A.; El-Kady, M. F.; Rahmanifar, M. S.; Kaner, R. B.; Mousavi, M. F. Towards Establishing Standard Performance Metrics for Batteries, Supercapacitors and Beyond. *Chem. Soc. Rev.* **2019**, *48* (5), 1272–1341. https://doi.org/10.1039/C8CS00581H.

(50) Peng, X.; Liu, H.; Yin, Q.; Wu, J.; Chen, P.; Zhang, G.; Liu, G.; Wu, C.; Xie, Y. A Zwitterionic Gel Electrolyte for Efficient Solid-State Supercapacitors. *Nat. Commun.* **2016**, *7* (1), 11782. https://doi.org/10.1038/ncomms11782.

(51) Yilmaz, G.; Lu, X.; Ho, G. W. Cross-Linker Mediated Formation of Sulfur-Functionalized V 2 O 5 /Graphene Aerogels and Their Enhanced Pseudocapacitive Performance. *Nanoscale* **2017**, *9* (2), 802–811. https://doi.org/10.1039/C6NR08233E.

(52) Bai, M.-H.; Liu, T.-Y.; Luan, F.; Li, Y.; Liu, X.-X. Electrodeposition of Vanadium Oxide–Polyaniline Composite Nanowire Electrodes for High Energy Density Supercapacitors. *J. Mater. Chem. A* **2014**, *2* (28), 10882–10888. https://doi.org/10.1039/C3TA15391F.

(53) Cheng, Y.; Lu, S.; Zhang, H.; Varanasi, C. V.; Liu, J. Synergistic Effects from Graphene and Carbon Nanotubes Enable Flexible and Robust Electrodes for High-Performance Supercapacitors. *Nano Lett.* **2012**, *12* (8), 4206–4211. https://doi.org/10.1021/nl301804c.

(54) Khalid, S.; Cao, C.; Wang, L.; Zhu, Y. Microwave Assisted Synthesis of Porous NiCo2O4 Microspheres: Application as High Performance Asymmetric and Symmetric Supercapacitors with Large Areal Capacitance. *Sci. Rep.* **2016**, *6* (1), 22699. https://doi.org/10.1038/srep22699.

(55) Zhai, T.; Lu, X.; Ling, Y.; Yu, M.; Wang, G.; Liu, T.; Liang, C.; Tong, Y.; Li, Y. A New Benchmark Capacitance for Supercapacitor Anodes by Mixed-Valence Sulfur-Doped V 6 O 13− X. *Adv. Mater.* **2014**, *26* (33), 5869–5875. https://doi.org/10.1002/adma.201402041.

(56) Choudhury, A.; Bonso, J. S.; Wunch, M.; Yang, K. S.; Ferraris, J. P.; Yang, D. J. In-Situ Synthesis of Vanadium Pentoxide Nanofibre/Exfoliated Graphene Nanohybrid and Its Supercapacitor Applications. *J. Power Sources* **2015**, *287*, 283–290. https://doi.org/10.1016/j.jpowsour.2015.04.062.

(57) Patil, S. S.; Dubal, D. P.; Deonikar, V. G.; Tamboli, M. S.; Ambekar, J. D.; Gomez-Romero, P.; Kolekar, S. S.; Kale, B. B.; Patil, D. R. Fern-like RGO/BiVO4 Hybrid Nanostructures for High-Energy Symmetric Supercapacitor. *ACS Appl. Mater. Interfaces* **2016**, *8* (46), 31602–31610. https://doi.org/10.1021/acsami.6b08165.

(58) Lu, X.; Yu, M.; Zhai, T.; Wang, G.; Xie, S.; Liu, T.; Liang, C.; Tong, Y.; Li, Y. High

Energy Density Asymmetric Quasi-Solid-State Supercapacitor Based on Porous Vanadium Nitride Nanowire Anode. *Nano Lett.* **2013**, *13* (6), 2628–2633. https://doi.org/10.1021/nl400760a.

(59) El-Kady, M. F.; Strong, V.; Dubin, S.; Kaner, R. B. Laser Scribing of High-Performance and Flexible Graphene-Based Electrochemical Capacitors. *Science (80-.).* **2012**, *335* (6074), 1326–1330. https://doi.org/10.1126/science.1216744.

(60) Pech, D.; Brunet, M.; Durou, H.; Huang, P.; Mochalin, V.; Gogotsi, Y.; Taberna, P.-L.; Simon, P. Ultrahigh-Power Micrometre-Sized Supercapacitors Based on Onion-like Carbon. *Nat. Nanotechnol.* **2010**, *5* (9), 651–654. https://doi.org/10.1038/nnano.2010.162.

(61) Hummers, W. S.; Offeman, R. E. Preparation of Graphitic Oxide. *J. Am. Chem. Soc.* **1958**, *80* (6), 1339–1339. https://doi.org/10.1021/ja01539a017.

(62) Chen, M.; Zhang, Y.; Liu, Y.; Wang, Q.; Zheng, J.; Meng, C. Three-Dimensional Network of Vanadium Oxyhydroxide Nanowires Hybridize with Carbonaceous Materials with Enhanced Electrochemical Performance for Supercapacitor. *ACS Appl. Energy Mater.* **2018**, *1* (10), 5527–5538. https://doi.org/10.1021/acsaem.8b01109.

Supporting Information

Calculations

The specific capacitance of an electrode measured via cyclic voltammetry (CV) or via galvanostatic charge/discharge (GCD) in a three-electrode setup was calculated using the following equations:

$$C_{specific} = \frac{\int i\,dV}{\nu \times V \times x} \quad (1)$$

$$C_{specific} = \frac{2 \times i \times \int V\,dt}{x \times |V_f{}^2 - V_i{}^2|} \quad (2)$$

where $\int i\,dV$ is the integration of the discharge half of the CV curve, V is the potential, ν is the scan rate, x is either the active material mass or the active electrode area, t is the discharge time, and V_i and V_f are the initial and final potentials, respectively.

For two-electrode systems, the gravimetric or areal device capacitance is calculated by

$$C_{device} = \frac{\int i\,dV}{\nu \times V \times 2m} \text{ or } C_{device} = \frac{i \times \int V\,dt}{m \times |V_f{}^2 - V_i{}^2|} \quad (3)$$

where m is the active material mass.

The volumetric device capacitance is calculated by

$$C_{device} = \frac{\int i\,dV}{\nu \times V \times y} \text{ or } C_{device} = \frac{2 \times i \times \int V\,dt}{y \times |V_f{}^2 - V_i{}^2|} \quad (4)$$

where y is the total volume of the two electrodes, two current collectors, electrolyte, and separator, or the geometric area of the active material,

The device energy density and power density are calculated using the following equations:

$$E\ (Wh\ kg^{-1}) = \frac{1}{2} \times C_{device} V^2 \times \frac{1\ h}{3600\ s} \times \frac{1\ 000}{1\ kg} \quad (5)$$

$$P\ (W\ kg^{-1}) = \frac{E}{t} \quad (6)$$

	Thickness / µm	Volume %	Areal mass loading / mg cm^{-2}	Weight %
LSG/VO_x	15	52.6	0.302	14.7
Current collector	10	35.1	1.357	66.0
Separator	7	12.3	0.797	19.4
Device total	57	47.4	4.115	100.0

Table S2-1. Thickness and areal mass loading of active material, current collector, and separator in LSG/VO_x SSCs.

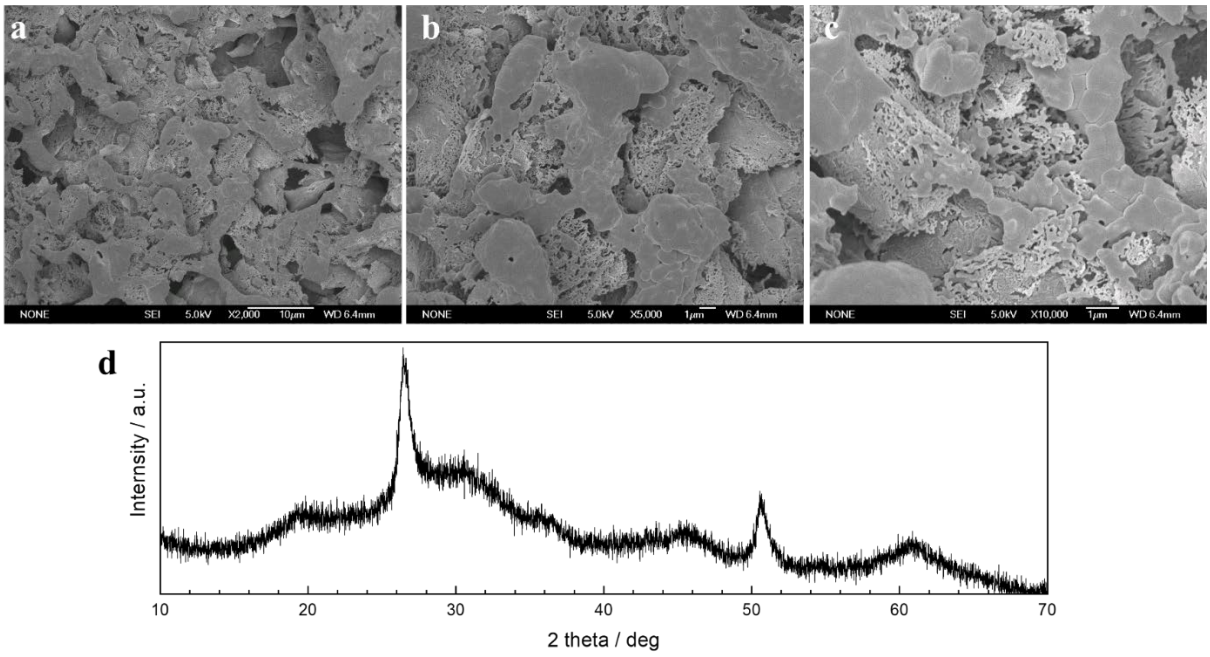

Figure S2-1. Characterization of the GO/VCl_3 film. (a-c) Low- and high-magnification SEM images of the GO/VCl_3 film. (d) XRD pattern of the GO/VCl_3 film.

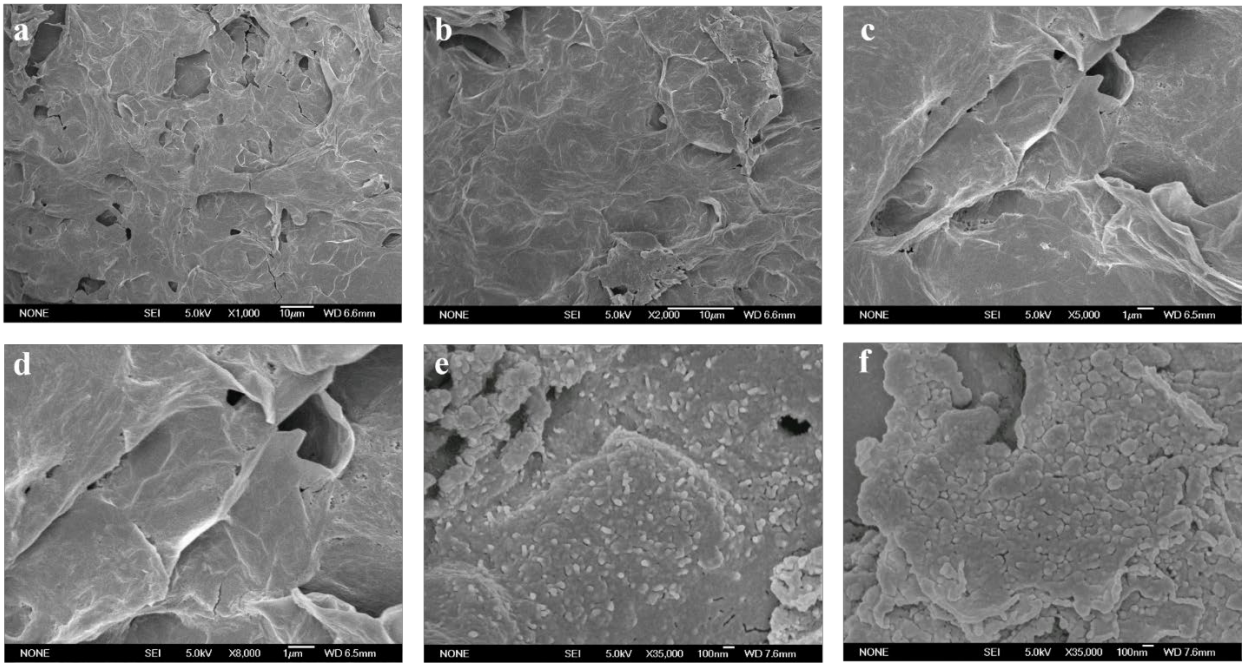

Figure S2-2. Low- and high-magnification SEM images of the LSG/VO_x composite electrode.

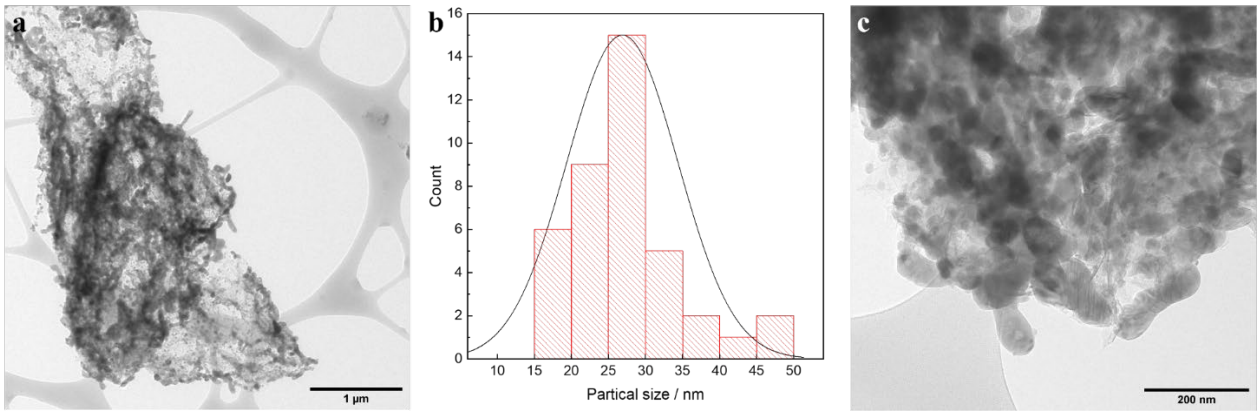

Figure S2-3. (a) A TEM image showing VO_x particles on a graphene sheet. (b) A plot showing the size distribution of VO_x particles based on **Figure 2-2.c**. (c) A higher-magnification TEM image of the VO_x network.

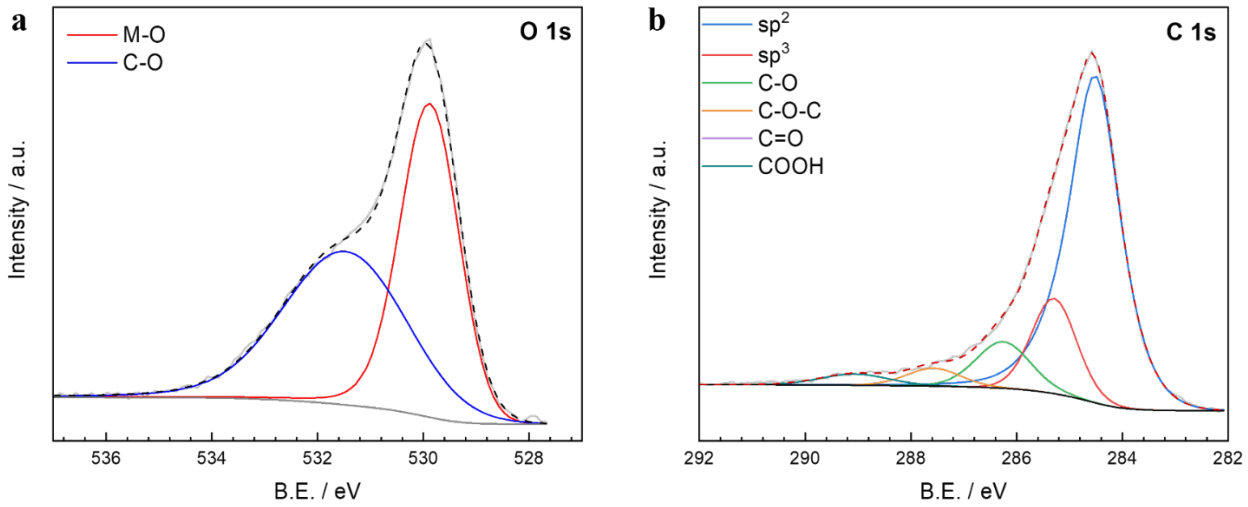

Figure S2-4. XPS (a) O 1s and (b) C 1s spectra of the LSG/VO_x composite.

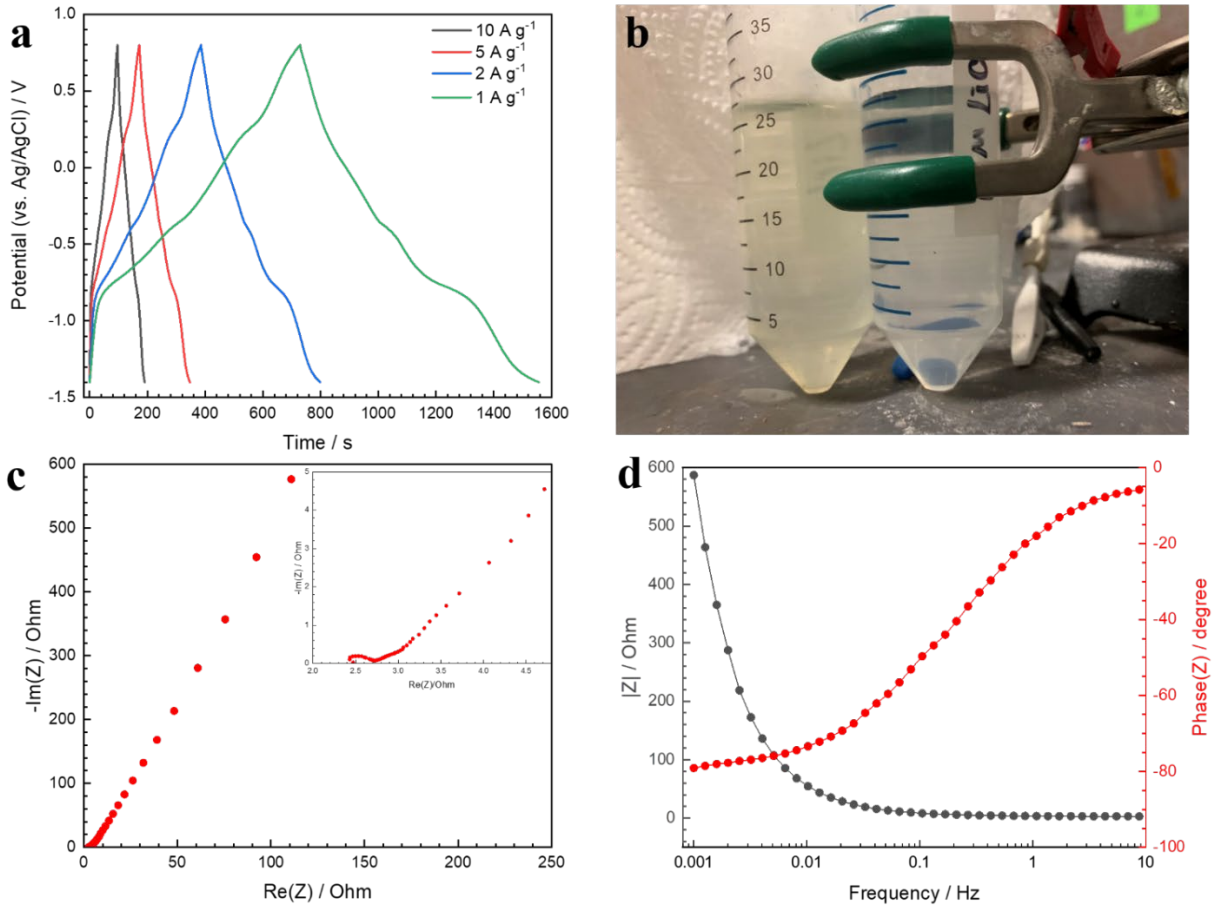

Figure S2-5. (a) GCD curves of an aqueous LSG/VO_x at 1, 2, 5, 10 A g^{-1} in a three-electrode setup. (b) Photos of the electrolyte after measurement (left) and fresh electrolyte (right). (c and d) Nyquist and Bode impedance plots of LSG/VO_x.

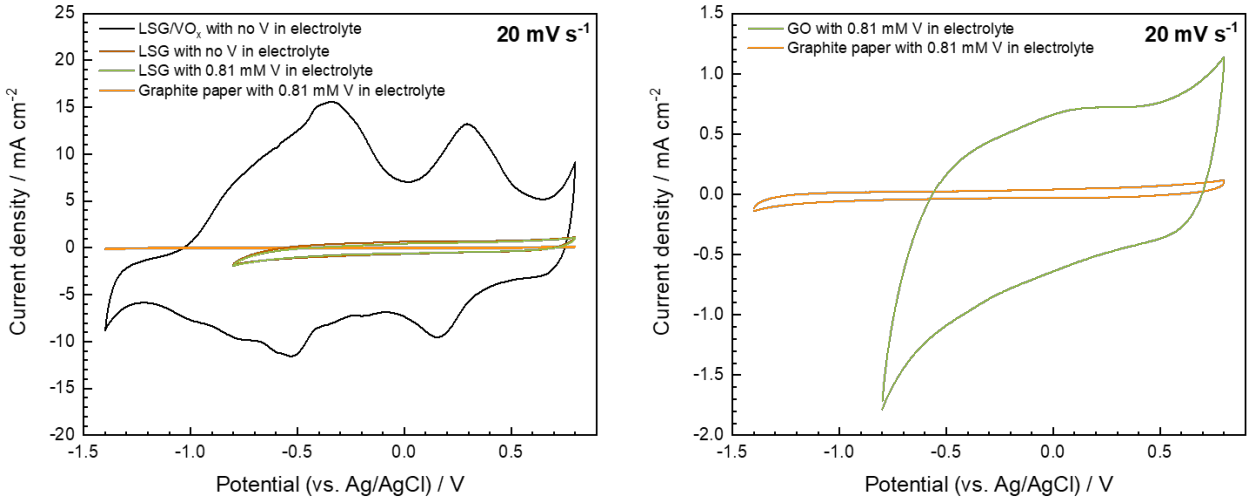

Figure S2-6. (a) CV of LSG/VO_x and LSG in 10 M LiCl compared to that of LSG and graphite paper in an electrolyte of 0.81 mM VCl_3 and 10 M LiCl at 20 mV s^{-1}. (b) CV of LSG and graphite paper in an electrolyte of 0.81 mM VCl_3 and 10 M LiCl at 20 mV s^{-1}(zoomed-in version of **Figure S2-6a.**).

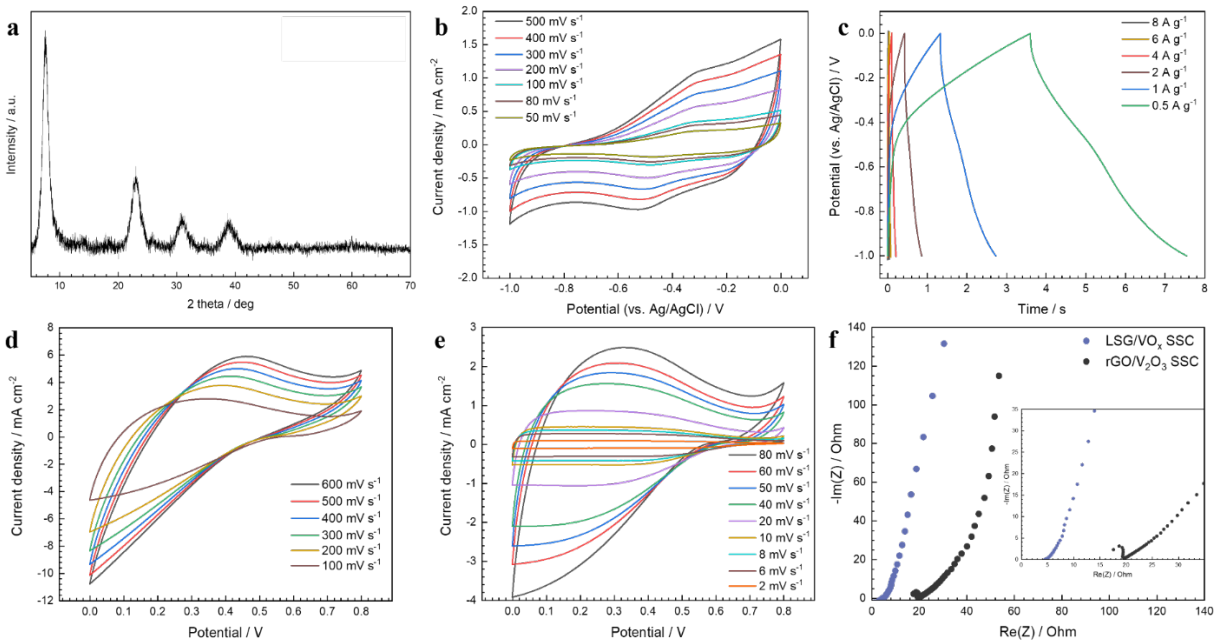

Figure S2-7. (a) XRD pattern of the rGO/V_2O_3 mixture matching $V_2O_5 \cdot 1.6\ H_2O$ (JCPDS no. 40–1296) (a) CV curves of the rGO/V_2O_3 electrode at 500, 400, 300, 200, 100, 80, 50 mV s^{-1} in a 3-electrode setup. (c) GCD curves of the rGO/V_2O_3 electrode at 8 ,6, 4, 2, 1, 0.5 A g^{-1} in a 3-electrode setup. (d-e) CV curves of the rGO/V_2O_3 SSC at various scan rate. (f) Nyquist impedance plot of LSG/VO_x and rGO/V_2O_3 electrodes with the high-frequency region shown in the inset.

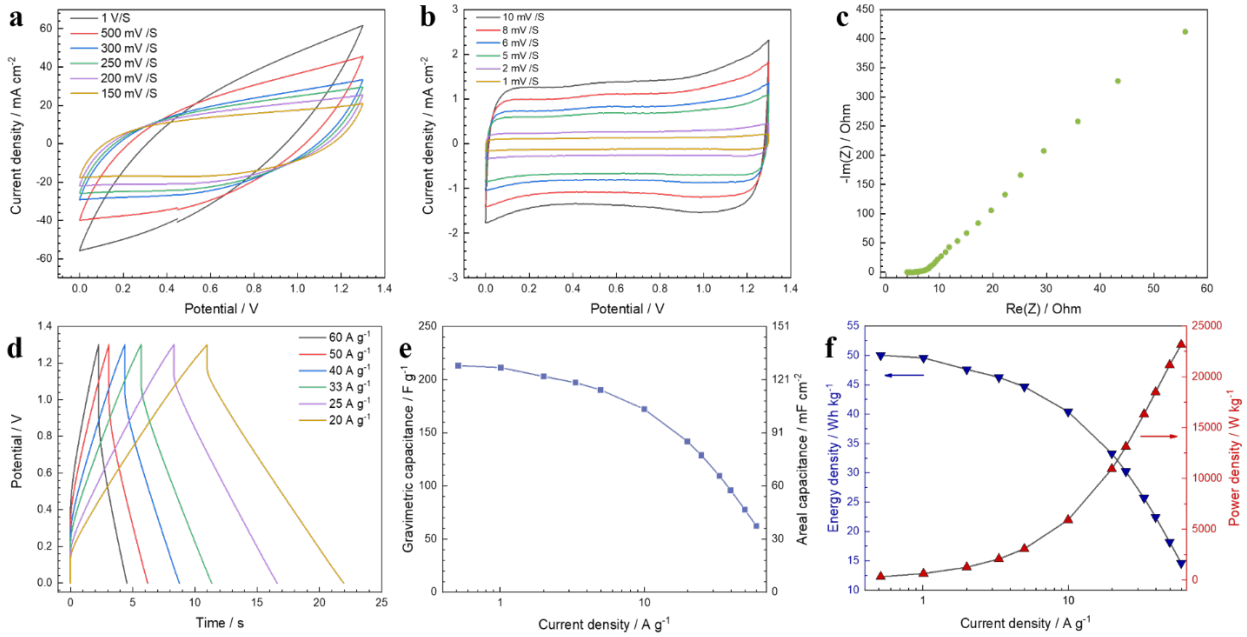

Figure S2-8. Electrochemical measurements of an aqueous 10 M LiCl LSG/VO_x symmetric supercapacitor (SSC). (a) CV curves of an aqueous LSG/VO_x SSC at 1000, 500, 300, 250, 200, 150 mV s^{-1}. (b) CV curves of an aqueous LSG/VO_x SSC at 10, 8, 6, 5, 2, 1 mV s^{-1}. (c) Nyquist plot of an LSG/VO_x SSC. (d) GCD curves of an aqueous LSG/VO_x SSC at 60, 50, 40, 33, 25, 20 A g^{-1}. (e) Gravimetric and areal capacitance of an aqueous LSG/VO_x SSC at various current densities. (f) Gravimetric energy and power densities of an aqueous LSG/VO_x SSC at various current densities.

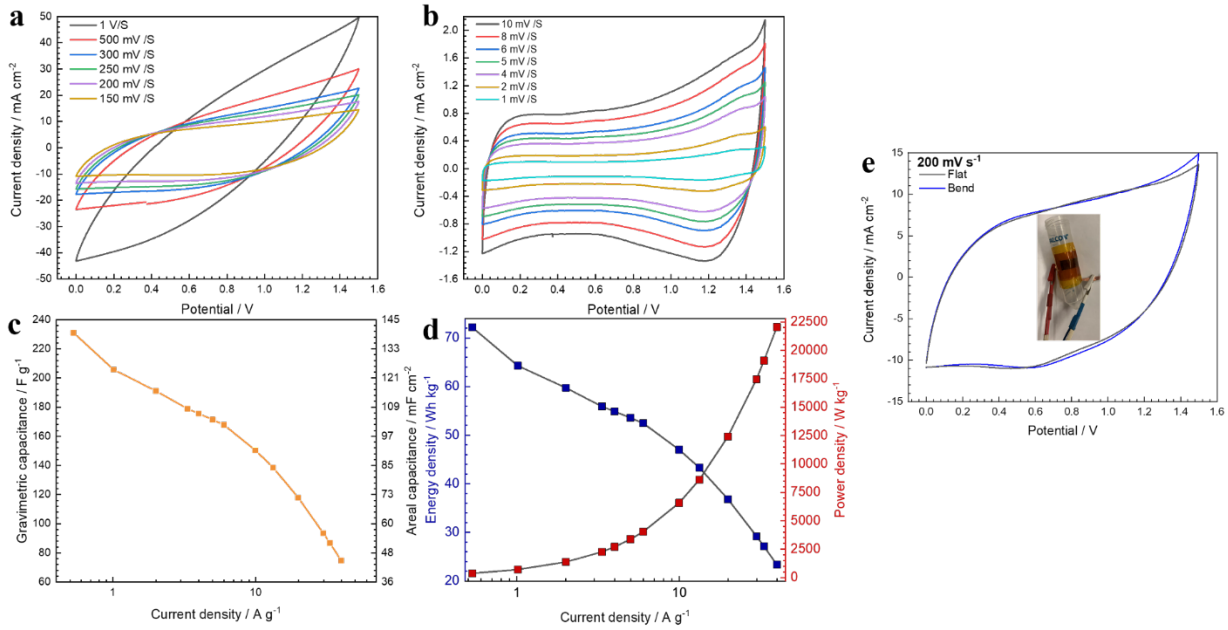

Figure S2-9. Electrochemical measurements of an quasi-solid-state LiCl/PVA LSG/VO_x SSC. (a) CV curves of an aqueous LSG/VO_x SSC at 1000, 500, 300, 250, 200, 150 mV s^{-1}. (b) CV curves of an aqueous LSG/VO_x SSC at 10, 8, 6, 5, 2, 1 mV s^{-1}. (c) The gravimetric and areal capacitance of an aqueous LSG/VO_x SSC at various current densities. (d) Gravimetric energy and power densities of an aqueous LSG/VO_x SSC at various current densities. (e) CV curves of an quasi-solid-state LSG/VO_x SSC when flat and bent; the inset is a photo of an SSC bent around a 50 mL Falcon tube.

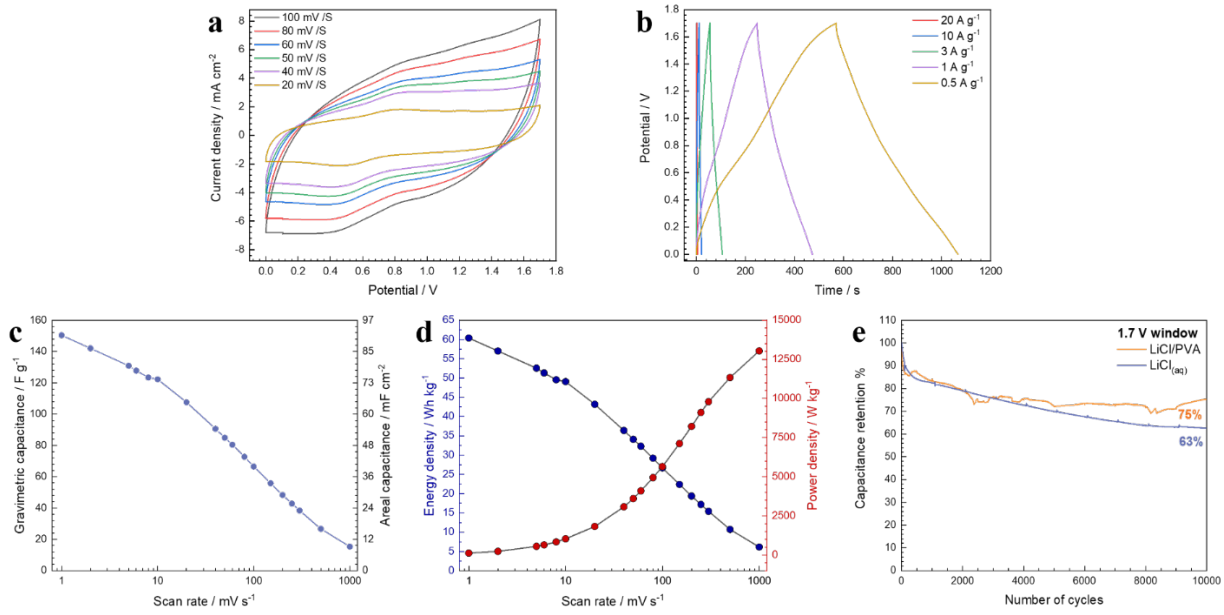

Figure S2-10. Electrochemical measurements of a 1.7 V quasi-solid-state LSG/VO_x SSC. (a) CV curves of an aqueous LSG/VO_x SSC at 20, 40, 50, 60, 100 mV s^{-1}. (b) GCD curves of an aqueous LSG/VO_x SSC at 0.5, 1, 3, 10, 20 A g^{-1}. (c) Gravimetric and areal capacitance of an aqueous LSG/VO_x SSC at various scan rates. (d) Gravimetric energy and power densities of an aqueous LSG/VO_x SSC at various scan rates. (e) Long-term stability of an aqueous LSG/VO_x SSC after 10,000 cycles, in comparison to the aqueous system.

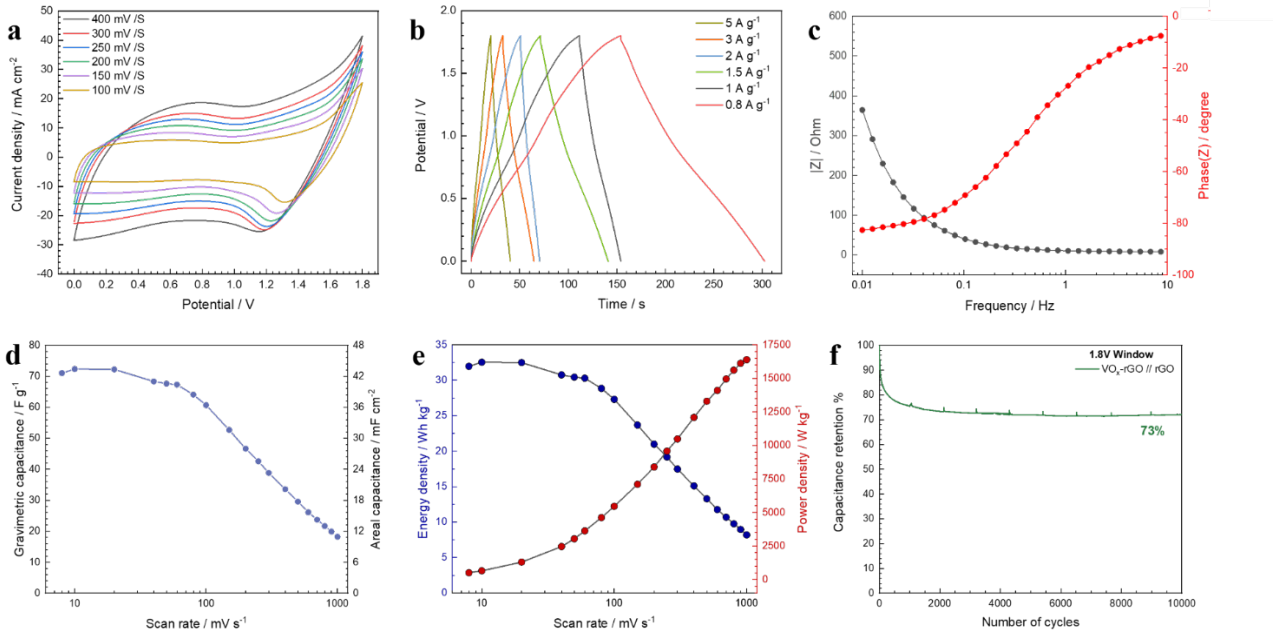

Figure S2-11. Electrochemical measurements of an aqueous 10 M LiCl rGO//LSG/VO_x asymmetric supercapacitor (ASC). (a) CV curves of an aqueous rGO//LSG/VO_x ASC at 400, 300, 250, 200, 150, 100 mV s^{-1}. (b) GCD curves of an aqueous rGO//LSG/VO_x ASC at 0.8, 1, 1.5, 2, 3, 5 A g^{-1}. (c) Bode plot of an aqueous rGO//LSG/VO_x ASC. (d) Gravimetric and areal capacitance of an aqueous LSG/VO_x SSC at various scan rates. (e) Gravimetric energy and power densities of an aqueous rGO//LSG/VO_x ASC at various scan rates. (f) Long-term stability of an aqueous LSG/VO_x SSC after 10,000 cycles.

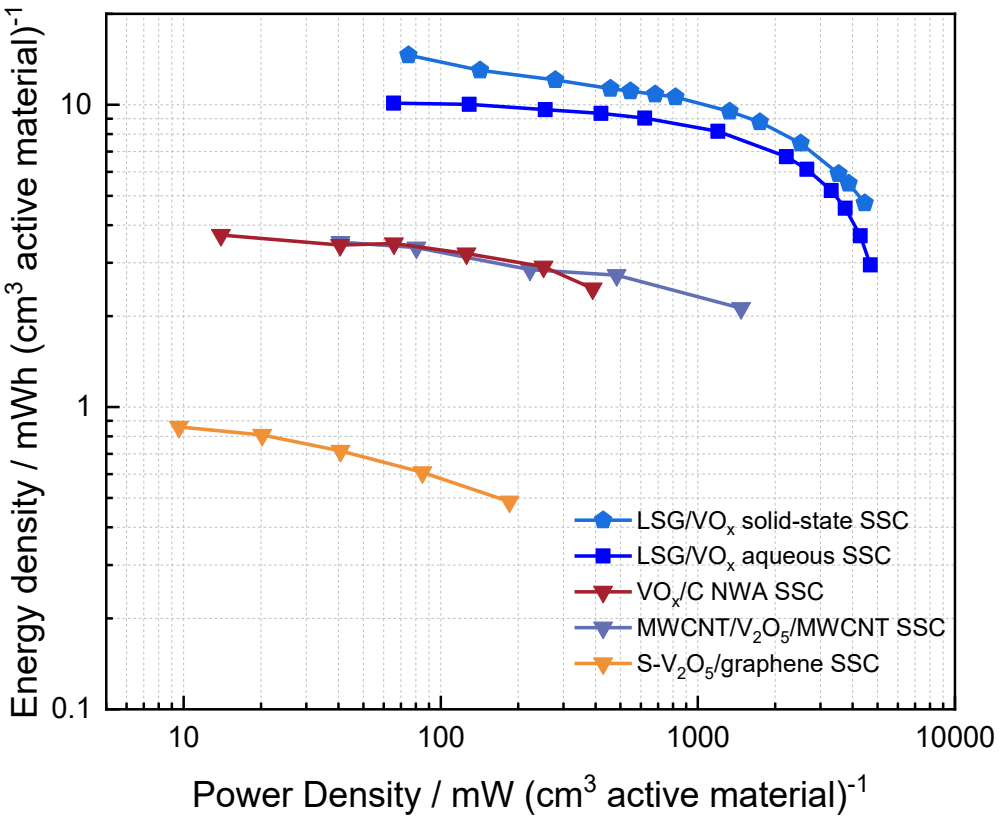

Figure S2-12. A Ragone plot comparing the volumetric energy and power densities of LSG/VO_x symmetric supercapacitors to other vanadium oxide systems reported in the literature, normalized to active material volume.[1–3]

TGA analysis

We also did TGA measurement to determine the weight% of VO_x in the active material at a rate of 5 °C min^{-1} in air, as shown in the Figure below. Between 350 °C and 650 °C, the sample weight increases by about 12%, which accounts for the loss of GO and the oxidation of VO_x to V_2O_5. Since both events occur in the same region, only an estimate can be obtained. According the XPS results, the three main oxidation states are +2, +3, +4 and +5, with at. % of 12.6, 69.9, 14.3 and 3.2, respectively, as summarized in the table below:

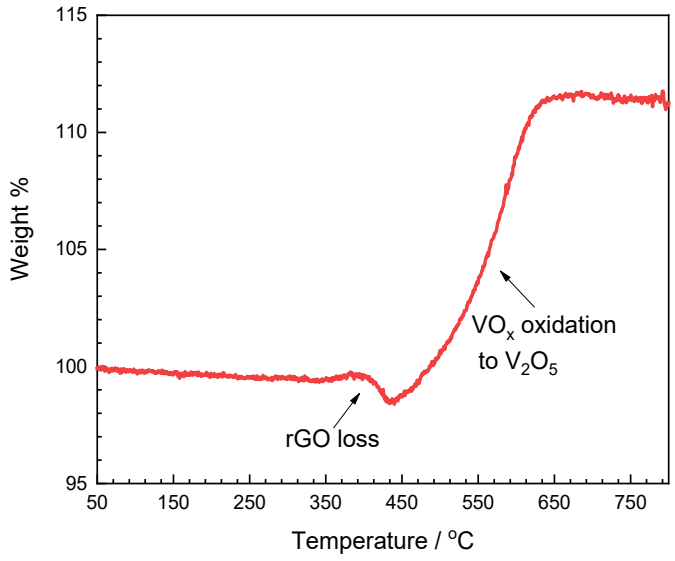

VO_x	Ox. state	at. %	MW / g mol^{-1}
VO	+2	12.6	66.94
$VO_{1.5}$	+3	69.9	74.94
VO_2	+4	14.3	82.94
$VO_{2.5}$	+5	3.2	90.94

Assuming this ratio, the effective molecular weight of VO_x is calculated to be 75.59 g mol^{-1}. Using the equation below:

$$\frac{100 - m_{LSG}\%}{12 + m_{LSG}\%} = \frac{75.59}{90.94 - 75.59}$$

The weight% of LSG ($m_{LSG}\%$) is determined to be 6.82% and that of VO_x is determined to be 93.18%.

Supporting Information References

[1] Z.-H. Huang, Y. Song, X.-X. Liu, *Chem. Eng. J.* **2019**, *358*, 1529.

[2] G. Yilmaz, X. Lu, G. W. Ho, *Nanoscale* **2017**, *9*, 802.

[3] L. Hua, Z. Ma, P. Shi, L. Li, K. Rui, J. Zhou, X. Huang, X. Liu, J. Zhu, G. Sun, W. Huang, *J. Mater. Chem. A* **2017**, *5*, 2483.

Chapter 3. A Laser-Scribed Vanadium Oxide Cathode for Ultra-Fast Zinc-Ion Energy Storage

Abstract

Aqueous zinc-ion storage is promising for large-scale energy storage applications, but is plagued by the lack of high-performance cathode materials that can simultaneously enable high specific capacity, ultra-fast charging, and outstanding cycling stability. In this work, we design a novel laser-scribed nano-vanadium oxide (LNVO) cathode with Faradaic pseudocapacitive response. This material stores charges through Faradaic redox reactions on/near the surface at fast rates owing to its small grain size, displaying a notable surface-controlled capacity contribution (90%-98%). Benefitting from this, a high specific capacity of 490 mAh g^{-1} can be achieved by the LNVO/Zn system at 0.5 A g^{-1} and impressively 54% (264 mAh g^{-1}) can be retained at 100 A g^{-1} with a 10 s charge/discharge cycle, showing excellent rate capability. The LNVO/Zn is also capable of reaching >90% capacity retention after 3000 cycles at a remarkably high rate of 30 A g^{-1}, as well as achieving both high energy (396 Wh kg^{-1}) and power densities (56,306 W kg^{-1}). Multiple characterization techniques unambiguously reveal a charge storage mechanism by zinc and hydronium ion co-insertion. Moreover, when the LNVO cathode is integrated into quasi-solid-state zinc-ion batteries, the super-stable flexible device also exhibits great mechanical stability, demonstrating its promising prospects for both grid-scale and flexible energy storage systems.

Introduction

Due to the accelerating hazards posed by climate change, concerted international efforts aim to achieve net-zero emissions by 2050, indicating the need for swift and fundamental changes in the global energy landscape. One of the priority areas that requires immediate technological advances is grid-scale energy storage. According to the International Energy Agency (IEA), although pumped-storage hydropower remains the most widely used grid-scale storage technology, grid-scale batteries are rapidly progressing, and lithium-ion batteries (LIB) take the lead in all new battery capacity installed in 2021.[1] Despite their high energy density and well-developed manufacturing methods, LIBs cause concerns in safety, cyclability and cost that are critical to large-scale stationary storage.[2–4] Aqueous rechargeable batteries with attractive properties of low cost and being environmentally benign have emerged as promising solutions for grid-scale electrochemical energy storage.[5] Among them, zinc-ion batteries (ZIBs) have received increasing research interest due to their merits such as abundant reserves, divalent charge, low redox potential and compatibility with mild pH electrolytes. [6,7]

Although a Zn metal anode has a high theoretical capacity of 820 mAh g^{-1} and can be produced on a large scale, it remains challenging to find cathode materials that simultaneously possess the following attributes: (i) high specific capacity, (ii) fast charging capability, (iii) structural stability upon cycling and (iv) can be made by a scalable synthesis. Herein, we propose a cathode design based on pseudocapacitive vanadium oxides. Unlike the conventional capacitor-type and battery-type materials that are limited by either low energy or low power density, pseudocapacitance relies on Faradaic reactions that are confined to the surface (or near the surface) and occur at rates comparable to non-Faradaic processes like electric double layer formation, bridging the gap between traditional materials.[8] Vanadium oxides (VO_x) are not intrinsically pseudocapacitive and

nanosizing is required to achieve extrinsic pseudocapacitance.[9] In this work, we present a nanoengineered nano-vanadium oxide (LNVO) cathode for zinc-ion storage, which is synthesized by a scalable laser-scribing/calcination method that results in VO_x nanoparticles anchored on a conductive graphene scaffold. As illustrated in **Figure 3-8**, the LNVO/Zn battery stores charges via ultra-fast Faradaic redox reactions in which 90 – 98% of the capacity originates from surface-controlled contributions, thanks to the small grain size of the VO_x nanoparticles. A remarkable specific capacity of 490 mAh g^{-1} can be achieved at 0.5 A g^{-1} with a record rate capability signified by 264 mAh g^{-1} capacity gained within 10 s upon 100 A g^{-1} charging/discharging. Exceptional high-rate cycling stability has been achieved with capacity retention reaching 92% (of the initial 434 mAh g^{-1}) after 3,000 cycles at 30 A g^{-1} and 85% (of the initial 329 mAh g^{-1}) 329 mAh g^{-1} after 1,500 cycles at 50 A g^{-1}. The charge storage mechanism is investigated with multiple techniques, revealing a hydronium ion-facilitated Zn ion co-insertion pathway where minimal structural changes have been observed upon cycling. Furthermore, the fabricated zinc-ion battery exhibits LIB-level energy density (up to 396 Wh kg^{-1}) and capacitor-level power density (up to 56306 W kg^{-1}) with commercially favorable areal capacity and excellent temperature endurance. Moreover, the quasi-solid-state LNVO/Zn device fabricated in a polymer gel electrolyte also shows outstanding electrochemical performance during mechanical deformations and long-term cycling. Therefore, the LNVO cathode presents high specific capacity, fast charging behavior, cycling stability and durability in practical uses, which are ideal features for grid-scale energy storage applications.

Results and discussion

Synthesis and characterization

The laser-scribed nano-VO_x (LNVO) film consisting of redox-active VO_x nanoparticles and a reduced graphene oxide (rGO) conductive scaffold was fabricated by an improved laser-scribing method from a previously reported procedure with further calcination treatment to increase the uniformity (**See Methods**).[10] Briefly, a dried film cast from a VCl_3/graphite oxide (GO) precursor mixture was laser-scribed and subsequently calcined at 300 °C for 1 hour. The as-synthesized LNVO shows the well indexed diffraction peaks shown in **Figure 3-9a**, which illustrates that the LNVO film is mostly orthorhombic V_2O_5 (JCPDS: 00-041-1426) accompanied by VO_2 (JCPDS: 00-044-0252). The V_2O_5 and VO_2 phases, respectively, adopt layered and channel-like structures that can provide multiple diffusion pathways and enable fast ion conduction. A broad graphitic peak at 26.4° confirms the existence of rGO, which provides enhanced electron transport in the LNVO film. X-ray photoelectron spectroscopy (XPS) was used to characterize the chemical valences and bonding information. The peaks of V 2p can be deconvoluted into the V^{5+} signal ($2p_{3/2}$: 517.7 eV) accompanied by a V^{4+} component ($2p_{3/2}$: 516.5 eV), showing that V is multivalent with 67% V^{5+} and 33% V^{4+} content (**Figure 3-9b**), suggesting that the effective chemical formula of the nano-VO_x is $VO_{2.34}$. The peaks of the O 1s core level can be fit into three peaks located at 530.5, 531.5, and 532.7 eV, representing V-O-V, C=O, and C-O bonds, respectively (**Figure S3-13a**). V-O-V accounting for 70% corresponds well with thermogravimetry analysis (TGA), implying the weight ratio of active material (LNVO) is around 70 wt.% in the as-prepared sample. Both X-ray diffraction (XRD) and XPS measurements confirm the formation of multivalent vanadium oxide from the designed synthesis.

Scanning electron microscope (SEM) images of the sample are given in **Figure 3-9c-d**, where highly-exposed rGO sheets with rough surfaces can be seen with nano-VO_x particles embedded in this hierarchically porous structure. This provides abundant surface-active sites and more diffusion pathways, boosting fast kinetics in electrochemical reactions. A transmission electron microscope (TEM) image (**Figure 3-9e**) also displays ultrathin rGO nanosheets as scaffold. The VO_x nanoparticles with the size range from 2-6 nm are uniformly distributed on the surface (**Figure 3-9f, Figure S3-14**). High-resolution TEM (HRTEM) images in **Figure 3-9g-h** reveal the interlayer distance of 0.44 nm and 0.33 nm, which correspond to the (001) and (-201) planes of V_2O_5 and VO_2, respectively. The selected area electron diffraction (SAED) results can also be indexed to these two species (**Figure S3-14**). Energy dispersive spectroscopy (EDS) mapping (**Figure 3-9i**) shows that C, V, and O are uniformly distributed in the LNVO. Overall, all evidence indicates the successful synthesis of LNVO with a nanostructure that facilitates intercalation stress relieving during charge/discharge that provides finite diffusion space confined on/near the surface. Therefore, the redox processes are expected not to be limited by bulk diffusion and resemble capacitive processes, which provides a great foundation for fast-charging applications.

Electrochemical performance

To analyze the electrochemical kinetics of the LNVO cathode material, cyclic voltammetry (CV) curves at a voltage range of 0.3-1.6 V were recorded and are displayed in **Figure 3-10a**. The two pairs of peaks in the CV and the plateaus in galvanostatic charging/discharging (GCD) suggest that reversible Faradaic reactions occur in the charge storage process. The peak current response (i) can be divided into two separate contributions (battery-like diffusion-controlled and capacitor-like

surface-controlled charge-storage processes), and is related to the scan rate (v) by an empirical power-law relationship as described in the following formula: [11,12]

$$i = a\, v^b$$

where a and b are experimentally determined constants where b = 0.5 stands for a diffusion-controlled charge-storage process, while b = 1.0 signifies a surface-controlled capacitive charge-storage process. The as fit b values for these four redox peaks are 0.92, 0.99, 1.01, 0.92, which are all close to 1 for the LNVO film over a wide range of sweep rates from 0.2 to 2 mV s^{-1} (**Figure 3-10b**), signifying that the electrochemical reaction is almost all surface-controlled and not limited by diffusion-controlled processes throughout the whole operating potential range. As a comparison, asymmetric peak intensities and much lower b values (0.23, 0.82, 0.72, 0.43) have been observed for bulk V_2O_5 (BVO) (**Figure S3-15**). A mixture of diffusion- and surface-controlled process behavior for BVO suggests that the Faradaic pseudocapacitive response of LNVO arises from the nanostructure derived from a combination of the laser scribing and calcination processes. The calculated current contributions from these two types of processes follows:

$$i = k_1 v + k_2 v^{\frac{1}{2}}$$

where k_1 and k_2 are the proportionality constants of surface- and diffusion-controlled contributions respectively. With increasing scan rates, the ratio of capacitance-type charge storage for LNVO increases from 90% at 0.2 mV s^{-1}, to 93% at 1 mV s^{-1} and reaches 98% at 2 mV s^{-1} (**Figure 3-10c**). It is worth noting that these reported b-values for LNVO are among the highest compared to previous literature values in the zinc-ion storage area, meaning intrinsically non-capacitive vanadium oxide exhibits a pseudocapacitive nature in this work. Collectively, high b values and high surface-controlled capacity contributions suggest that although the charge-storage

of the LNVO film is confined to the cathode surface and occurs with ultrafast pseudocapacitive kinetics, the charge storage mechanism is Faradaic in nature, leading to fast-charging zinc-ion energy storage.

To evaluate the fast-charging zinc-ion storage performance, the rate capability and cycle life tests under high current densities were conducted. To exclude the capacity contributions of the rGO scaffold and graphite paper substrate, cells with these two carbon materials as cathodes were galvanostatically cycled at 0.1 A g^{-1}, and the capacity contributions from the scaffold and substrate alone were found to be negligible compared with the LNVO film (**Figure S3-16b**). The rate performances of LNVO and BVO cathodes are illustrated in **Figure 3-10d** and **Table S2** with the current density increasing stepwise from 0.5 to 100 A g^{-1} and then decreasing back to 0.5 A g^{-1}. LNVO shows an outstanding specific capacity of 490 mAh g^{-1} at 0.5 A g^{-1}, which is among the highest reported to the best of our knowledge. Notably, high specific capacities of 363 and 328 mAh g^{-1} were obtained at high rates of 30 and 50 A g^{-1}, respectively. More impressively, the LNVO/Zn cell can reach a capacity 264 mAh g^{-1} at an ultra-high current density of 100 A g^{-1} in under 10 s. To elaborate, ~54% of the maximum capacity can be retained with a 200-fold current density increase from 0.5 A g^{-1} to 100 A g^{-1}, which is one of the best rate performances reported in the literature (**Figure 3-10e** and Error! Reference source not found.).[13–20] In the end, the system was cycled again at 0.5 A g^{-1} and negligible fading of capacity was observed, suggesting that the rate performance is sustainable and causes no irreversible damage to the cathode material. For BVO, its discharge capacity rapidly decreased to 15 mAh g^{-1} when the current density was increased to 50 A g^{-1}. Thus, the super-high-rate performance is dramatically improved due to pseudocapacitive response of the precisely designed LNVO cathode material.

The cycling stability and corresponding voltage profiles of the LNVO electrode at a current density of 30 A g^{-1} are shown in **Figure 3-10f**, which shows an impressive 92% capacity retention after 3000 cycles. Plateaus in the GCD profiles (**Figure S3-17b**) can be observed during long-term cycling, which indicates that reversible Faradaic reactions still occur even in the ultrafast charge/discharge storage process. The capacity of LNVO at 30 A g^{-1} is almost three times greater than that of micro-sized BVO powder with a much more stable Coulombic efficiency (CE) range. The LNVO film generally shows a dramatically superior electrochemical performance compared to its bulk counterpart due to its facile strain relaxation upon Zn cycling, shorter diffusion lengths, and faster storage mechanism. We further took apart the cell after 2000 cycles at 30 A g^{-1} to investigate the electrode evolution during long-term cycling and **Figure S3-18** shows the optical image. No obvious color change for the separator after cycling is observed, indicating the common vanadium dissolution issue might be suppressed by the rigidity of the LNVO nanostructure. As displayed in SEM images (**Figure S3-19**), the morphology of the LNVO film with nano-VO_x particles anchored on a rGO scaffold only slightly changes and no serious Zn dendrites can be seen in the SEM images, favoring the long-term cycling stability at fast rates. More impressively, the LNVO electrode has a capacity retention of >85% after 1,500 cycles at a high current density of 50 A g^{-1}, and the CE was maintained at nearly 100% throughout cycling (**Figure S3-17b**).

Storage mechanism

To elucidate the pseudocapacitive charge-storage mechanism based on redox reactions confined on/near the LNVO film surface, the evolution of LNVO electrodes at different charge/discharge states were first characterized by XPS measurements. Error! Reference source not found.**b** gives a clear trend that the Zn:V at.% ratio decreased as the battery was charged to 1.6 V and then increased

when the cell was discharged to 0.3 V, demonstrating reversible Zn de-intercalation/intercalation upon charge/discharge. As shown in the O 1s region (**Figure S3-20**), there is a significantly taller high-energy shoulder when the cell was fully discharged at 0.3 V. This can be assigned to the increasing presence of H-O-H,[21–24] which is absent in the pristine cathode (**Figure S3-13a**). The at.% ratio of H-O-H to V-O-V follows the same trend during cycling, suggesting that Zn^{2+} insertion is accompanied by H_3O^+ (Error! Reference source not found.**c**). Based on the Zn/V ratio from the XPS survey spectrum, 0.70 Zn^{2+} per V is reversibly cycled between 0.3 V and 1.6 V. For each $V_2O_{4.68}$ unit, the amount of inserted Zn^{2+} and H^+ can be quantified to be 1.40 and 0.84 when considering the high capacity of 553 mAh g^{-1} at 0.1 A g^{-1} corresponding to a ~3.64 electron redox process (**Figure S3-21**). Therefore, the insertion of Zn^{2+} and H^+ contributes to 77% (about 426 mAh g^{-1}) and 23% (about 127 mAh g^{-1}) capacity, respectively, and the step-by-step electrochemical reactions based on different redox peaks in CV curve (**Figure 3-10a**) can be expressed as following:

Step 1 (0.3-0.9 V): $V_2O_{4.68} + 0.68\ Zn^{2+} + 0.49\ H^+ + 1.85\ e^- \leftrightarrow H_{0.49}Zn_{0.68}V_2O_{4.68}$

Step 2 (0.9 V-1.6 V): $H_{0.49}Zn_{0.68}V_2O_{4.68} + 0.72\ Zn^{2+} + 0.35\ H^+ + 1.79\ e^- \leftrightarrow H_{0.84}Zn_{1.40}V_2O_{4.68}$

Overall: $V_2O_{4.68} + 1.40\ Zn^{2+} + 0.84\ H^+ + 3.64\ e^- \leftrightarrow H_{0.84}Zn_{1.40}V_2O_{4.68}$

Raman spectroscopy (Error! Reference source not found.**d**) was carried out to further investigate the changes in the cathodes. As shown in **Figure S3-22**, the low-frequency peaks at 283, 404, 480, 521, 688, 998 cm^{-1} can be assigned to the ladder distortion, V-$O_{bridging}$-V bending, ladder step stretching, V-O3$O_{bridging}$-V symmetric stretching and apical V=O stretching in V_2O_5, respectively.[25] The D and G bands of graphene are also observed at 1338 and 1598 cm^{-1}. Upon charging and discharging, the main parts of the spectra remain unchanged except for the region between 820 and 1000 cm^{-1}. As the cell is charged from 0.3 V to 1.6 V, the intensity of the 998 cm^{-}

[1] peak (assigned to apical V=O stretching) increased with Zn^{2+} extraction, while the broad peaks in the 820-950 cm^{-1} region gradually decreased and finally disappeared at the top of the charge. The spectrum of the fully charged cell is almost identical to that of the pristine cathode. This suggests that the V=O bond in the pristine V_2O_5 is disrupted by the O coordination to inserted Zn^{2+} and/or V coordination to the co-inserted H_3O^+ during discharge. We speculate that the new peaks arise from stretching modes of the apical V-O bonds that resulted from the V-O-Zn with Zn^{2+} and/or V-O-H coordination with co-inserted H_3O^+.[26] Subsequently with the potential decreasing to 0.3 V, the broad peaks are recovered upon Zn^{2+} insertion, which clearly demonstrates the good Zn^{2+} storage reversibility.

The co-insertion mechanism was further validated by TEM of the LNVO cathode. The TEM image in Error! Reference source not found.**e** shows the nano-VO_x particles are still tightly anchored onto the rGO sheets, maintaining good hierarchical nanostructure after fully being charged/discharged. Because the lattice contraction induced by zinc intercalation and the expansion caused by the hydronium intercalation cancel each other out, the constant lattice spacing of 0.45 nm in the HRTEM image (Error! Reference source not found.**f**) can be understood,[13,27] which favors long-term cycling stability at faster rates. Meanwhile, the homogeneous distribution of elemental Zn in the EDS mappings further demonstrates uniform Zn^{2+} insertion (Error! Reference source not found.**g**). We also investigated the electrochemical behavior of the LNVO cathode in organic Zn^{2+}-based electrolyte to elucidate this Zn^{2+}/H_3O^+ co-insertion mechanism. As shown in **Figure S3-23a**, when 0.1 M $Zn(OTf)_2$ in anhydrous acetonitrile was used as the electrolyte, the specific capacity was negligible and there is no significant H-O-H component in the XPS O 1s region of the cathode

(**Figure S3-23b**). However, the capacity increased dramatically to 402 mAh g^{-1} with the addition of 10 wt.% H_2O, indicating that H_2O is essential to Zn^{2+} insertion.

Practical applications

For practical applications, there are many parameters that need to be considered, such as gravimetric energy/power density, mass loading, temperature tolerance, mechanical robustness, and fast-charging properties. The LNVO/Zn system is able to achieve these requirements simultaneously without sacrificing any of them. The high energy and high power densities are confirmed by the Ragone plot (**Figure 3-12a**), showing an energy density of 396 Wh kg^{-1} at a power density of 351 W kg^{-1} and 164 Wh kg^{-1} at 56306 W kg^{-1}, which surpasses most of the previously reported Zn-ion devices.[28–32] At a mass loading of 4.5 mg cm^{-2}, a high energy density of 215 Wh kg^{-1} is still maintained with a commercially favorable areal capacity that is close to 2 mAh cm^{-2} (**Figure 3-12b**). **Figure 3-12c** shows the galvanostatic voltage profiles at different temperatures. A high specific capacity of ~400 mAh g^{-1} with minimal polarization and good reaction kinetics were obtained at both 4 °C and 65 °C, which is comparable to that tested at 25 °C, suggesting the good compatibility over a wide range of temperatures. As shown in **Figure 3-12d**, the LNVO/Zn system was cycled in a $ZnCl_2$/LiCl/PVA gel electrolyte to demonstrate its practicability as a flexible device. The fabricated quasi-solid-state pouch cell was cycled under flat, bent, and twisted conditions. The relatively stable specific capacity when mechanically bent or twisted indicate the excellent mechanical stability of the cell, revealing superior comprehensive performance of the as-prepared LNVO film.

Conclusions

In summary, we have designed a nano-VO_x (LNVO) film with good pseudocapacitive response for zinc ion storage synthesized via a scalable laser-scribing method. The hierarchical nanostructure provides abundant charge storage active sites, facilitating high specific capacity and fast electrochemical kinetics. In this way, the LNVO/Zn system exhibits a Faradaic nature with predominantly capacitive kinetics, as the redox processes are confined to the surface (90-98% contribution), thus achieving high energy density and power density simultaneously, which fills an important gap in the energy-storage field. Specifically, a record rate performance, 264 mAh g^{-1} for <10 s-fast charging/discharging at 100 A g^{-1}, has been obtained. The energy and power density can reach 396 Wh kg^{-1} (at 351 W kg^{-1}) and 56306 W kg^{-1} (at 164 Wh kg^{-1}), respectively. Oustanding cycling performance at ultrafast rates, 434 mAh g^{-1} with a capacity retention of >90% over 3,000 cycles at 30 A g^{-1} and 329 mAh g^{-1} with >85% over 1,500 cycles at 50 A g^{-1}, has been demonstrated and can be attributed to the structural stability of LNVO upon cycling. The charge storage mechanism of the LNVO/Zn system was found to be a hydronium ion-faciliated co-insertion of zinc ions. The scalable areal mass loading, temperature tolerance and great electrochemical performance when constructed in a flexible device show that the LNVO film is readily applicable in practical settings. Overall, the LNVO/Zn system provides a promising solution towards grid-scale energy storage owing to its high capacity, fast kinetics and long cycle life.

Methodts

Synthesis of LNVO

Graphite oxide (GO) was synthesized via a modified Hummer's method.[33] In a typical synthesis, 160 mg of freeze-dried GO powder was diluted with the addition of 7.6 mL DI water and dispersed by 2-minute tip sonication. 40 mg of VCl_3 (Fisher Scientific) was dissolved in 8.4 mL DI water and bath sonicated for 2 hours. Next, the VCl_3 solution was uniformly added to the GO suspension within 1 hour via a syringe pump while stirring. The resulting mixture was then drop-cast onto graphite paper (Panasonic) at a density of 200 μL cm^{-2} and left to dry under ambient conditions. Then, the dried film was laser-scribed using a 40 W Full Spectrum Laser Muse 2D Vision Desktop CO_2 Laser Cutter with a 12% power setting, and electrodes were cut out of the film using a 10 mm hole punch. Finally, the electrodes were placed in a furnace which was set to 60 °C for 1 h, ramped up to 300 °C at 2 °C min^{-1} and then left at 300 °C for 1 h. The as-made *LNVO* electrodes were weighed by a micro-balance and the active material loading was determined to be 0.9 mg cm^{-2} by TGA. The films with higher mass loadings of 1.8, 2.7, and 4.5 mg cm^{-2} were synthesized using analogous methods with different amounts of GO and VCl_3 powder.

Fabrication of BVO cathodes

To fabricate the BVO cathodes, the V_2O_5 (Fisher Scientific, >99.6%), conductive carbon (Canrd, ≥99.5%), and polyvinylidene fluoride (PVDF, Canrd, ≥99.5%) binder with a mass ratio of 7:2:1 were dispersed in N-methyl-2-pyrrolidone (NMP, ≥99.9%) and cast onto stainless steel foil (10 μm thick, Canrd, 99.99%) using a conventional slurry and doctor-blading technique. The slurry with a mass loading of ~0.9 mg cm^{-2} was then dried overnight at 90 °C in a vacuum oven. The as-prepared electrodes were punched into 10 mm disks.

Fabrication of quasi-solid-state pouch cells

The $ZnCl_2$/LiCl/PVA gel electrolyte was made following a previously reported method.[34] The LNVO film was cut so that a 2×3.5 cm^2 area was exposed. The gel electrolyte was added to wet each of the electrodes and the separator and left for 30 minutes. After the excess electrolyte was removed, the separator was sandwiched between the two electrodes, and the assembled device was dried at 40 °C overnight. Subsequently, the current collectors were extended using 3M copper tape and the device was assembled using Kapton tape.

Electrochemical testing

All electrochemical data were collected on BioLogic VMP3 and LANDt battery cycler at 25 °C under ambient conditions unless specified otherwise. The 2032-type coin cells were assembled using glass fiber (Cytiva, Grade GF/C) as the separator, 2.0 M zinc sulfate ($ZnSO_4$, Sigma-Aldrich, 99%) as the electrolyte, and Zn foil (1.2 cm in diameter, 70 μm thick, Leishent, 99%) as the anode. For standardization, the amount of electrolyte for each cell was controlled to be 100 μL. Galvanostatic charge/discharge (GCD) and cyclic voltammetry (CV) tests were performed between 0.3-1.6 V. Electrochemical performance value calculations were based on discharge capacities.

Material characterization

Zn|LNVO full cells were disassembled at different charge/discharge states after cycling. Zn foil and LNVO films were harvested for scanning electron microscopy (SEM), transmission electron microscopy (TEM), X-ray photoelectron spectroscopy (XPS), and Raman characterizations. All samples for material characterization were gently and thoroughly rinsed with DI water to remove

trace residual salt. The SEM images were collected using a JEOL JSM-67 Field Emission Scanning Electron Microscope. TEM was performed on an FEI Titan 80-300 scanning transmission electron microscope (S/TEM) operated at 300 kV acceleration voltage. X-ray powder diffraction (XRD) was performed using a Panalytical X'Pert Pro X-ray powder diffractometer with Cu Kα radiation with a wavelength of 0.154 nm on a SiO_2 crystal zero-background plate. In order to eliminate the coinciding signals from graphite paper, glass slides were used as the substrate instead and the active materials were scratched off to maximize the signals. The unassigned small peaks in the spectra are from SiO_2 impurities. The XPS spectra were acquired using a Kratos Axis Ultra DLD spectrometer equipped with a monochromatic Al Kα X-ray source. Fittings of the XPS spectra were performed with CasaXPS software (Casa Software Ltd., version 2.3.15) to estimate the chemical species. High-resolution O 1s spectra were calibrated using the C 1s peak at 284.8 eV and fitted using a Shierly-type function background. The peak positions and areas were optimized by a Gaussian/Lorentzian product peak shape function, following the literature. The mass of the electrode was measured by a Mettler Toledo MX5 microbalance with 0.001 mg sensitivity. Raman spectroscopy was carried out using a Reinshaw inVia confocal Raman microscope with a 633 nm laser. Thermogravimetry analysis (TGA) was performed on a Perkin Elmer Diamond Thermogravimetric analyzer from ambient temperature to 800 °C at a linear heating rate of 10 °C min^{-1} under air atmosphere.

Acknowledgements

This work was finacially supported by the Noble Family Innovation Fund and UCLA-CNSI EICN Facilities.

References

(1) Schoenfisch, M.; Dasgupta, A. *Grid-Scale Storage*. IEA. https://doi.org/License: CC BY 4.0.

(2) Palacín, M. R.; de Guibert, A. Why Do Batteries Fail? *Science (1979)* **2016**, *351* (6273). https://doi.org/10.1126/science.1253292.

(3) Choi, N.-S.; Chen, Z.; Freunberger, S. A.; Ji, X.; Sun, Y.-K.; Amine, K.; Yushin, G.; Nazar, L. F.; Cho, J.; Bruce, P. G. Challenges Facing Lithium Batteries and Electrical Double-Layer Capacitors. *Angewandte Chemie International Edition* **2012**, *51* (40), 9994–10024. https://doi.org/10.1002/anie.201201429.

(4) Choi, N. S.; Chen, Z.; Freunberger, S. A.; Ji, X.; Sun, Y. K.; Amine, K.; Yushin, G.; Nazar, L. F.; Cho, J.; Bruce, P. G. Challenges Facing Lithium Batteries and Electrical Double-Layer Capacitors. *Angewandte Chemie - International Edition* **2012**, *51* (40), 9994–10024. https://doi.org/10.1002/anie.201201429.

(5) Yan, M.; Ni, H.; Pan, H. Rechargeable Mild Aqueous Zinc Batteries for Grid Storage. *Advanced Energy and Sustainability Research* **2020**, *1* (1), 2000026. https://doi.org/10.1002/aesr.202000026.

(6) Fang, G.; Zhou, J.; Pan, A.; Liang, S. Recent Advances in Aqueous Zinc-Ion Batteries. *ACS Energy Lett* **2018**, *3* (10), 2480–2501. https://doi.org/10.1021/acsenergylett.8b01426.

(7) Chen, D.; Lu, M.; Cai, D.; Yang, H.; Han, W. Recent Advances in Energy Storage Mechanism of Aqueous Zinc-Ion Batteries. *Journal of Energy Chemistry* **2021**, *54*, 712–726. https://doi.org/10.1016/j.jechem.2020.06.016.

(8) Simon, P.; Gogotsi, Y.; Dunn, B. Where Do Batteries End and Supercapacitors Begin? *Science*. American Association for the Advancement of Science March 14, 2014, pp 1210–1211. https://doi.org/10.1126/science.1249625.

(9) Augustyn, V.; Simon, P.; Dunn, B. Pseudocapacitive Oxide Materials for High-Rate Electrochemical Energy Storage. **2014**. https://doi.org/10.1039/c3ee44164d.

(10) Huang, A.; El-Kady, M. F.; Chang, X.; Anderson, M.; Lin, C.; Turner, C. L.; Kaner, R. B. Facile Fabrication of Multivalent VO x /Graphene Nanocomposite Electrodes for High-Energy-Density Symmetric Supercapacitors. *Adv Energy Mater* **2021**, *11* (26), 2100768. https://doi.org/10.1002/aenm.202100768.

(11) Augustyn, V.; Come, J.; Lowe, M. A.; Kim, J. W.; Taberna, P.-L.; Tolbert, S. H.; Abruña, H. D.; Simon, P.; Dunn, B. High-Rate Electrochemical Energy Storage through Li+ Intercalation Pseudocapacitance. *Nat Mater* **2013**, *12* (6), 518–522. https://doi.org/10.1038/nmat3601.

(12) Lindström, H.; Södergren, S.; Solbrand, A.; Rensmo, H.; Hjelm, J.; Hagfeldt, A.; Lindquist, S.-E. Li + Ion Insertion in TiO 2 (Anatase). 1. Chronoamperometry on CVD Films and Nanoporous Films. *J Phys Chem B* **1997**, *101* (39), 7710–7716. https://doi.org/10.1021/jp970489r.

(13) Wang, L.; Huang, K.-W.; Chen, J.; Zheng, J. Ultralong Cycle Stability of Aqueous Zinc-Ion Batteries with Zinc Vanadium Oxide Cathodes. *Sci Adv* **2019**, *5* (10), 1–11. https://doi.org/10.1126/sciadv.aax4279.

(14) Lv, T.; Zhu, G.; Dong, S.; Kong, Q.; Peng, Y.; Jiang, S.; Zhang, G.; Yang, Z.; Yang, S.; Dong, X.; Pang, H.; Zhang, Y. Co-Intercalation of Dual Charge Carriers in Metal-Ion-

Confining Layered Vanadium Oxide Nanobelts for Aqueous Zinc-Ion Batteries. *Angewandte Chemie International Edition* **2023**, *62* (5). https://doi.org/10.1002/anie.202216089.

(15) Ma, X.; Cao, X.; Yao, M.; Shan, L.; Shi, X.; Fang, G.; Pan, A.; Lu, B.; Zhou, J.; Liang, S. Organic–Inorganic Hybrid Cathode with Dual Energy-Storage Mechanism for Ultrahigh-Rate and Ultralong-Life Aqueous Zinc-Ion Batteries. *Advanced Materials* **2022**, *34* (6), 2105452. https://doi.org/10.1002/adma.202105452.

(16) Hu, L.; Wu, Z.; Lu, C.; Ye, F.; Liu, Q.; Sun, Z. Principles of Interlayer-Spacing Regulation of Layered Vanadium Phosphates for Superior Zinc-Ion Batteries. *Energy Environ Sci* **2021**, *14* (7), 4095–4106. https://doi.org/10.1039/D1EE01158H.

(17) Huang, J.; Liang, H.; Tang, Y.; Lu, B.; Zhou, J.; Liang, S. In Situ Induced Coordination between a “Desiccant” Interphase and Oxygen-Deficient Navajoite towards Highly Efficient Zinc Ion Storage. *Adv Energy Mater* **2022**, *12* (35), 2201434. https://doi.org/10.1002/aenm.202201434.

(18) Sun, Q.; Cheng, H.; Yuan, Y.; Liu, Y.; Nie, W.; Zhao, K.; Wang, K.; Yao, W.; Lu, X.; Lu, J. Uncovering the Fundamental Role of Interlayer Water in Charge Storage for Bilayered V 2 O 5 · n H 2 O Xerogel Cathode Materials. *Adv Energy Mater* **2023**, *13* (3), 2202515. https://doi.org/10.1002/aenm.202202515.

(19) Zhu, K.; Wei, S.; Shou, H.; Shen, F.; Chen, S.; Zhang, P.; Wang, C.; Cao, Y.; Guo, X.; Luo, M.; Zhang, H.; Ye, B.; Wu, X.; He, L.; Song, L. Defect Engineering on V2O3 Cathode for Long-Cycling Aqueous Zinc Metal Batteries. *Nat Commun* **2021**, *12* (1), 6878. https://doi.org/10.1038/s41467-021-27203-w.

(20) Zhang, Y.; Jiang, S.; Li, Y.; Ren, X.; Zhang, P.; Sun, L.; Yang, H. Y. In Situ Grown Hierarchical Electrospun Nanofiber Skeletons with Embedded Vanadium Nitride Nanograins for Ultra-Fast and Super-Long Cycle Life Aqueous Zn-Ion Batteries. *Adv Energy Mater* **2023**, *13* (5), 2202826. https://doi.org/10.1002/aenm.202202826.

(21) Zhao, Q.; Chen, X.; Wang, Z.; Yang, L.; Qin, R.; Yang, J.; Song, Y.; Ding, S.; Weng, M.; Huang, W.; Liu, J.; Zhao, W.; Qian, G.; Yang, K.; Cui, Y.; Chen, H.; Pan, F. Unravelling H + /Zn 2+ Synergistic Intercalation in a Novel Phase of Manganese Oxide for High-Performance Aqueous Rechargeable Battery. *Small* **2019**, *15* (47), 1904545. https://doi.org/10.1002/smll.201904545.

(22) Zhai, X. Z.; Qu, J.; Hao, S. M.; Jing, Y. Q.; Chang, W.; Wang, J.; Li, W.; Abdelkrim, Y.; Yuan, H.; Yu, Z. Z. Layered Birnessite Cathode with a Displacement/Intercalation Mechanism for High-Performance Aqueous Zinc-Ion Batteries. *Nanomicro Lett* **2020**, *12* (1), 1–15. https://doi.org/10.1007/s40820-020-0397-3.

(23) Pang, Q.; Sun, C.; Yu, Y.; Zhao, K.; Zhang, Z.; Voyles, P. M.; Chen, G.; Wei, Y.; Wang, X. H2V3O8 Nanowire/Graphene Electrodes for Aqueous Rechargeable Zinc Ion Batteries with High Rate Capability and Large Capacity. *Adv Energy Mater* **2018**, *8* (19), 1800144. https://doi.org/10.1002/aenm.201800144.

(24) Zhang, N.; Jia, M.; Dong, Y.; Wang, Y.; Xu, J.; Liu, Y.; Jiao, L.; Cheng, F. Hydrated Layered Vanadium Oxide as a Highly Reversible Cathode for Rechargeable Aqueous Zinc Batteries. *Adv Funct Mater* **2019**, *29* (10), 1807331. https://doi.org/10.1002/adfm.201807331.

(25) Smirnov, M. B.; Roginskii, E. M.; Smirnov, K. S.; Baddour-Hadjean, R.; Pereira-Ramos, J.-P. Unraveling the Structure–Raman Spectra Relationships in V 2 O 5 Polymorphs via a Comprehensive Experimental and DFT Study. *Inorg Chem* **2018**, *57* (15), 9190–9204. https://doi.org/10.1021/acs.inorgchem.8b01212.

(26) Lee, S.-H.; Cheong, H. M.; Je Seong, M.; Liu, P.; Tracy, C. E.; Mascarenhas, A.; Pitts, J. R.; Deb, S. K. Microstructure Study of Amorphous Vanadium Oxide Thin Films Using Raman Spectroscopy. *J Appl Phys* **2002**, *92* (4), 1893–1897. https://doi.org/10.1063/1.1495074.

(27) Kundu, D.; Adams, B. D.; Duffort, V.; Vajargah, S. H.; Nazar, L. F. A High-Capacity and Long-Life Aqueous Rechargeable Zinc Battery Using a Metal Oxide Intercalation Cathode. *Nat Energy* **2016**, *1* (10), 16119. https://doi.org/10.1038/nenergy.2016.119.

(28) Lee, J.; Ju, J. B.; Cho, W. Il; Cho, B. W.; Oh, S. H. Todorokite-Type MnO2 as a Zinc-Ion Intercalating Material. *Electrochim Acta* **2013**, *112*, 138–143. https://doi.org/10.1016/j.electacta.2013.08.136.

(29) Zhang, N.; Cheng, F.; Liu, J.; Wang, L.; Long, X.; Liu, X.; Li, F.; Chen, J. Rechargeable Aqueous Zinc-Manganese Dioxide Batteries with High Energy and Power Densities. *Nat Commun* **2017**, *8* (1), 405. https://doi.org/10.1038/s41467-017-00467-x.

(30) Zhang, N.; Cheng, F.; Liu, Y.; Zhao, Q.; Lei, K.; Chen, C.; Liu, X.; Chen, J. Cation-Deficient Spinel ZnMn 2 O 4 Cathode in Zn(CF 3 SO 3) 2 Electrolyte for Rechargeable Aqueous Zn-Ion Battery. *J Am Chem Soc* **2016**, *138* (39), 12894–12901. https://doi.org/10.1021/jacs.6b05958.

(31) Yan, M.; He, P.; Chen, Y.; Wang, S.; Wei, Q.; Zhao, K.; Xu, X.; An, Q.; Shuang, Y.; Shao, Y.; Mueller, K. T.; Mai, L.; Liu, J.; Yang, J. Water-Lubricated Intercalation in V 2 O 5 ·nH 2 O for High-Capacity and High-Rate Aqueous Rechargeable Zinc Batteries. *Advanced Materials* **2018**, *30* (1), 1703725. https://doi.org/10.1002/adma.201703725.

(32) Ding, J.; Du, Z.; Gu, L.; Li, B.; Wang, L.; Wang, S.; Gong, Y.; Yang, S. Ultrafast Zn2+ Intercalation and Deintercalation in Vanadium Dioxide. *Advanced Materials* **2018**, *30* (26), 2–7. https://doi.org/10.1002/adma.201800762.

(33) Hummers, W. S.; Offeman, R. E. Preparation of Graphitic Oxide. *J Am Chem Soc* **1958**, *80* (6), 1339–1339. https://doi.org/10.1021/ja01539a017.

(34) Zeng, Y.; Zhang, X.; Meng, Y.; Yu, M.; Yi, J.; Wu, Y.; Lu, X.; Tong X Zeng, Y. Y.; Zhang, X. Y.; Meng, Y.; Yu, M. H.; Lu, X. H.; Tong, Y. X.; Yi, J. N.; Wu, Y. Q. Achieving Ultrahigh Energy Density and Long Durability in a Flexible Rechargeable Quasi-Solid-State Zn–MnO2 Battery. *Advanced Materials* **2017**, *29* (26), 1700274. https://doi.org/10.1002/ADMA.201700274.

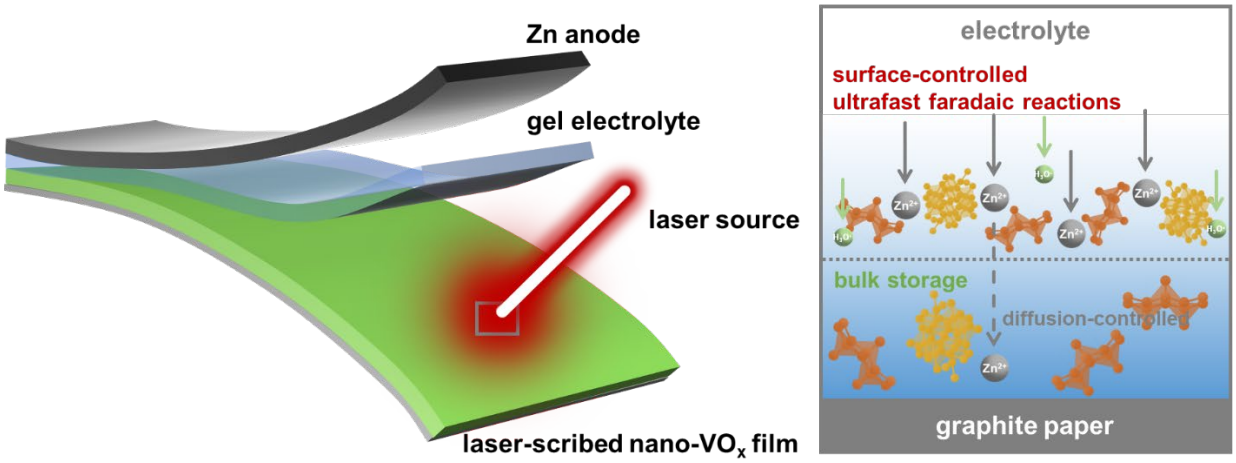

Figure 3-8. Schematic illustration showing the construction and the fast-charging behavior of the zinc-ion battery with a laser-scribed nano-VO_x cathode.

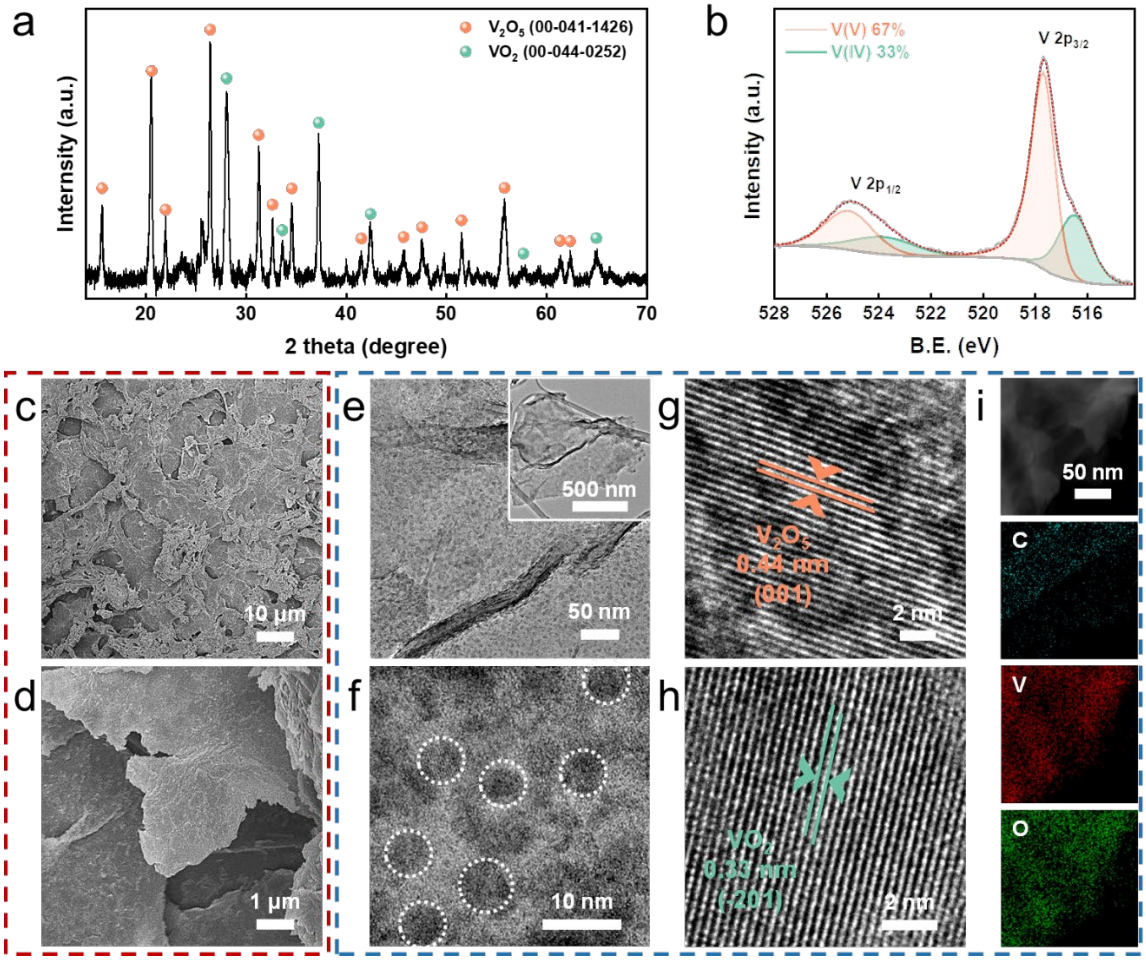

Figure 3-9. Characterization of the synthesized laser-scribed nano-VO_x cathode. (a) XRD pattern of LNVO. (b) XPS V 2p spectrum of LNVO. (c)-(d) SEM images of LNVO. (e)-(f) TEM images showing VO_x nanoparticles on an rGO sheet. (g)-(h) High-resolution TEM showing lattice spacings of V_2O_5 and VO_2. (i) TEM-EDS images displaying C, V, O distribution of LNVO.

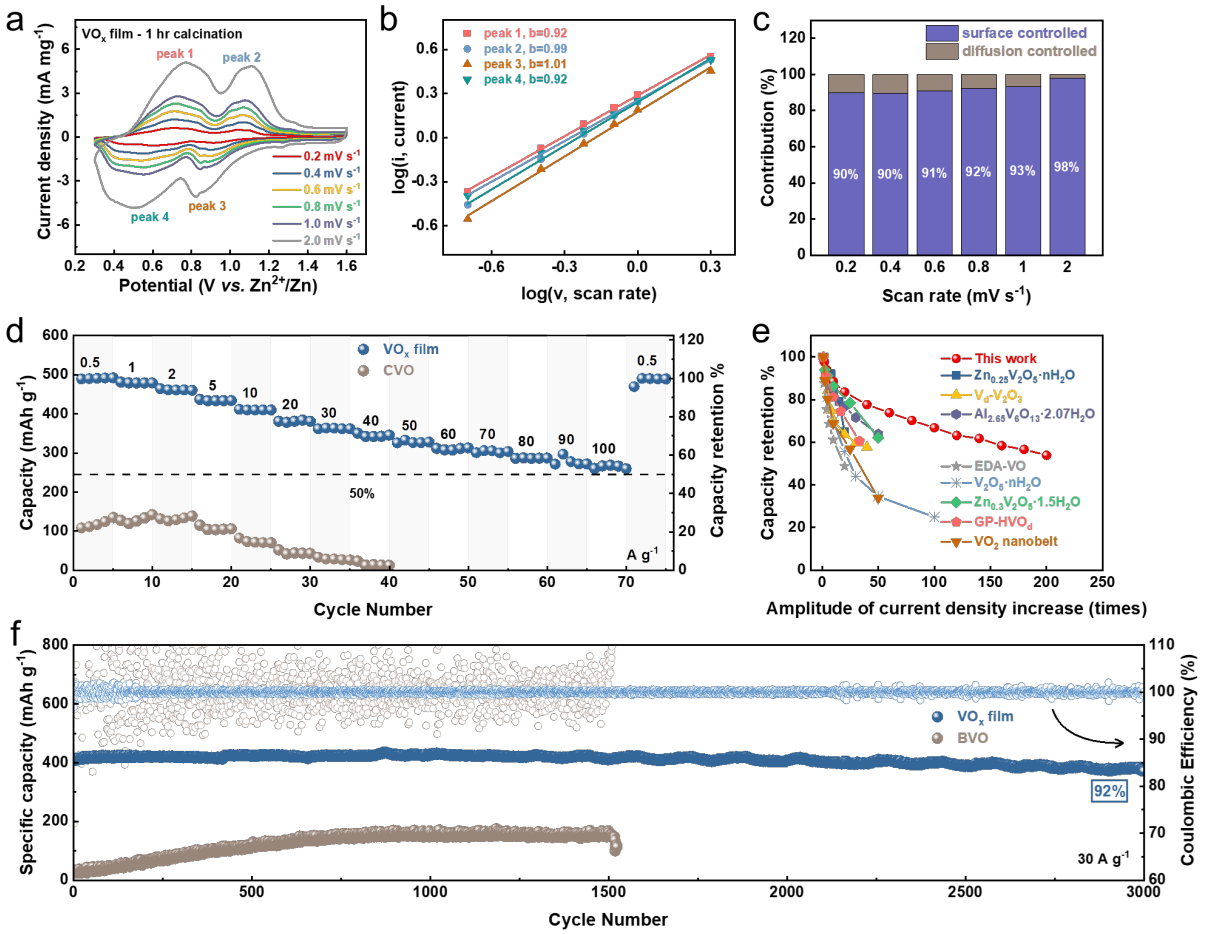

Figure 3-10. Electrochemical characterization of LNVO/Zn cells. (a) cyclic voltammogram (CV) of an LNVO/Zn cell at slow scan rates. (b) b-value fitting of peak currents from CV. (c) Quantified capacity contributions from surface-controlled and diffusion-controlled processes based on CV data. (d) Rate performance of LNVO/Zn showing the discharge capacity at 0.5 – 100 A g^{-1}. (e) Capacity retention % of the LNVO/Zn system change upon current density increase in comparison to previously reported systems. (f) The specific capacity of an LNVO/Zn cell during long-term cycling at 30 A g^{-1} compared to a cell with a bulk BVO cathode.

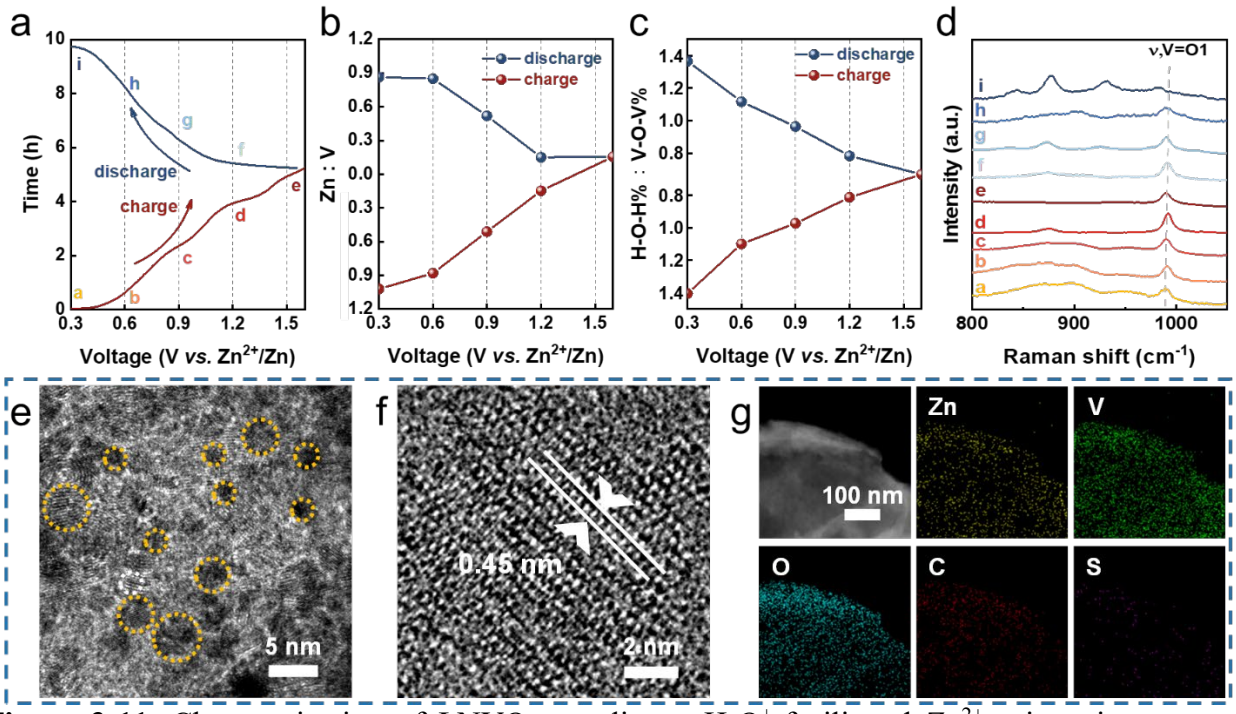

Figure 3-11. Characterization of LNVO revealing a H_3O^+-facilitated Zn^{2+}co-insertion mechanism. (a) The charge/discharge curve at 0.5 A g^{-1} labelled with stages a-i. (b) Zn:V atomic% ratios at various stages based on XPS survey spectra. (c) Atomic% ratios of the decoupled H-O-H to V-O-V peaks at various stages based on XPS O 1s region. (e-f) High-resolution TEM images showing the VO_x particles and lattice spacing of a fully discharged LNVO cathode. (g) TEM-EDS showing Zn, V, O, C and S distributions in the fully discharged LNVO cathode.

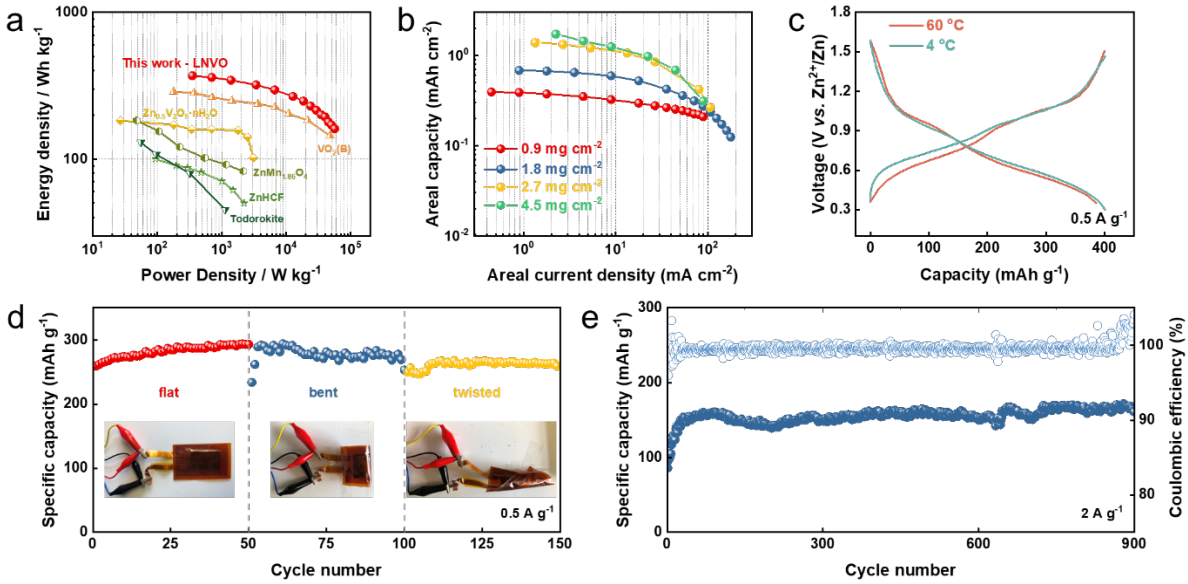

Figure 3-12. Demonstrated practical aspects of the LNVO/Zn system. (a) A Ragone plot comparing energy and power densities of the LNVO/Zn system to others in the literature. (b) Areal capacity of cells with different areal mass loading of LNVO cathode. (c) Voltages profiles of the LNVO/Zn system when cycled at 4 and 60 °C. Cycling performance of a flexible quasi-solid-state LNVO/Zn pouch cell showing (d) its mechanical flexibility and (e) long-term cycling stability at 2 A g^{-1}.

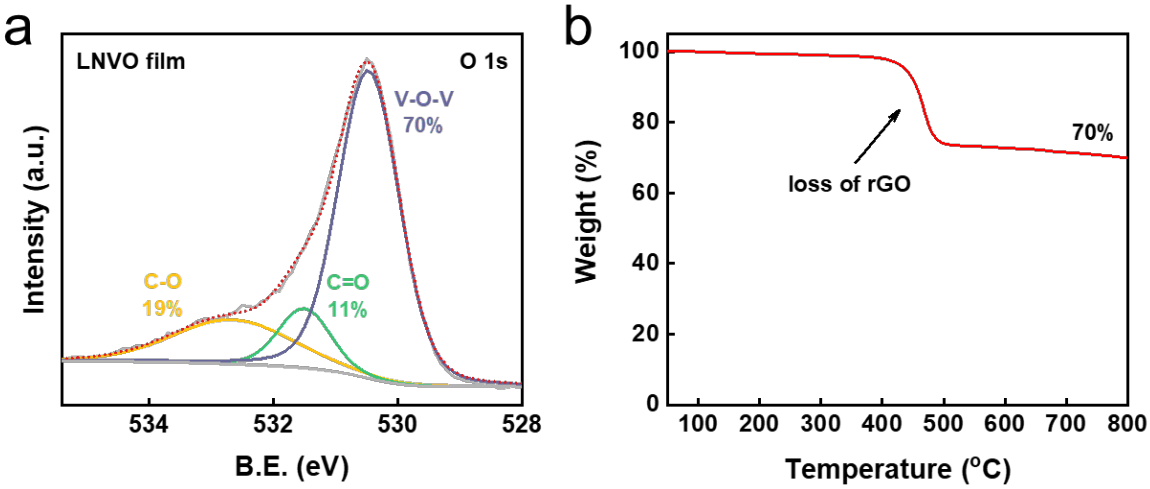

Figure S3-13. (a) XPS O 1s region and (b) TGA profile of the pristine LNVO.

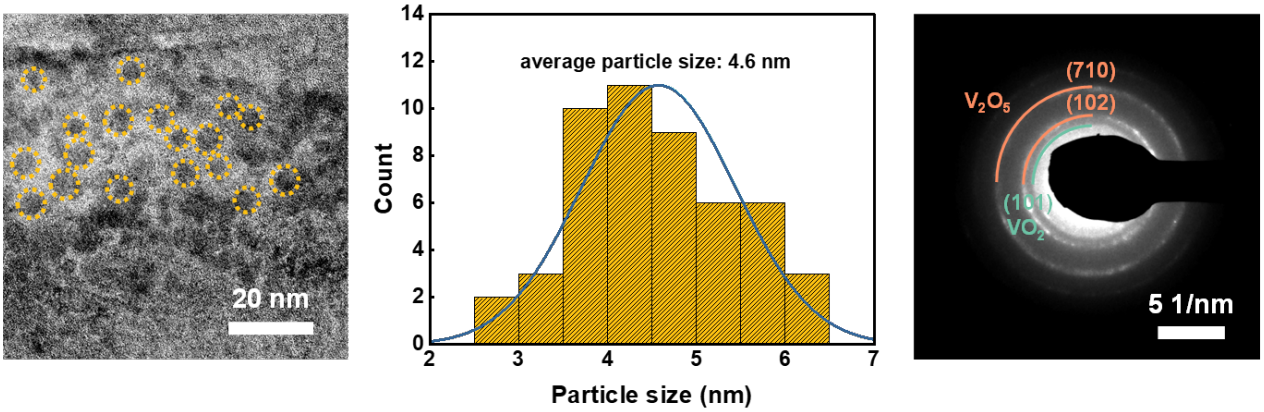

Figure S3-14. Particle size distribution and SAED pattern based on the TEM images of pristine LNVO.

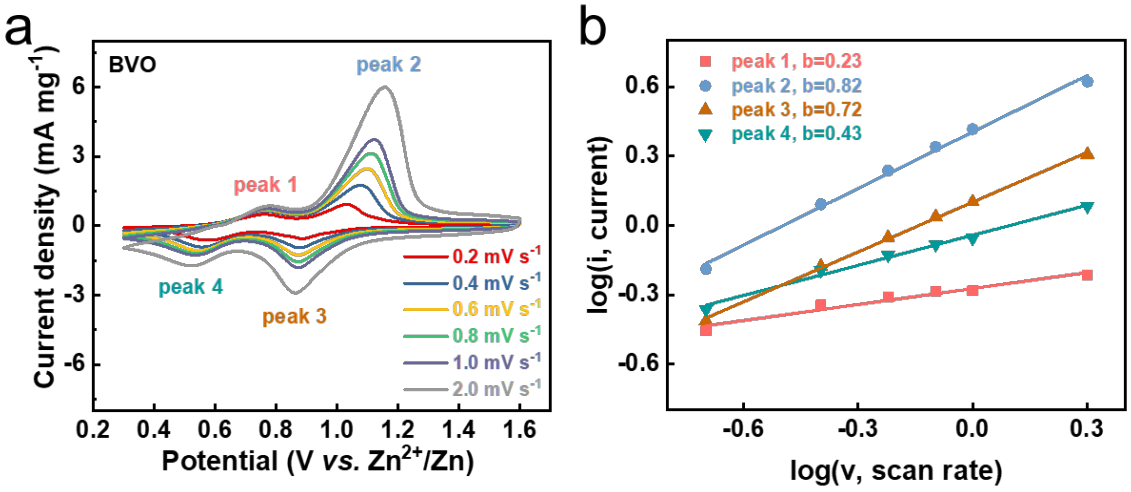

Figure S3-15. (a) CV and (b) b-value fitting of BVO|Zn cells.

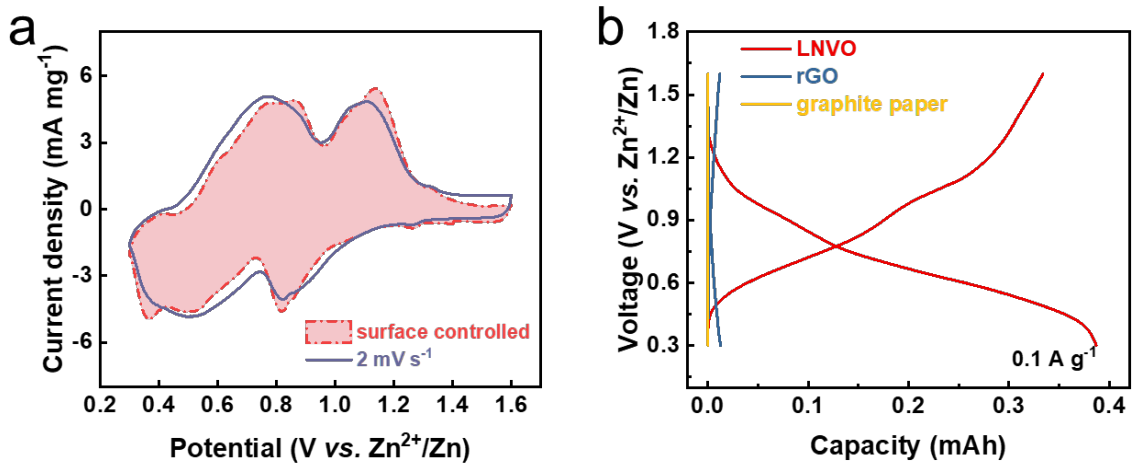

Figure S3-16. (a) CV of LNVO/Zn cell at 2 mV s^{-1} showing surface-controlled contributions. (b) Voltage-capacity profiles of cells with LNVO, rGO and graphite paper as cathode and zinc metal anode at 0.1 A g^{-1}.

Table S2. Rate Performance Data of LNVO/Zn and BVO/Zn Systems

	Rate performance (A g^{-1})														
Cathode	0.5	1	2	5	10	20	30	40	50	60	70	80	90	100	0.5
LNVO	491	480	462	434	410	381	363	345	328	310	303	287	278	264	486
BVO	119	130	132	107	74	45	29	15	---	---	---	---	---	---	---

Table S3. High-Rate Performance Data of Previously Reported ZIB and This Work

Active materials	Rate performance	Amplitude of current density increase	Capacity retention	Reference
$Zn_{0.25}V_2O_5 \cdot nH_2O$ nanobelts	183 mAh g^{-1} (3 A g^{-1})	20	65%	Nat. Energy, 2016, 1, 16119
vanadium defective-V_2O_3 (V_d-V_2O_3)	113 mAh g^{-1} (4 A g^{-1})	40	58%	Nat. Commun., 2021, 12, 6878
$Zn_{0.3}V_2O_5 \cdot 1.5H_2O$	265.2 mAh g^{-1} (10 A g^{-1})	50	62%	Sci. Adv. 2019, 5, eaax4279
phenylamine (PA)-intercalated $VOPO_4 \cdot 2H_2O$ (PA-VOP)	187.5 mAh g^{-1} (10 A g^{-1})	100	70%	Energy & Environ. Sci., 2021, 14, 4095-4106
$Al_{2.65}V_6O_{13} \cdot 2.07H_2O$	376.8 mAh g^{-1} (5 A g^{-1})	50	64%	Angew. Chem. Int. Ed. 2023, 62, e202216089
ethylenediamine–vanadium oxide (EDA-VO)	169.9 mAh g^{-1} (10 A g^{-1})	20	49%	Adv. Mater. 2022, 34, 2105452
vanadium nitride embedded nitrogen-doped carbon nanofiber (VN/N-CNFs)	297 mAh g^{-1} (100 A g^{-1})	200	42%	Adv. Energy Mater. 2023, 13, 2202826
$V_2O_5 \cdot nH_2O$ xerogels	112.2 mAh g^{-1} (10 A g^{-1})	100	25%	Adv. Energy Mater. 2023, 13, 2202515
$CaSO_4 \cdot 2H_2O$ coated $V_5O_{12-x} \cdot 6H_2O$ (GP-HVO_d)	225.5 mAh g^{-1} (10 A g^{-1})	33	61%	Adv. Energy Mater. 2022, 12, 2201434
VO_2 nanobelt	116.6 mAh g^{-1} (10 A g^{-1})	50	34%	Adv. Energy Mater. 2021, 11, 2003902
	363 mAh g^{-1} (30 A g^{-1})	**60**	**74%**	
This work	**328 mAh g^{-1} (50 A g^{-1})**	**100**	**67%**	
	264 mAh g^{-1} (100 A g^{-1})	**200**	**54%**	

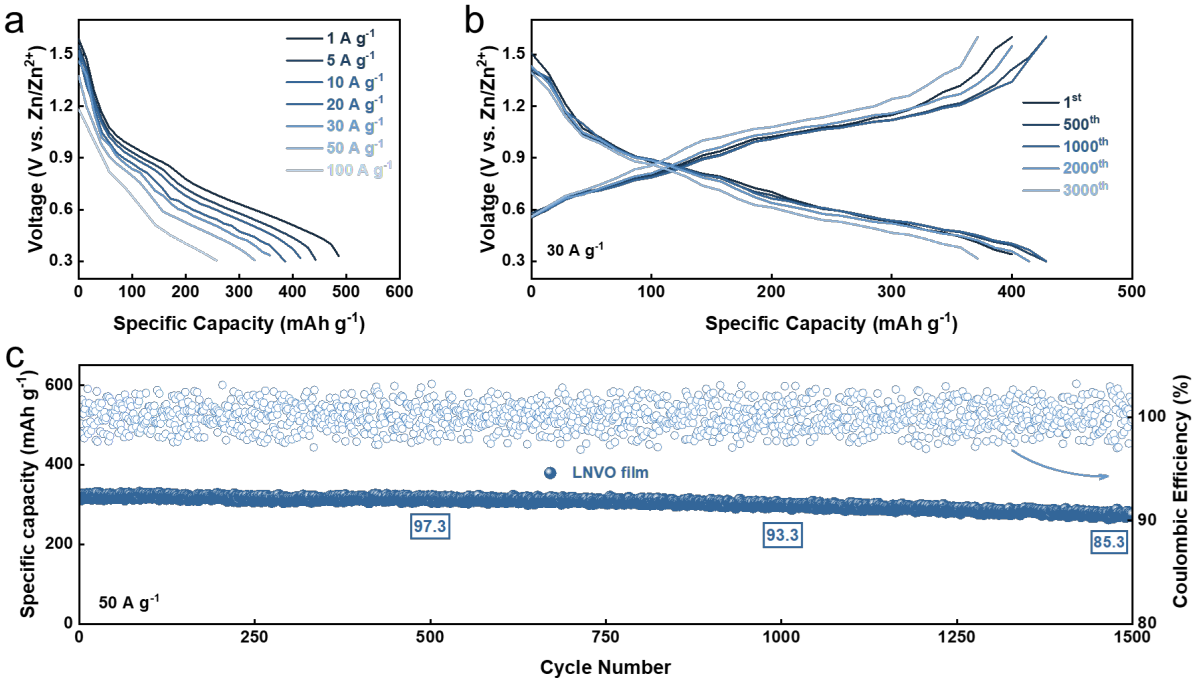

Figure S3-17. Voltage-capacity profiles of LNVO/Zn cells (a) at various current densities and (b) at the 1st , 500th, 1000th, 2000th, 3000th cycle during 30 A g^{-1} cycling. (c) Long-term cycling of a LNVO/Zn cell at 50 A g^{-1}.

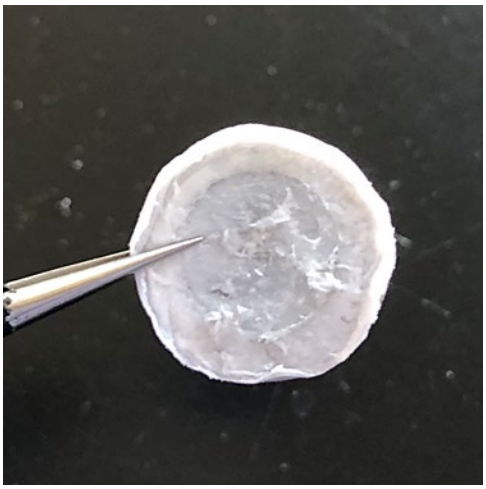

Figure S3-18. Optical image of the separator in a LNVO/Zn cell after cycling.

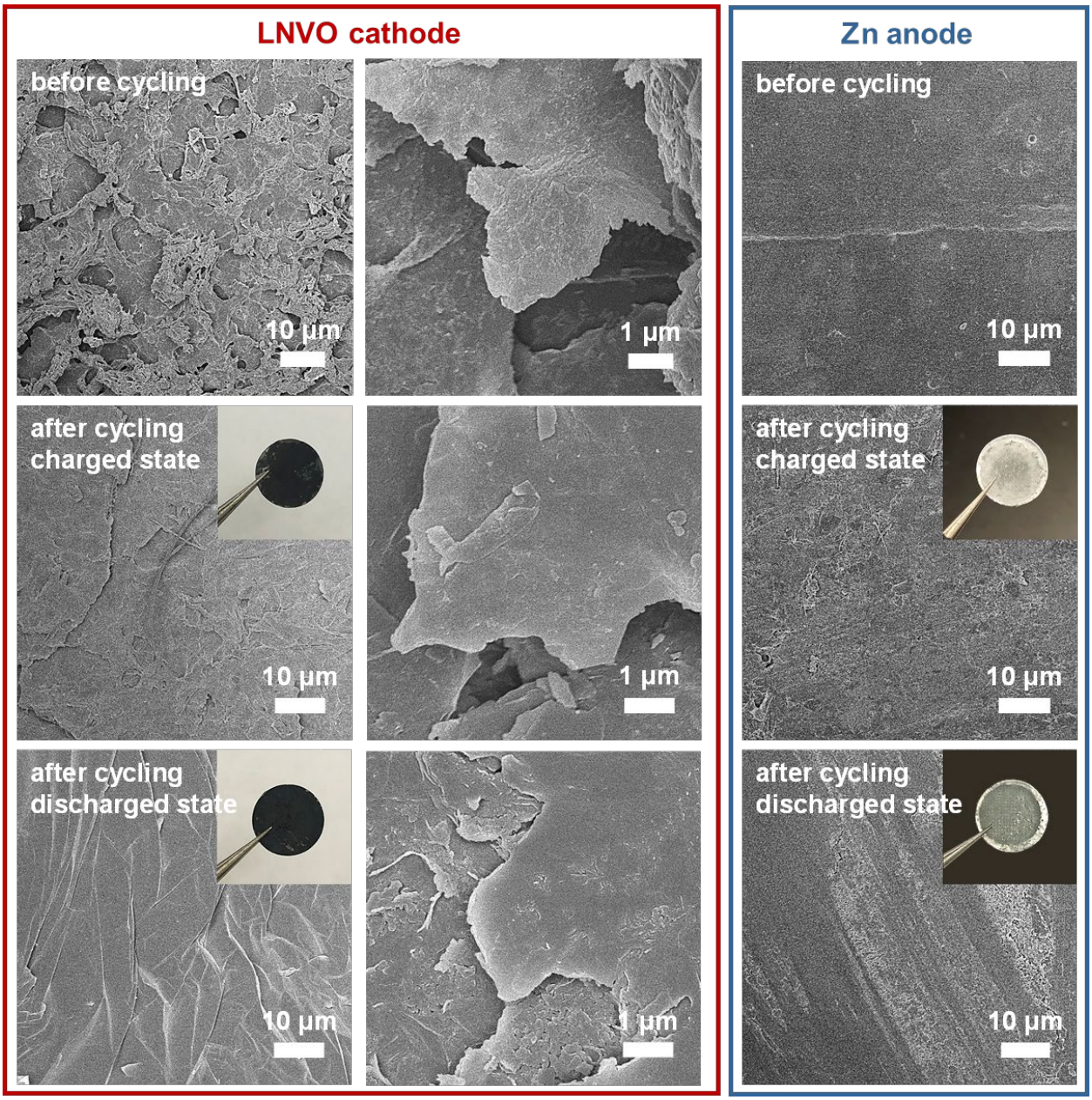

Figure S3-19. Optical and SEM images of the LNVO cathode and Zn anode after cycling.

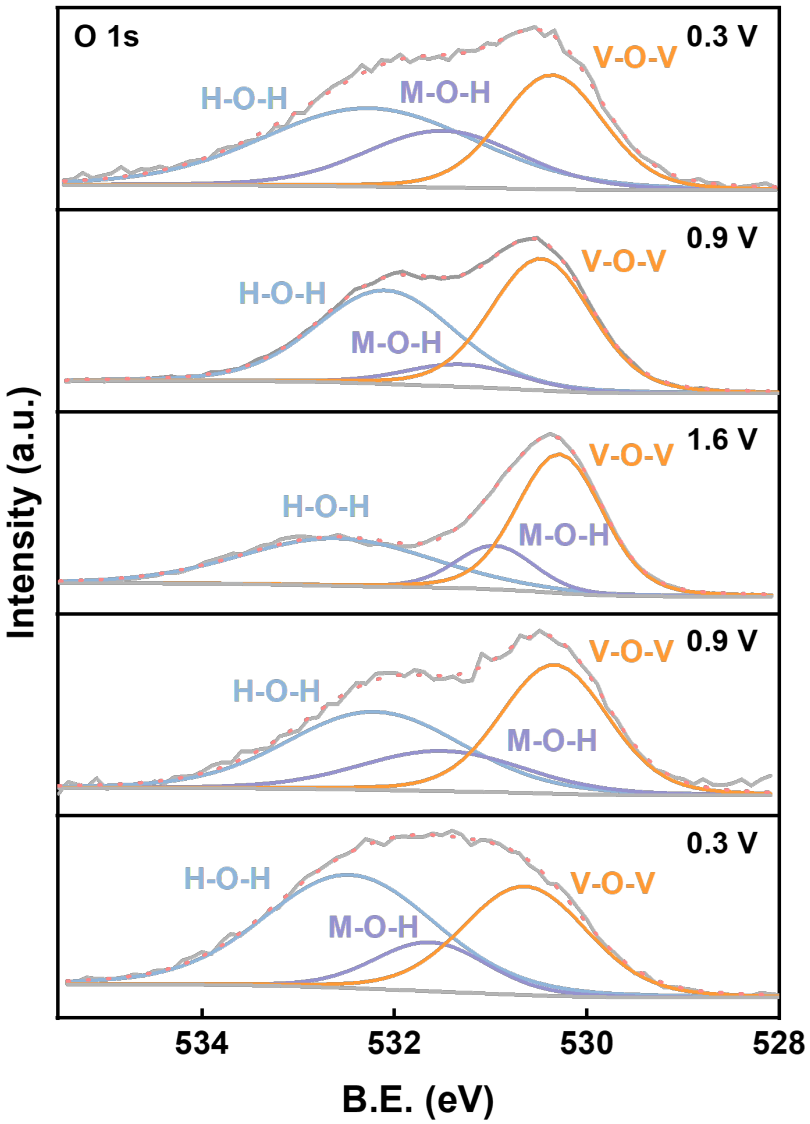

Figure S3-20. XPS O 1s region of the LNVO cathode at different voltages during the 1st charge/discharge cycle (0.5 A g^{-1}).

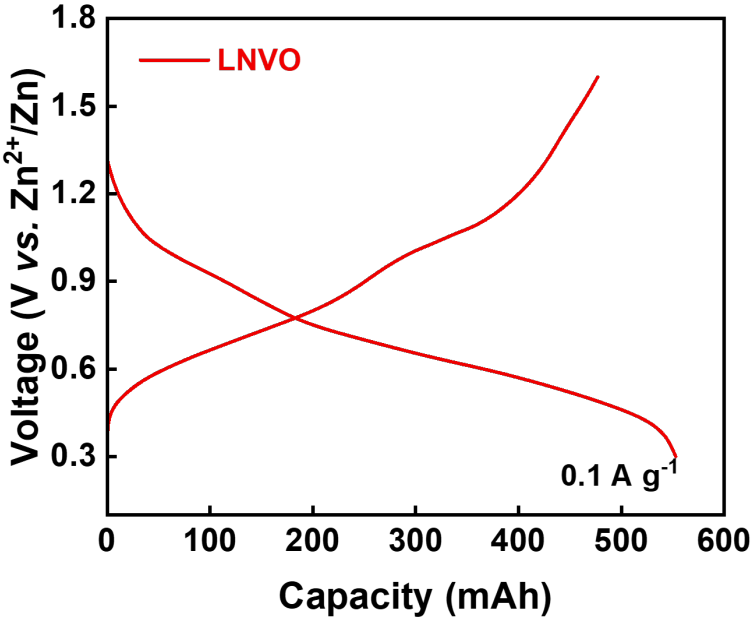

Figure S3-21. Capacity-voltage profile of the LNVO/Zn cell cycled at 0.1 A g^{-1}.

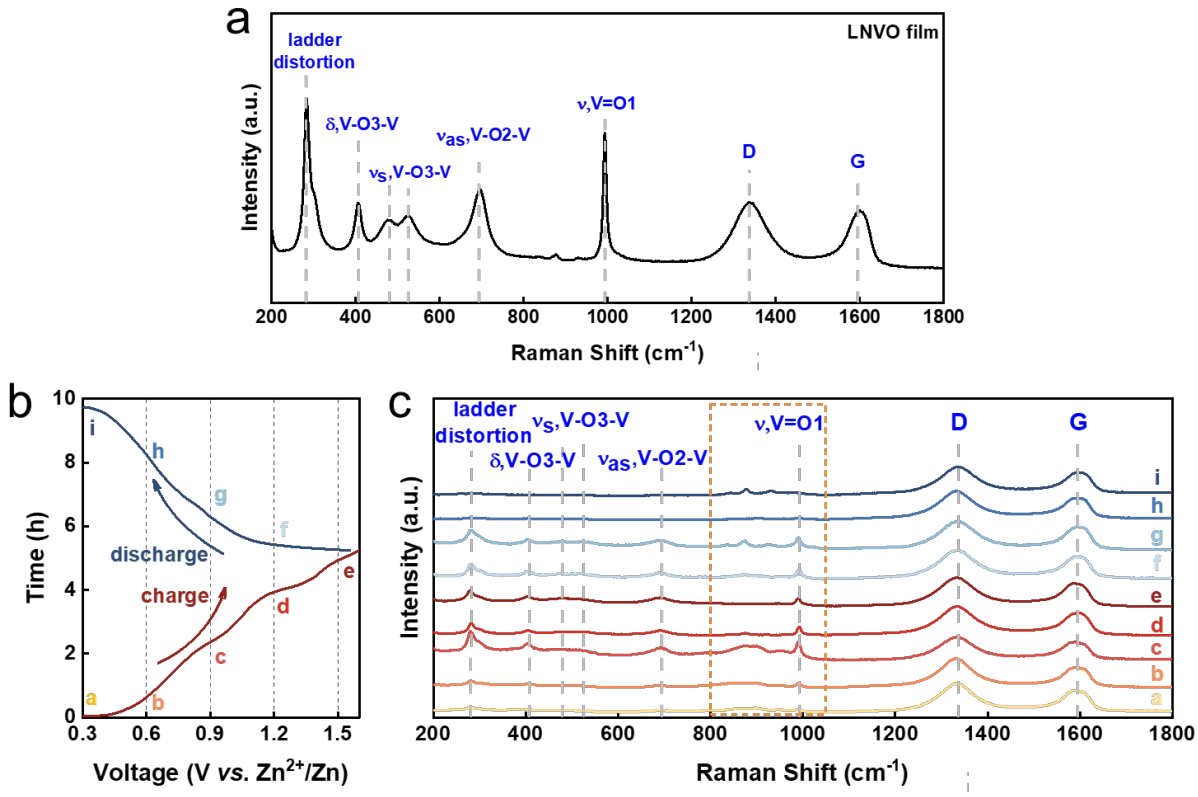

Figure S3-22. (a) The Raman spectrum of pristine LNVO. (b) The charge/discharge curve at 0.5 A g^{-1} labelled with stages a-i. (c) The Raman spectrum of LNVO cathode at various stages based on XPS survey spectra.

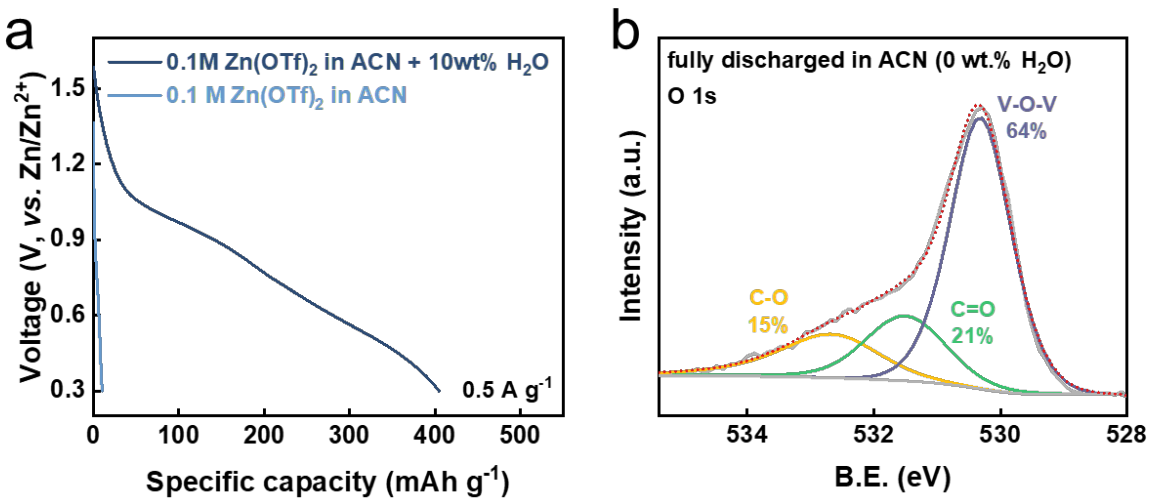

Figure S3-23. (a) Capacity-voltage profile of the LNVO/Zn cell cycled at 0.5 A g^{-1} in 0.1 M acetyl nitrile $Zn(OTf)_2$ electrolyte with 0 and 10 wt% H_2O.

Chapter 4. Nanoengineered Vanadium Oxide Composite as High-performance Anode for Aqueous Li-ion Hybrid Battery

Introduction

Aqueous rechargeable batteries have emerged as a promising technology for applications in large-scale energy storage systems due to their safe operation, non-toxicity, and cost-efficiency.[1] Among storage systems based on various cations such Na^+, K^+, Zn^{2+}, Mg^{2+}, Al^{3+}, etc., aqueous lithium-ion batteries (LIBs) are the most prominent candidates because of the well-developed manufacturing capability for LIB component production. The progress of aqueous LIB research has been significantly advanced by the development of numerous aqueous electrolytes, extending the electrochemical window beyond the conventional 1.23 V limit imposed by the electrolytic decomposition of water.[2–5] While the commercially available LIB cathodes including $LiCoO_2$, $LiFePO_4$, and $LiMn_2O_4$ conveniently sit below the upper potential limit of the operational window of aqueous electrolytes, carbon-based anodes that are widely used in organic electrolytes are not compatible with the aqueous system due to their low Li/Li^+ intercalation potential.[6–9] Thus, unconventional transition metal-based anodes must be employed in aqueous LIBs.

Restricted by the relatively high lower potential limit of aqueous lithium-ion electrolytes, the choice of suitable transition metal redox couples for an aqueous LIB anode is limited. Most reported aqueous LIBs use an intercalation-type Mo_6S_8 or TiO_2 anode. Although high average full-cell voltage can be achieved, the energy density is restricted by their low specific capacity, since a high capacity ratio between the negative electrode (anode) and positive electrode (cathode), known as the n:p ratio, is required to compensate for the initial loss of anode capacity by reactions with the electrolyte.[5] Therefore, there is an urgent need for anode materials that exhibit high

specific capacity. Vanadium oxide anodes have been reported to show enhanced capacity in aqueous LIBs; however, the added capacity is not sufficient to account for the lower average voltage owing to its unfavorable redox potential, leading to disadvantageous energy density.[10–13] *Moreover, aqueous LIBs have great potential for fast charging applications due to the enhanced diffusion in an aqueous electrolyte, which can be further improved by integrating electrodes with multi-dimensional diffusion pathways or with redox reactions confined to the surface. The spinel* $LiMn_2O_4$ *cathode allows three-dimensional Li migration, and* V_2O_5*, as an intrinsically intercalation-type material, can show extrinsic pseudocapacitive behavior when nanosized.*[14–17] *Therefore, the combination of these three components is expected to deliver a hybrid battery with excellent fast charging capability.*

In this work, we report a novel V_2O_5*/laser-scribed graphene (LSG) composite material in which* V_2O_5 *nanoparticles are uniformly anchored on a conductive graphene nanosheet scaffold. The* V_2O_5*-LSG composite is made from* VCl_3*/graphite oxide via an originally designed two-step laser scribing/photothermal approach where the former gives an expanded LSG network as well as nanosized vanadium particles and the latter further converts all vanadium species to* V_2O_5 *nanoparticles. In this way, the resulting* V_2O_5 *nanoparticles in the* V_2O_5*-LSG electrode are electrochemically active, small in grain size and easily accessible for charge transport via the LSG structure. This* V_2O_5*-LSG electrode shows pseudocapacitive features and remarkable rate capability in three-electrode measurements. When the* V_2O_5*-LSG anode is paired with a* $LiMn_2O_4$ *cathode, the hybrid battery exhibits predominantly surface-controlled charge storage behavior, leading to excellent fast charging capability. The full-cell specific capacity can reach 151 mAh (g anode)*$^{-1}$ *giving high power and energy density, 650 W kg*$^{-1}$ *(at 15.6 Wh kg*$^{-1}$*) and 81.5 Wh kg*$^{-1}$ *at (13.6 W kg*$^{-1}$*), that outperform the majority of previously reported aqueous LIBs.*

Results and discussions

The synthesis of V_2O_5-laser scribed graphene (LSG) was designed to adapt a pseudocapacitive material to battery chemistry. As shown in **Figure 13**, the VCl_3 solution was added to a graphite oxide (GO) dispersion to ensure uniform mixing of vanadium ions and GO sheets. The vanadium cations are believed to act as spacers to avoid aggregation of GO layers. As reported in our prior work, laser-scribing of a drop-cast VCl_3/GO film can simultaneously lead to the formation of low-valent vanadium oxides (VO_x, predominantly V_2O_3 and VO_2) and an expanded reduced graphene oxide (rGO) network due to the rapid release of gases, denoted here as VO_x-LSG.[18,19] Although laser-scribing alone can fabricate thin-film electrodes for supercapacitor systems that only rely on surface charge storage processes, the electrodes usually suffer from low areal mass loading[20,21] and incompatibility with battery-type electrochemistry, which require more uniformly formed electrodes to carry out ion transport deeper beneath the surface. Therefore, after the transient heat exposure induced by a CO_2 laser, the VO_x-LSG was exposed to a much longer (> 0.5 h) thermal treatment in air resulting in the oxidation of lower-valent VO_x to V_2O_5. By choosing a sufficiently low temperature, thermal decomposition of graphene to CO is prevented and the integrity of the LSG structure is preserved. In the end, the transformation from any unconverted VCl_3/GO and VO_x-LSG intermediate into a V_2O_5-LSG composite was completed.

The structural features of the as-synthesized V_2O_5-LSG composite were investigated by electron microscopy (SEM) and transmission electron microscopy (TEM). In

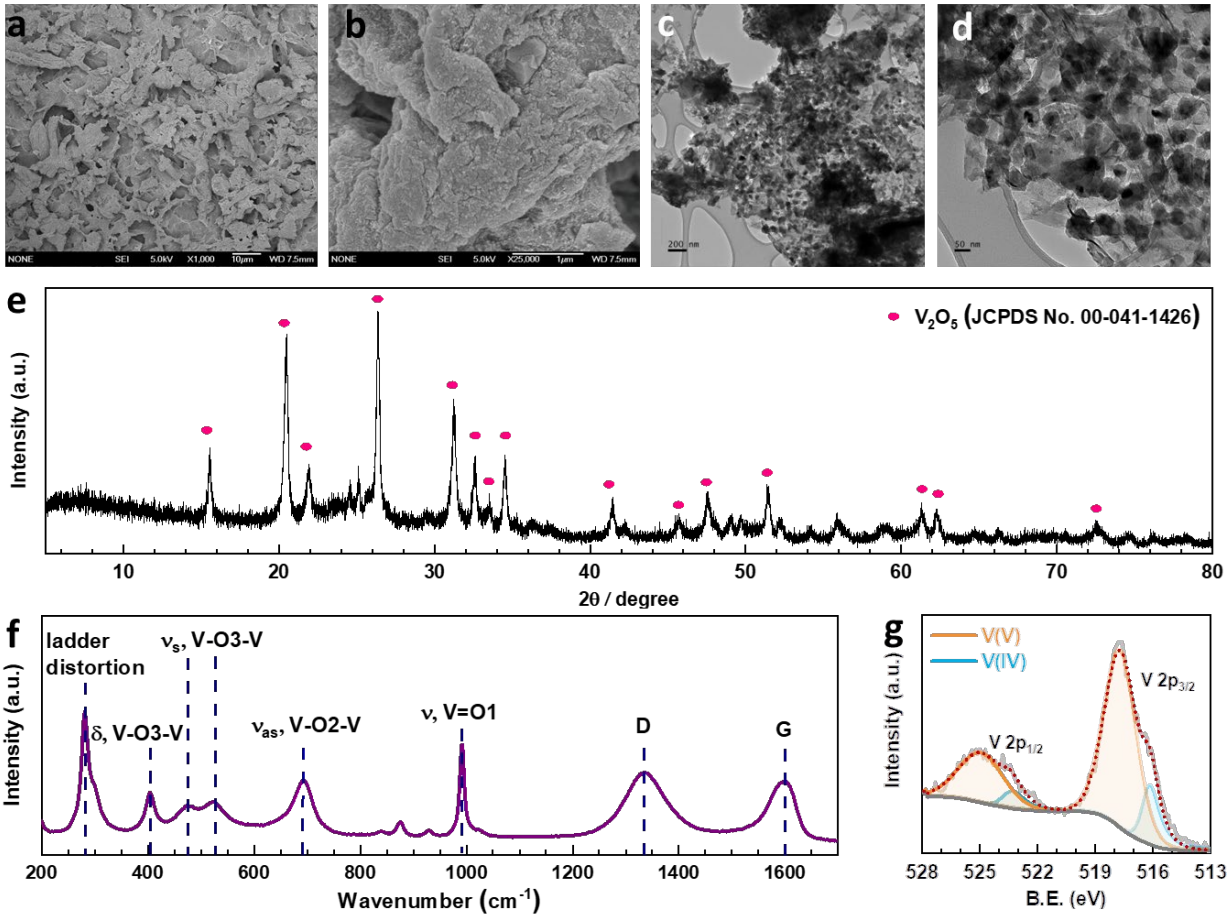

Figure 14a, randomly stacked rGO flakes with visible wrinkles are observed in the SEM image, suggesting the successful formation of the conductive LSG network. Under high

magnification,

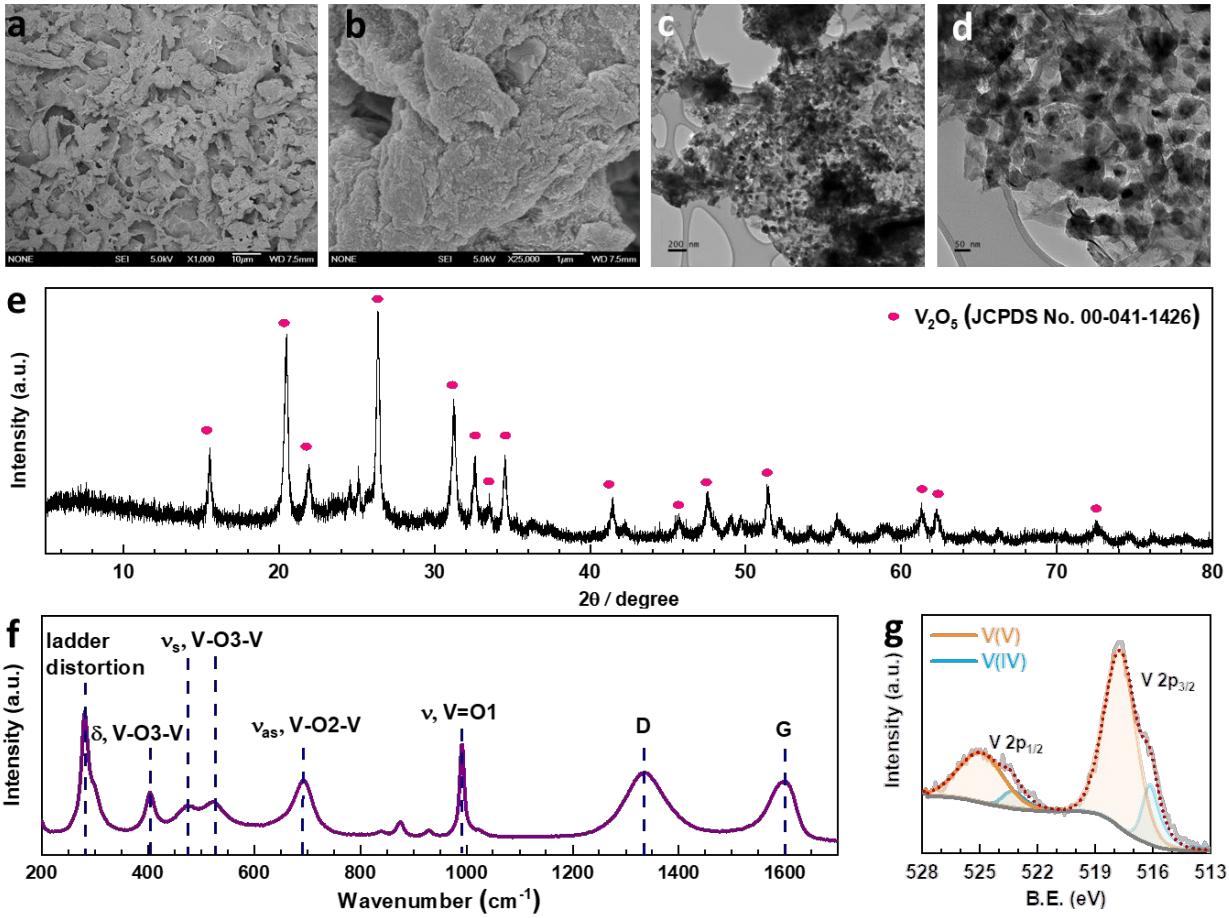

Figure 14b shows that the LSG sheets are evenly and fully coated by V_2O_5 nanoparticles. As illustrated by the TEM images

(

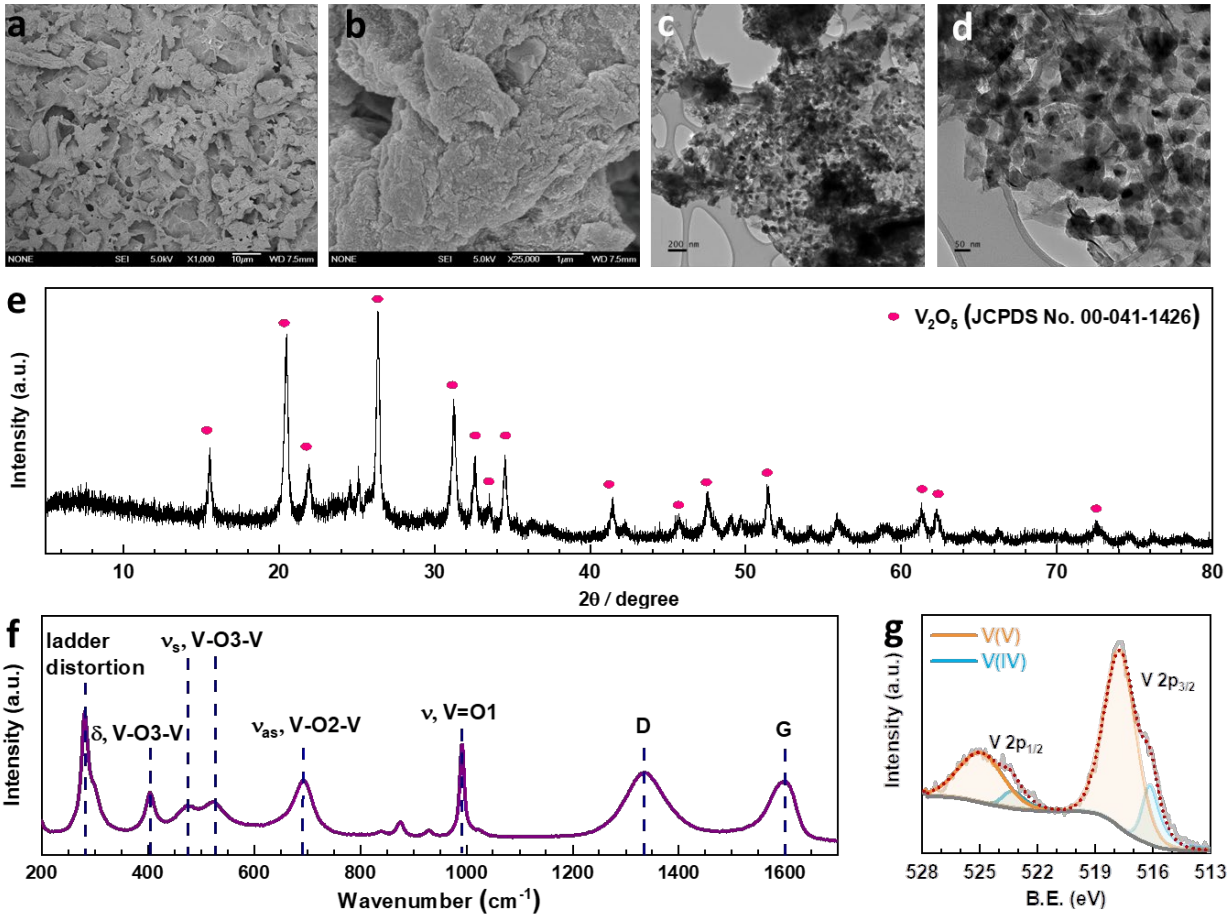

Figure 14c-d), nanoparticles are uniformly distributed on the graphene sheets and are ~50 nm in size. The morphological evidence demonstrates that the interconnected and porous LSG structure is preserved and the V_2O_5 particle size remained within the same order of magnitude after calcination. Additionally, the composition of the synthesized V_2O_5-LSG composite was studied by X-ray powder diffraction (XRD), X-ray photoelectron spectroscopy (XPS) and Raman

spectroscopy.

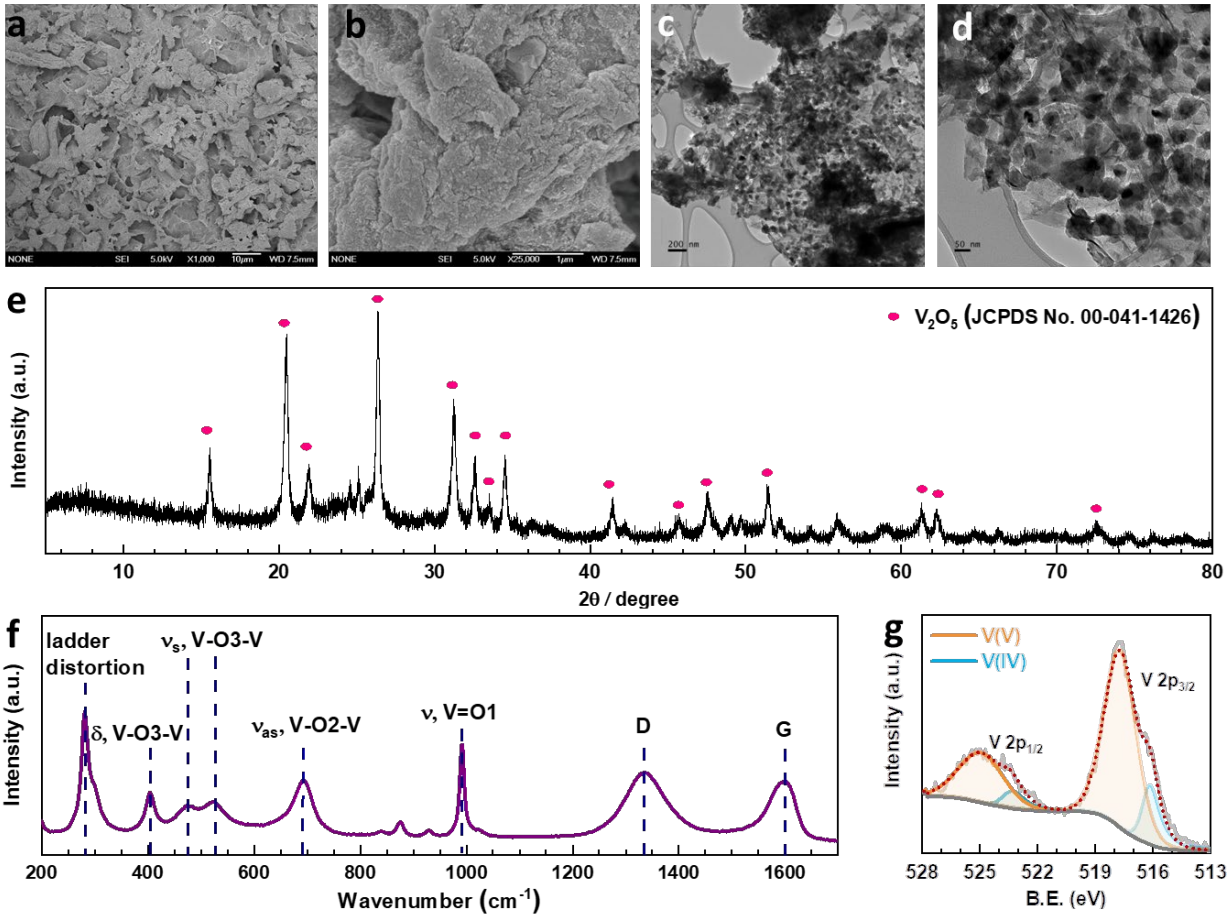

Figure 14e presents the diffraction pattern of the V_2O_5-LSG composite and it matches that of orthorhombic V_2O_5, confirming the formation of V_2O_5 from the lower-valent VCl_3 precursor and VO_x intermediate. The most prominent peaks at 20.4°, 26.3° and 31.2° correspond to the (001), (110) and (310) planes, respectively. The successful synthesis of V_2O_5-LSG was confirmed by Raman spectroscopy, which shows all the V_2O_5 vibrational features as well as the D and G bands of graphene

(

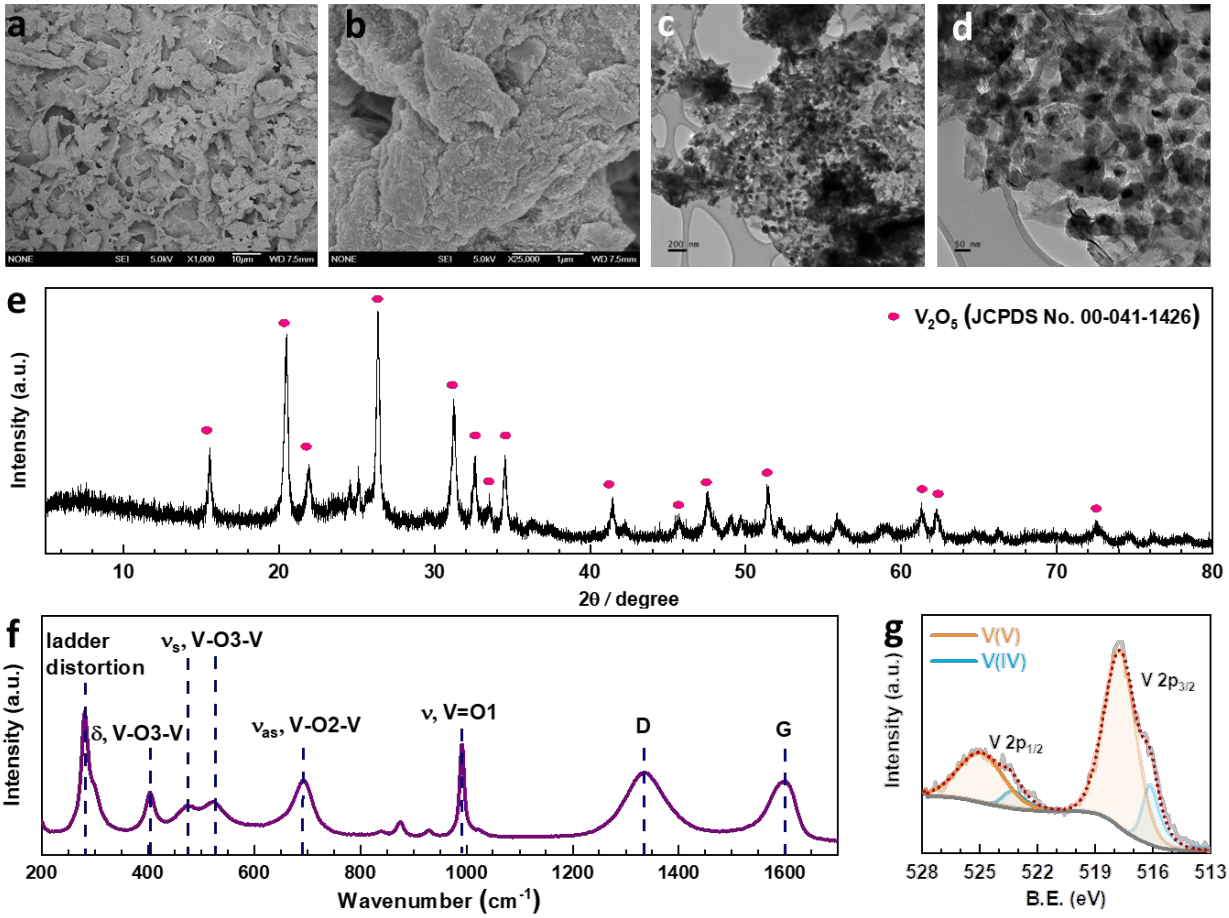

Figure 14f). O1, O2 and O3 denote the out-of-plane terminal, in-plane terminal and in-plane bridging oxygen atoms in V_2O_5, and all the peaks are labeled with the corresponding vibration modes.[22] Furthermore, the complete oxidation of VCl_3 to V_2O_5 is confirmed by the absence of both Cl 2s and Cl 2p peaks in the XPS survey spectrum of V_2O_5-LSG (**Figure S4-24**). As illustrated in the high-resolution V 2p spectrum

(

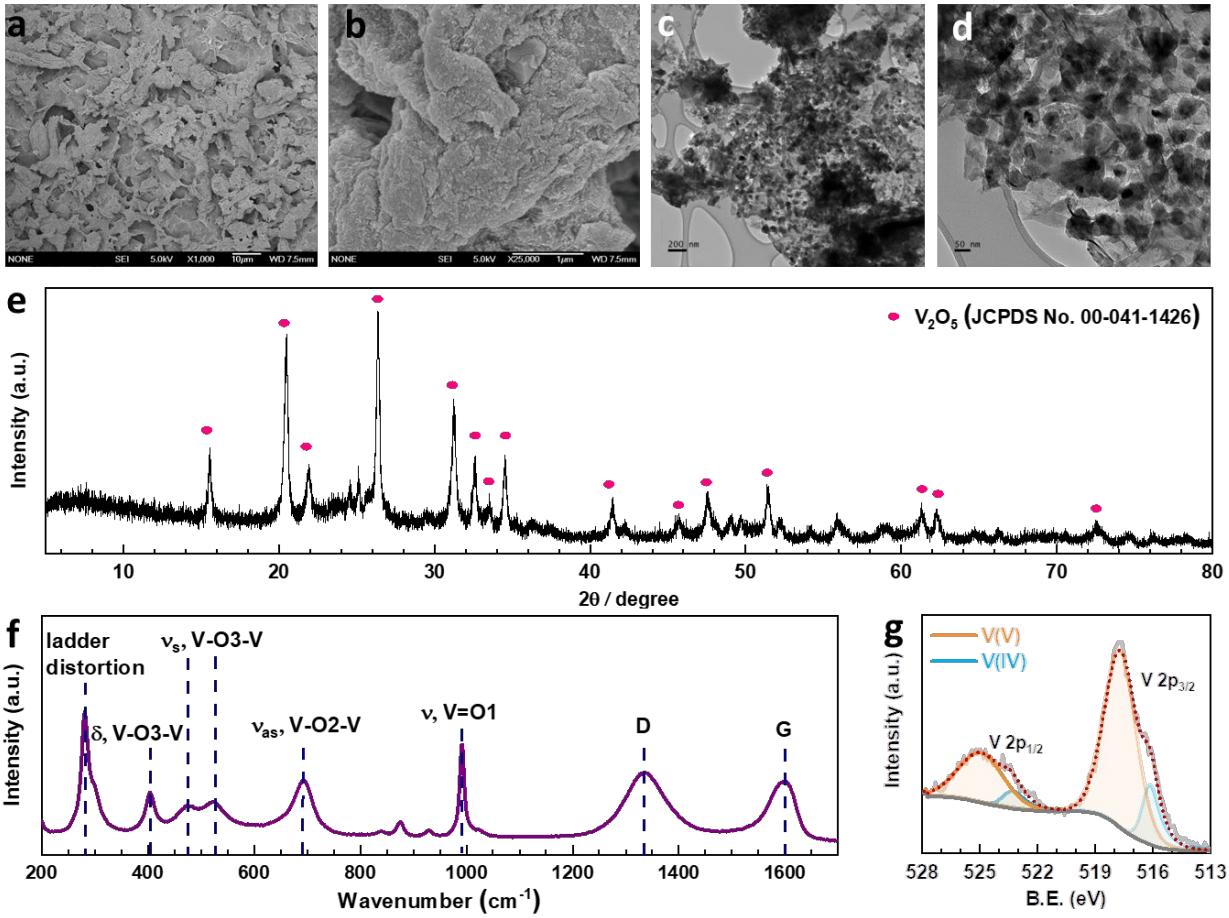

Figure 14g), a major peak at 517.7 eV in the region also indicates that the dominant V oxidation state is 5+ despite the presence of approx. 13.4% V^{4+} at 516.1 eV. Furthermore, since the calcination temperature was chosen to be below 400 °C, above which LSG is vulnerable to thermal oxidation to CO, ~10% of the final V_2O_5- composite is LSG by weight, as signified by the sharp decrease around 400 °C in the thermogravimetric analysis (TGA), as shown in **Figure S4-25**. Overall, all characterization results indicate that the post-laser-scribing calcination step ensures full reaction converting VCl_3 to V_2O_5 without compromising the conductive LSG scaffold, as illustrated in **Figure 13**.

The electrochemical features of the V_2O_5-LSG composite electrodes were first studied using a three-electrode setup in the potential window 0 to -1.4 V vs Ag/AgCl with 21 M lithium bis(trifluoromethane)sulfonimide (LiTFSI) as the electrolyte. As shown in **Figure 15a**, *the CV curves possess broad peaks with small peak-to-peak separations, which is a feature of fast Faradaic charge storage processes and is typical for a redox-active pseudocapacitive material. The voltage profile in* **Figure 15b** *shows two sloping regions with drastically different gradients. From -1.1 V to 0.5 V vs Ag/AgCl, there is a sloping plateau and the capacity contribution from which gradually decreases with increasing current density, indicting rate-dependent battery-type behavior. This is consistent with CV measurements since the most pronounced redox peaks are also observed in the same region. On the other hand, a sloping voltage is always observed between -0.5 V and 0 V vs Ag/AgCl and the gradient stays constant with changing current density, signifying capacitive behavior. As described in* **Figure 15c**, the V_2O_5-LSG composite electrode demonstrated an excellent rate capability in 21 M LiTSFI. At 0.1, 0.2, 0.5 and 1 A g^{-1}, the average discharge capacity can reach 158, 145, 131 and 119 mAh g^{-1}, respectively. Impressively, 75% of the maximum capacity was retained upon a 10-fold rate increase from 0.1 to 1 A g^{-1}. Additionally, ~7% capacity loss was observed in the first cycle, which is speculated to be caused by irreversible formation of LiF from the electrode reaction with LiTSFI.[5] When the rate is returned to 0.1 A g^{-1} in the end, ~95% of the initial capacity was recovered after accounting for the loss from LiF formation. The outstanding rate performance of the V_2O_5-LSG electrode provides a promising foundation for its fast-charging applications in full cells.

To evaluate the electrochemical performance of the V_2O_5-LSG composite in a more practical setting, it was tested as the anode in full cells and paired with an intercalation-type cathode $LiMn_2O_4$, as illustrated in **Figure 16a**. **Figure 16b** shows the CV curves of

the V_2O_5-LSG anode and the $LiMn_2O_4$ cathode. The anode is electrochemically active between 1.8 V and 3.2 V vs. Li/Li^+, which covers the potential ranges of common aqueous lithium-ion battery anodes such as Mo_6S_8 and TiO_2.[4,23] The discharge capacity of the $LiMn_2O_4$ cathode was measured to be 112 mAh g^{-1} (*Figure S4-26)*, which is 29% lower than that of the V_2O_5-LSG anode. *Conventional LIB anodes that have similar specific capacity as* $LiMn_2O_4$ often require doubling the mass of the anode to obtain a suitable n:p ratio in order to compensate for the anode capacity loss due to solid-electrolyte interphase formation;[6] however, since the V_2O_5-LSG anode capacity is 41% higher than that of $LiMn_2O_4$, an anode : cathode mass ratio of 1 was used in all full cell testing. As shown in **Figure 16c**, between 0.5 and 2 V, the CV curves of the V_2O_5-LSG||$LiMn_2O_4$ cell adopt a distorted rectangular shape with prominent redox peaks, which is typical for a hybrid energy storage system.

In order to investigate the kinetics of the charge storage processes in the V_2O_5-LSG||$LiMn_2O_4$ cell, the sharpest pair of peaks that appear between 1.2 and 1.6 V were analyzed. The peak current densities (i) and the scan rates (v) generally obey the following power law:[24,25]

$$i = a\, v^b \tag{1}$$

By plotting $\log(i)$ *of each peak against* $\log(v)$*, the* b*-value of the peak can be determined, and the common consensus is that* b*-values of 0.5 and 1 indicate battery-type and capacitor-type behavior, respectively.* ***Figure 16d*** *illustrates that the anodic and cathodic peaks, respectively, have* b*-values of 0.93 and 0.92 (with* $R^2 = 0.998$*), suggesting that the charge storage mechanism of the* V_2O_5*-LSG||*$LiMn_2O_4$ *system consists of both battery-type and capacitor-type processes that is dominated by the latter. Furthermore, to gain more quantitative insights into the charge storage behavior and decouple the capacity contribution from the diffusion-controlled battery-type and*

the surface-controlled capacitor-type processes, a second kinetic analysis was carried out based on the following relationship:

$$i = k_1 v + k_2 v^{\frac{1}{2}} \quad (2)$$

The *surface-controlled* component ($k_1 v$) and the diffusion-controlled component ($k_2 v^{\frac{1}{2}}$) are proportional to the scan rate and the square root of the scan rate, respectively. **Figure 16e** shows an example where the current contributions from the two types of processes were quantified based on CV data of the system at 1 mV s^{-1}. It is clear that the lower-voltage region (0.5 – 1.2 V) is more predominantly governed by surface-controlled processes, whereas the diffusion-controlled current starts to significantly grow going into the higher-voltage region (1.2 – 2 V). This is consistent with the observation in **Figure 15b**, in which the V_2O_5-LSG anode also presents more battery-type behavior toward higher state-of-charge. This analysis was also carried out using CV data at *0.1, 0.2, 0.5 and 0.8 mV* s^{-1} *and the corresponding capacity quantification is summarized in* **Figure 16f**. The capacity contributed by the diffusion-controlled processes decreased from 79% at 1 mV s^{-1} to 61% at *0.1 mV* s^{-1}. *This indicates that the* charge storage mechanism of the V_2O_5-LSG||$LiMn_2O_4$ system is mainly governed by capacitive processes even at very slow scan rates although the contribution gap between the processes gradually lessens from 1 to *0.1 mV* s^{-1}. *This* capacity dominated by diffusion-controlled contributions of V_2O_5-LSG||$LiMn_2O_4$ gives an excellent foundation for its great electrochemical performance at high rates.

The electrochemical performance of the V_2O_5*-LSG||*$LiMn_2O_4$ *system was assessed in coin cell formats. First, a control experiment was carried out to eliminate any capacity contribution from the graphite paper substrate, and* ***Figure S4-27*** *shows that the substrate gives negligible capacity when paired with a* $LiMn_2O_4$ *cathode. The* V_2O_5*-LSG||*$LiMn_2O_4$ *cell was cycled at C/6, C/3, 1 C and 2 C rates as shown in* ***Figure 17a.*** *The average discharge capacity reached 151, 137, 123 and*

107 mAh (g anode)$^{-1}$, or 75, 69, 61 and 53 mAh g^{-1} based on the total electrode mass, at C/6, C/3, 1 C and 2 C, respectively. With a 12-fold rate increase from C/6 to 2 C, 71% capacity was retained, signifying outstanding fast charging capability. Again, the same initial decrease in capacity is observed, leading to 91% capacity retention when the rate is reversed to C/6, as seen in ***Figure 15c****. The voltage profiles of the V_2O_5-LSG||$LiMn_2O_4$ cell consist of a small plateau around 1.5 V and a voltage slope in the 0.5 – 1.4 V range, indicating that the capacity is predominantly from surface-controlled processes, as illustrated in* ***Figure 17b****. The plateau is a feature of diffusion-controlled Faradaic processes, and its gradient increases with increasing rate, suggesting the capacity contribution from battery-type behavior also falls with increasing rate. This trend corroborates with the kinetics analysis results presented in* ***Figure 16f****, and the plateau voltage matches the peak positions in the CV curves (****Figure 16c****). Additionally, the calcination time in the synthesis to convert VO_x-LSG to V_2O_5-LSG (****Figure 13****) was varied and their average discharge capacities compared in* ***Figure 17c****. On the one hand, with shorter calcination time, the conversion to V_2O_5-LSG may not be complete; on the other hand, the VCl_3 precursor is susceptible to both vaporization and decomposition.[26] Either way, it could lead to a low proportion of the electrochemically active V_2O_5 in the resulting composite, reducing the specific capacity. As shown in* ***Figure 17c****, in comparison to 0.5 h and 2 h, the V_2O_5-LSG anode that underwent calcination for 1 h gives the highest capacity when paired with a $LiMn_2O_4$ cathode, suggesting 1 h is the optimal calcination duration.*

*The V_2O_5-LSG||$LiMn_2O_4$ system was tested for long-term cycling at a 1 C rate (****Figure 17d****). 86% and 75% of the initial capacity were retained after 50 and 100 cycles, respectively. As illustrated in* ***Figure 17e****, the capacity fading is associated with the disappearance of the voltage plateaus around 0.8 and 1.5 V, indicating a change to reduced diffusion-controlled Faradaic processes.*

Furthermore, when a pair of V_2O_5-LSG||$LiMn_2O_4$ cells were connected in series, the battery pack can light up not only red, but also blue LED lights; impressively, the fully charged battery pack can power the LED illumination for more than 24 h.

Finally, several control experiments were carried out to confirm the source of the great electrochemical performance and to evaluate the designed synthetic strategy.

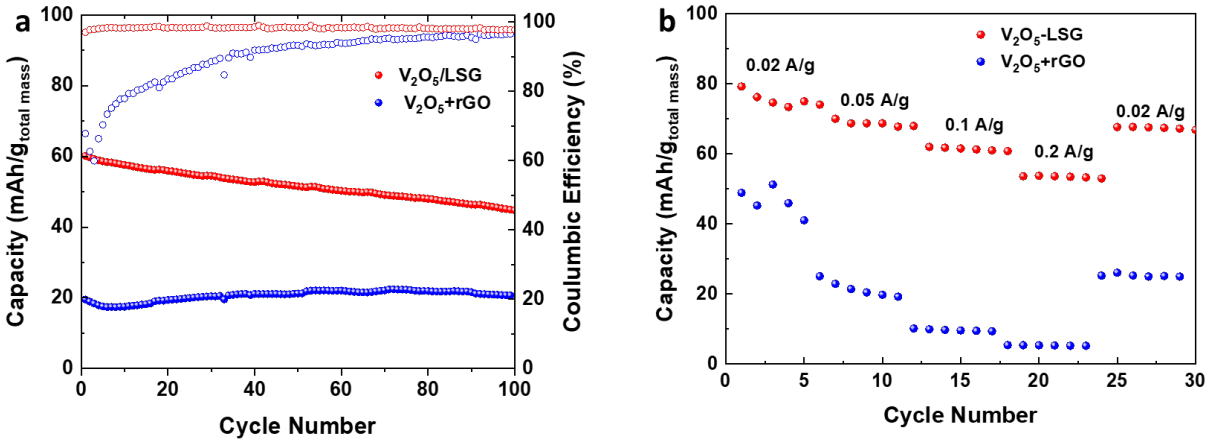

Figure* S4-28** *compares the electrochemical properties of a physical mixture V_2O_5 + rGO to those of the nanoengineered V_2O_5-LSG, and the former shows poor rate capability and cyclability due to the lack of a conductive scaffold and V_2O_5 nanosizing. The V_2O_5-LSG composite electrode fabricated following the synthesis in* ***Figure 13 *is also compared to a sample that only underwent one of either the laser-scribing or calcination steps*

(

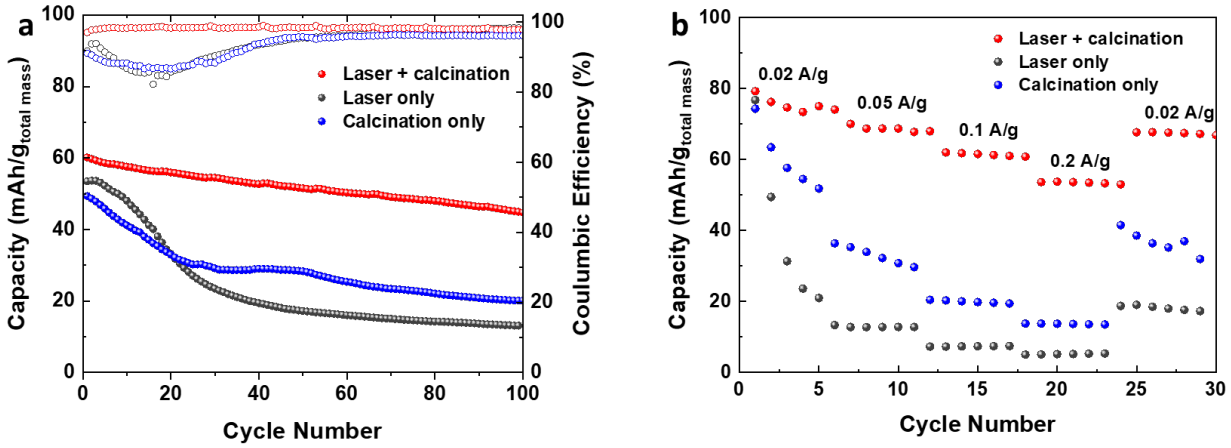

Figure* S4-29). Both the calcination only and laser only sample experienced a sharp capacity decrease at the start, which can be ascribed to the lack of a rigid supportive LSG network and loss of redox-active species due to imcomplete conversion. This confirms the significance of the design strategy presented in* ***Figure 13****. Overall, the meticulously designed V_2O_5-LSG electrode exhibits a high specific capacity and excellent fast-charging properties due to its predominantly surface-controlled charge storage mechanism that is triggered by the V_2O_5-nanoparticle-on-LSG-scaffold structure.*

The electrochemical performance of the V_2O_5-LSG||$LiMn_2O_4$ system is compared to other lithium-ion batteries (LIBs) previously reported in the literature.

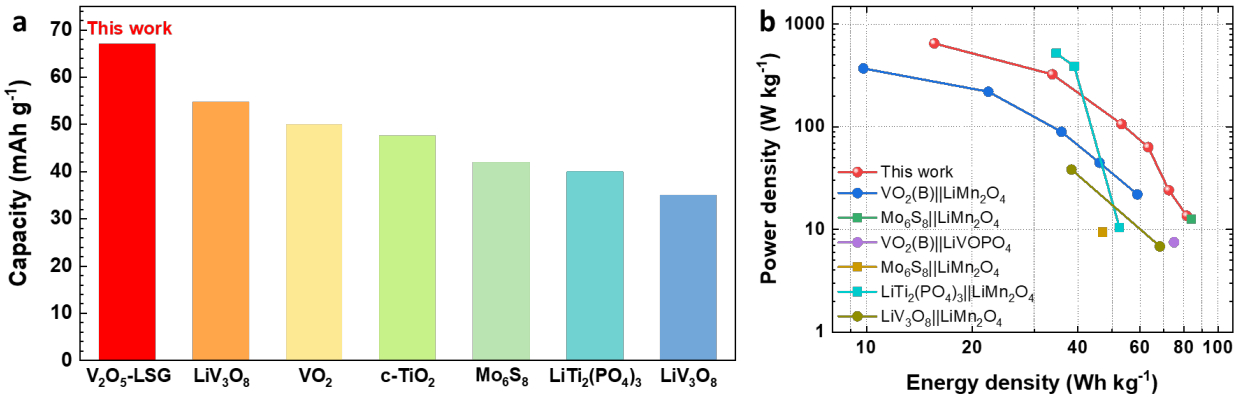

Figure 18a *compares the full-cell specific capacity based on the total mass of both anode and cathode compositions when other aqueous LIB anodes are paired with the $LiMn_2O_4$ cathode.*[5,11,27–30] *The V_2O_5-LSG||$LiMn_2O_4$ system gives the highest specific capacity of 67 mAh g^{-1} (after an initial capacity loss is accounted for) compared to other Ti, Mo and V-based anodes. This competitive advantage is attributed to the high capacity of the designed binder-free V_2O_5-LSG anode. The Ragone plot (*

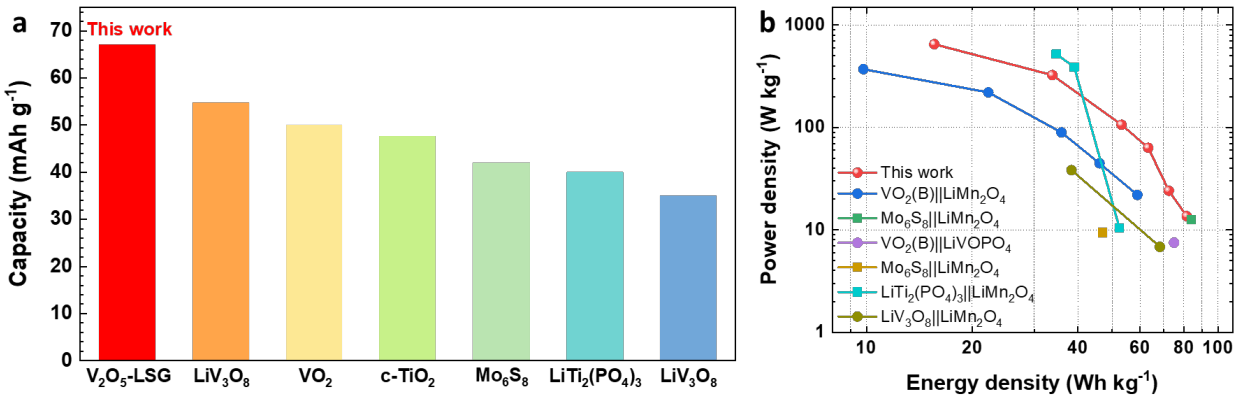

Figure 18b*) compares the energy and power density of the V_2O_5-LSG||$LiMn_2O_4$ cell to the aqueous LIBs reported in the literature.*[5,11,13,27,28,30,31] *The V_2O_5-LSG||$LiMn_2O_4$ system can reach a high*

power density of 650 W kg^{-1} at 15.6 Wh kg^{-1} and a high energy density of 81.5 Wh kg^{-1} at 13.6 W kg^{-1}, outperforming the majority of prior aqueous LIBs. The outstanding power density can be attributed to the predominantly surface-controlled charge storage as illustrated in ***Figure 16f****. Notably, although V-based anodes have a relatively less negative redox potential that leads to lower average full-cell voltages in comparison to Ti and Mo-based anodes, the energy density of the V_2O_5-LSG||$LiMn_2O_4$ cell is actually comparable to if not higher than other aqueous LIBs due to its remarkably high anode capacity. Thus, the V_2O_5-LSG||$LiMn_2O_4$ system exhibits tunable power and energy density and is a promising candidate for fast-charging and safe energy storage applications.*

Conclusions

In summary, a pseudocapacitive composite anode for aqueous lithium ion storage in which V_2O_5 nanoparticles are distributed on a conductive graphene scaffold is reported for applications in aqueous LIBs. The V_2O_5-LSG composite was synthesized from VCl_3/GO precursors by a two-step laser-scribing/calcination approach, resulting in both an expanded LSG structure and fully oxidized V_2O_5 particles that are ~50 nm in size. The V_2O_5-LSG anode can achieve an outstanding average specific capacity of 158 mAh g^{-1} and excellent rate capability as shown in three-electrode measurements. When paired with the intercalation-type cathode $LiMn_2O_4$ cathode, the full cell displays a predominantly surface-controlled charge storage mechanism that is Faradaic in nature, leading to excellent fast charging properties. The V_2O_5-LSG||$LiMn_2O_4$ system shows an average specific capacity of 151 and 107 mAh (g anode)$^{-1}$ at C/6 and 2 C. Furthermore, the full-cell specific capacity as well as power and energy density of this hybrid battery can reach 67 mAh g^{-1}, 650 W kg^{-1} (at 15.6 Wh kg^{-1}) and 81.5 Wh kg^{-1} at (13.6 W kg^{-1}) respectively, all of which compare favorably to previously reported aqueous LIBs. Thanks to its high capacity, fast charging

capability and safe operation, the V_2O_5-LSG||$LiMn_2O_4$ system provides a potential solution for future energy storage applications.

Conflicts of interest

R.B.K. hold an equity interest in Nanotech Energy, Inc.

Acknowledgement

The authors thank Dr. Myung Ki Hong, Endowed Chair in Materials Innovation at UCLA, for financial support (R.B.K.).

References

(1) Ju, Z.; Zhao, Q.; Chao, D.; Hou, Y.; Pan, H.; Sun, W.; Yuan, Z.; Li, H.; Ma, T.; Su, D.; Jia, B. Energetic Aqueous Batteries. *Adv Energy Mater* **2022**, *12* (27), 2201074. https://doi.org/10.1002/aenm.202201074.

(2) Chen, S.; Zhang, M.; Zou, P.; Sun, B.; Tao, S. Historical Development and Novel Concepts on Electrolytes for Aqueous Rechargeable Batteries. *Energy Environ Sci* **2022**, *15* (5), 1805–1839. https://doi.org/10.1039/D2EE00004K.

(3) Li, Q.; Chen, J.; Fan, L.; Kong, X.; Lu, Y. Progress in Electrolytes for Rechargeable Li-Based Batteries and Beyond. *Green Energy & Environment* **2016**, *1* (1), 18–42. https://doi.org/10.1016/J.GEE.2016.04.006.

(4) Lukatskaya, M. R.; Feldblyum, J. I.; Mackanic, D. G.; Lissel, F.; Michels, D. L.; Cui, Y.; Bao, Z. Concentrated Mixed Cation Acetate "Water-in-Salt" Solutions as Green and Low-Cost High Voltage Electrolytes for Aqueous Batteries. *Energy Environ Sci* **2018**, *11* (10), 2876–2883. https://doi.org/10.1039/C8EE00833G.

(5) Suo, L.; Borodin, O.; Gao, T.; Olguin, M.; Ho, J.; Fan, X.; Luo, C.; Wang, C.; Xu, K. "Water-in-Salt" Electrolyte Enables High-Voltage Aqueous Lithium-Ion Chemistries. *Science (1979)* **2015**, *350* (6263), 938–943. https://doi.org/10.1126/science.aab1595.

(6) Ao, H.; Zhao, Y.; Zhou, J.; Cai, W.; Zhang, X.; Zhu, Y.; Qian, Y. Rechargeable Aqueous Hybrid Ion Batteries: Developments and Prospects. *J Mater Chem A Mater* **2019**, *7* (32), 18708–18734. https://doi.org/10.1039/C9TA06433H.

(7) Liu, J.; Xu, C.; Chen, Z.; Ni, S.; Shen, Z. X. Progress in Aqueous Rechargeable Batteries. *Green Energy & Environment* **2018**, *3* (1), 20–41. https://doi.org/10.1016/J.GEE.2017.10.001.

(8) Wang, Y.; Yi, J.; Xia, Y. Recent Progress in Aqueous Lithium-Ion Batteries. *Adv Energy Mater* **2012**, *2* (7), 830–840. https://doi.org/10.1002/aenm.201200065.

(9) Zuo, W.; Li, R.; Zhou, C.; Li, Y.; Xia, J.; Liu, J. Battery-Supercapacitor Hybrid Devices: Recent Progress and Future Prospects. *Advanced Science* **2017**, *4* (7), 1600539. https://doi.org/10.1002/advs.201600539.

(10) Sun, Y.; Jiang, S.; Bi, W.; Wu, C.; Xie, Y. Highly Ordered Lamellar V2O3-Based Hybrid Nanorods towards Superior Aqueous Lithium-Ion Battery Performance. *J Power Sources* **2011**, *196* (20), 8644–8650. https://doi.org/10.1016/J.JPOWSOUR.2011.06.050.

(11) Li, W.; Dahn, J. R.; Wainwright, D. S. Rechargeable Lithium Batteries with Aqueous Electrolytes. *Science (1979)* **1994**, *264* (5162), 1115–1118. https://doi.org/10.1126/science.264.5162.1115.

(12) Shao, M.; Deng, J.; Zhong, F.; Cao, Y.; Ai, X.; Qian, J.; Yang, H. An All-Vanadium Aqueous Lithium Ion Battery with High Energy Density and Long Lifespan. *Energy Storage Mater* **2019**, *18*, 92–99. https://doi.org/10.1016/J.ENSM.2018.09.029.

(13) Wang, G. J.; Zhang, H. P.; Fu, L. J.; Wang, B.; Wu, Y. P. Aqueous Rechargeable Lithium Battery (ARLB) Based on LiV3O8 and LiMn2O4 with Good Cycling Performance. *Electrochem commun* **2007**, *9* (8), 1873–1876. https://doi.org/10.1016/j.elecom.2007.04.017.

(14) Augustyn, V.; Simon, P.; Dunn, B. Pseudocapacitive Oxide Materials for High-Rate Electrochemical Energy Storage. *Energy Environ Sci* **2014**, *7* (5), 1597–1614. https://doi.org/10.1039/C3EE44164D.

(15) Simon, P.; Gogotsi, Y.; Dunn, B. Where Do Batteries End and Supercapacitors Begin? *Science*. American Association for the Advancement of Science March 14, 2014, pp 1210–1211. https://doi.org/10.1126/science.1249625.

(16) Choi, C.; Ashby, D. S.; Butts, D. M.; DeBlock, R. H.; Wei, Q.; Lau, J.; Dunn, B. Achieving High Energy Density and High Power Density with Pseudocapacitive Materials. *Nature Reviews Materials 2019 5:1* **2019**, *5* (1), 5–19. https://doi.org/10.1038/s41578-019-0142-z.

(17) Manthiram, A. A Reflection on Lithium-Ion Battery Cathode Chemistry. *Nature Communications*. Nature Publishing Group March 25, 2020, pp 1–9. https://doi.org/10.1038/s41467-020-15355-0.

(18) Wang, L. J.; El-Kady, M. F.; Dubin, S.; Hwang, J. Y.; Shao, Y.; Marsh, K.; McVerry, B.; Kowal, M. D.; Mousavi, M. F.; Kaner, R. B. Flash Converted Graphene for Ultra-High Power Supercapacitors. *Adv Energy Mater* **2015**, *5* (18), 1500786. https://doi.org/10.1002/aenm.201500786.

(19) Huang, A.; El-Kady, M. F.; Chang, X.; Anderson, M.; Lin, C.; Turner, C. L.; Kaner, R. B. Facile Fabrication of Multivalent VO x /Graphene Nanocomposite Electrodes for High-Energy-Density Symmetric Supercapacitors. *Adv Energy Mater* **2021**, *11* (26), 2100768. https://doi.org/10.1002/aenm.202100768.

(20) Hwang, J. Y.; El-Kady, M. F.; Wang, Y.; Wang, L.; Shao, Y.; Marsh, K.; Ko, J. M.; Kaner, R. B. Direct Preparation and Processing of Graphene/RuO2 Nanocomposite Electrodes for

High-Performance Capacitive Energy Storage. *Nano Energy* **2015**, *18*, 57–70. https://doi.org/10.1016/j.nanoen.2015.09.009.

(21) Hwang, J. Y.; El-Kady, M. F.; Li, M.; Lin, C. W.; Kowal, M.; Han, X.; Kaner, R. B. Boosting the Capacitance and Voltage of Aqueous Supercapacitors via Redox Charge Contribution from Both Electrode and Electrolyte. *Nano Today* **2017**, *15*, 15–25. https://doi.org/10.1016/j.nantod.2017.06.009.

(22) Smirnov, M. B.; Roginskii, E. M.; Smirnov, K. S.; Baddour-Hadjean, R.; Pereira-Ramos, J.-P. Unraveling the Structure–Raman Spectra Relationships in V 2 O 5 Polymorphs via a Comprehensive Experimental and DFT Study. *Inorg Chem* **2018**, *57* (15), 9190–9204. https://doi.org/10.1021/acs.inorgchem.8b01212.

(23) Hou, Z.; Dong, M.; Xiong, Y.; Zhang, X.; Zhu, Y.; Qian, Y. Formation of Solid–Electrolyte Interfaces in Aqueous Electrolytes by Altering Cation-Solvation Shell Structure. *Adv Energy Mater* **2020**, *10* (15), 1903665. https://doi.org/10.1002/aenm.201903665.

(24) Augustyn, V.; Come, J.; Lowe, M. A.; Kim, J. W.; Taberna, P.-L.; Tolbert, S. H.; Abruña, H. D.; Simon, P.; Dunn, B. High-Rate Electrochemical Energy Storage through Li+ Intercalation Pseudocapacitance. *Nat Mater* **2013**, *12* (6), 518–522. https://doi.org/10.1038/nmat3601.

(25) Lindström, H.; Södergren, S.; Solbrand, A.; Rensmo, H.; Hjelm, J.; Hagfeldt, A.; Lindquist, S.-E. Li + Ion Insertion in TiO 2 (Anatase). 1. Chronoamperometry on CVD Films and Nanoporous Films. *J Phys Chem B* **1997**, *101* (39), 7710–7716. https://doi.org/10.1021/jp970489r.

(26) McCarley, R. E.; Roddy, J. W. The Vapor Pressures of Vanadium(II) Chloride, Vanadium(III) Chloride, Vanadium(II) Bromide, and Vanadium(III) Bromide by Knudsen Effusion. *Inorg Chem* **1964**, *3* (1), 60–63. https://doi.org/10.1021/ic50011a012.

(27) Lin, C.-H.; Sun, K.; Ge, M.; Housel, L. M.; McCarthy, A. H.; Vila, M. N.; Zhao, C.; Xiao, X.; Lee, W.-K.; Takeuchi, K. J.; Takeuchi, E. S.; Marschilok, A. C.; Chen-Wiegart, Y. K. Systems-Level Investigation of Aqueous Batteries for Understanding the Benefit of Water-in-Salt Electrolyte by Synchrotron Nanoimaging. *Sci Adv* **2020**, *6* (10), 1–12. https://doi.org/10.1126/sciadv.aay7129.

(28) Suo, L.; Borodin, O.; Sun, W.; Fan, X.; Yang, C.; Wang, F.; Gao, T.; Ma, Z.; Schroeder, M.; von Cresce, A.; Russell, S. M.; Armand, M.; Angell, A.; Xu, K.; Wang, C. Advanced High-Voltage Aqueous Lithium-Ion Battery Enabled by "Water-in-Bisalt" Electrolyte. *Angewandte Chemie International Edition* **2016**, *55* (25), 7136–7141. https://doi.org/10.1002/anie.201602397.

(29) Luo, J.-Y.; Xia, Y.-Y. Aqueous Lithium-Ion Battery LiTi2(PO4)3/LiMn2O4 with High Power and Energy Densities as Well as Superior Cycling Stability**. *Adv Funct Mater* **2007**, *17* (18), 3877–3884. https://doi.org/10.1002/adfm.200700638.

(30) Suo, L.; Han, F.; Fan, X.; Liu, H.; Xu, K.; Wang, C. "Water-in-Salt" Electrolytes Enable Green and Safe Li-Ion Batteries for Large Scale Electric Energy Storage Applications. *J Mater Chem A Mater* **2016**, *4* (17), 6639–6644. https://doi.org/10.1039/C6TA00451B.

(31) Sun, D.; Tang, Y.; He, K.; Ren, Y.; Liu, S.; Wang, H. Long-Lived Aqueous Rechargeable Lithium Batteries Using Mesoporous LiTi2(PO4)3@C Anode. *Sci Rep* **2015**, *5* (1), 17452. https://doi.org/10.1038/srep17452.

(32) Hummers, W. S.; Offeman, R. E. Preparation of Graphitic Oxide. *J Am Chem Soc* **1958**, *80* (6), 1339–1339. https://doi.org/10.1021/ja01539a017.

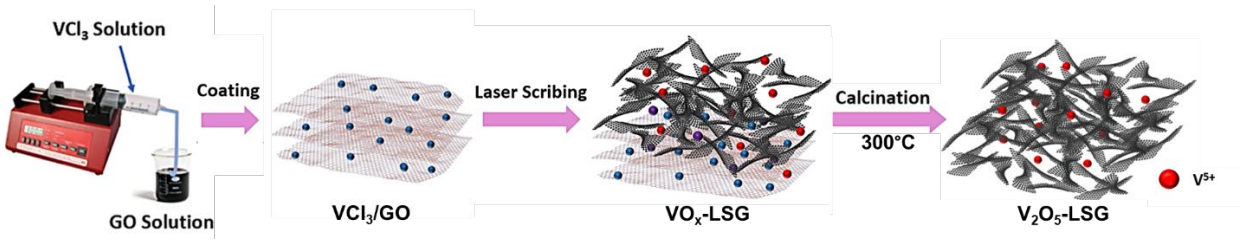

Figure 13. Schematic illustration of V_2O_5-LSG synthesis via laser scribing and calcination.

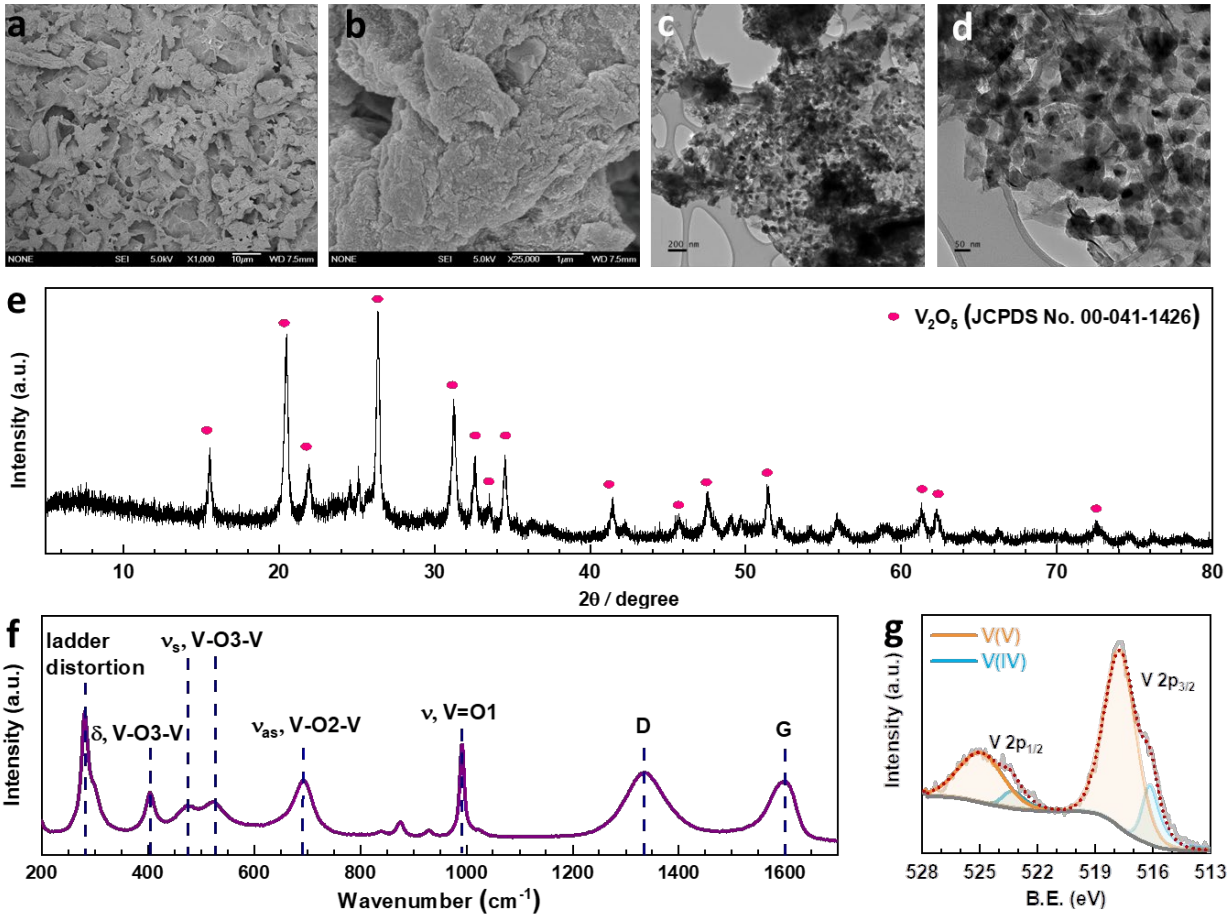

Figure 14. Characterization of the as-synthesized V_2O_5-LSG composite (calcination time = 1 h). (a-b) Low- and high-magnification SEM images of the V_2O_5-LSG composite. (c-d) A TEM image showing the V_2O_5 particles on the rGO sheets. (e) XRD pattern of V_2O_5-LSG matching V_2O_5 (JCPDS no. 00-001-0359). (f) Raman spectra of the composite showing V_2O_5 and graphene features. (g) XPS V 2p region of the V_2O_5-LSG composite spectra.

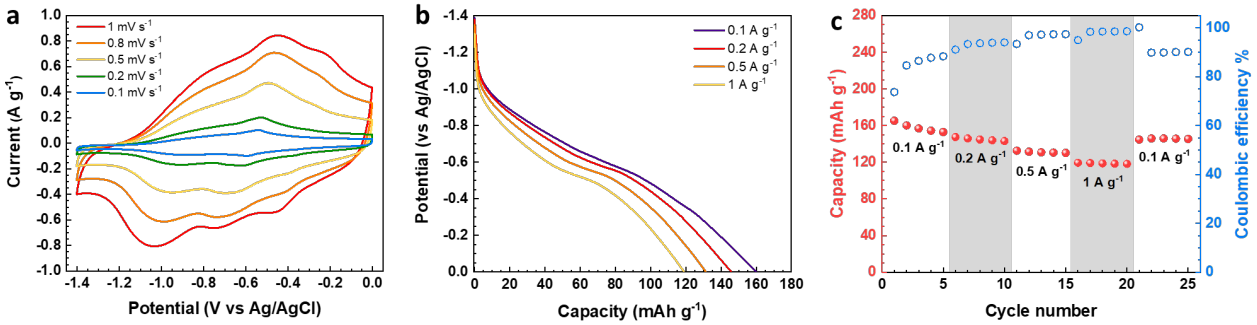

Figure 15. *Electrochemical measurements of the* V_2O_5-LSG electrode *in a three-electrode setup. (a) Cyclic voltammetry curves for* V_2O_5-LSG *at 0.1, 0.2, 0.5, 0.8, 1 mV* s^{-1}*. (b) Capacity-voltage profiles at 0.1, 0.2, 0.5, 1 A* g^{-1}*. (c) Rate performance and corresponding Coulombic efficiency of* V_2O_5-LSG cycled at different current densities.

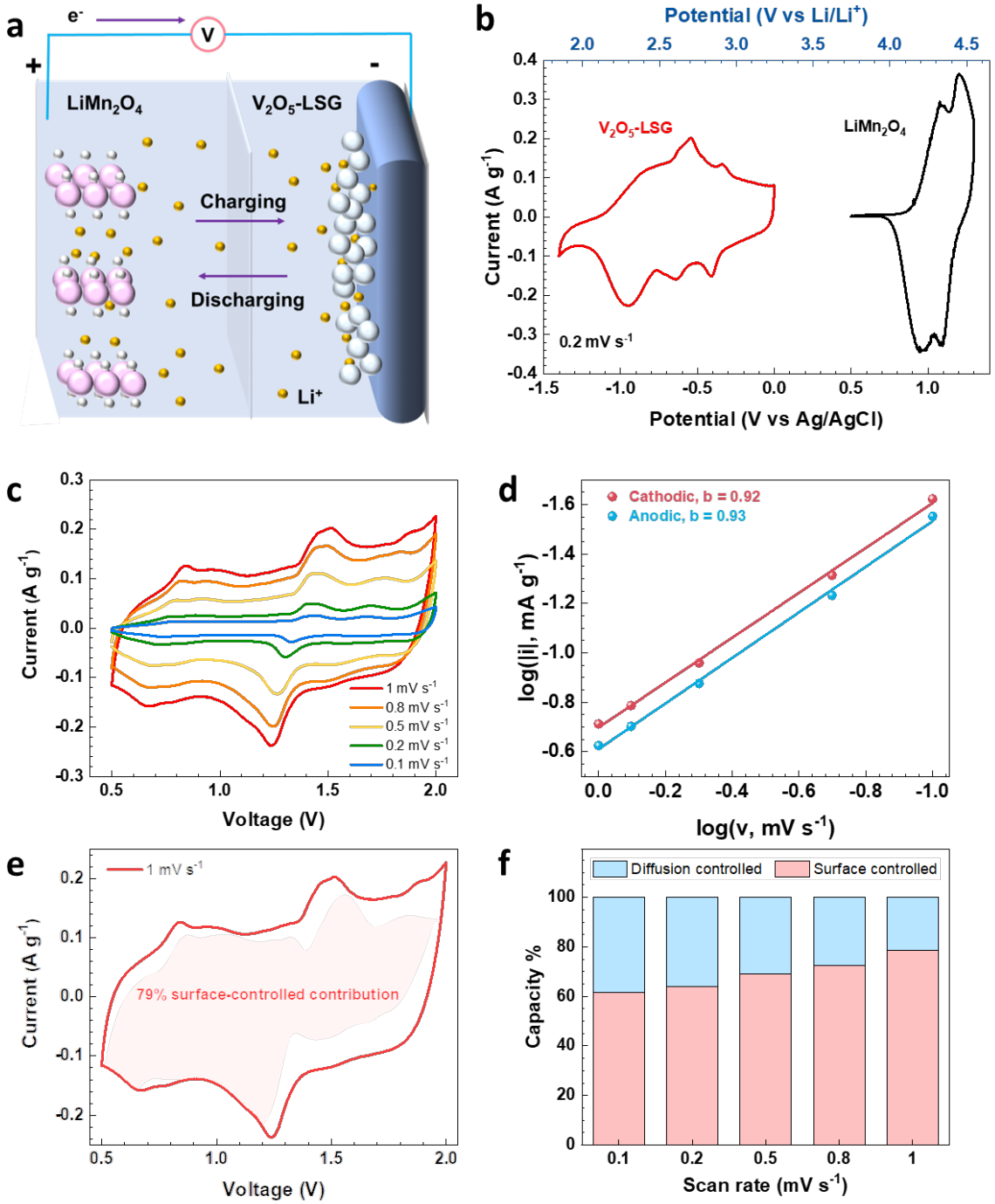

Figure 16. *Electrochemical analysis of the* V_2O_5-LSG||$LiMn_2O_4$ *cells. (a) Illustration of Li-ion storage in the hybrid system based on a pseudocapacitive anode and an intercalation-type cathode. (b) Potential windows of* V_2O_5-LSG and $LiMn_2O_4$ in 21 M LiTFSI electrolyte. (c) *Cyclic voltammetry curves of a* V_2O_5-LSG||$LiMn_2O_4$ coin *cell at 0.1, 0.2, 0.5, 0.8, and 1 mV* s^{-1}. *(d) b-values of the most pronounced pair of peaks in the CV. (e) Current contribution by surface-controlled processes at 1 mV* s^{-1}. *(f) Capacity contribution by surface-controlled and diffusion-controlled processes at a range of scan rates.*

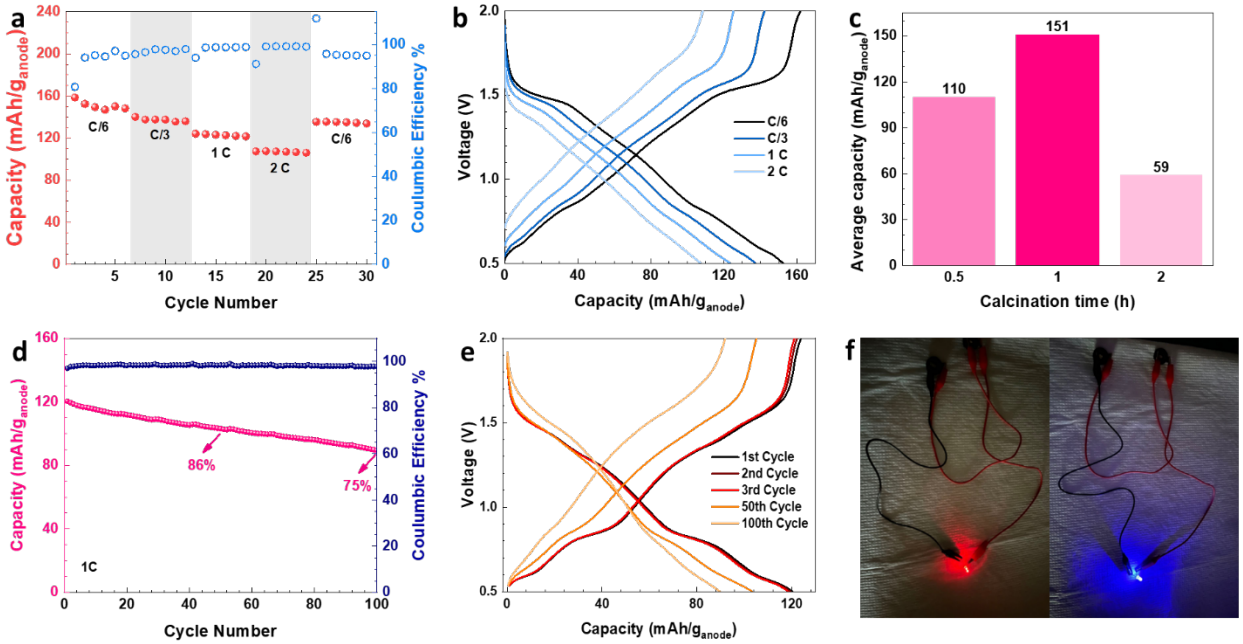

Figure 17. *Electrochemical performance of the* V_2O_5-LSG||$LiMn_2O_4$ coin *cells. (a) Rate performance and corresponding Coulombic efficiency of a* V_2O_5-LSG||$LiMn_2O_4$ cell cycled at 0.2 C, 0.5 C, 1C, 2C and 0.2 C. *(b) Capacity-voltage profiles at different rates. (c) Specific capacity comparison between samples synthesized with 0.5, 1, 2 h of calcination. (d) Capacity and Coulombic efficiency of a* V_2O_5-LSG||$LiMn_2O_4$ cell over 1 C *cycling. (e) Capacity-voltage profiles of the 1st, 2nd, 3rd, 50th, and 100th cycles during 1 C cycling. (f) Optical images of LED bulbs powered by 2* V_2O_5-LSG||$LiMn_2O_4$ coin *cells connected in series.*

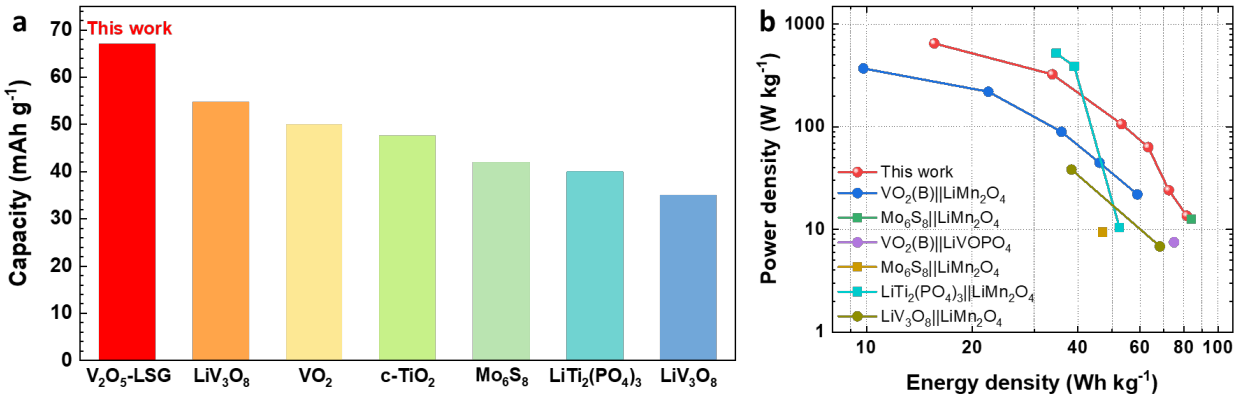

Figure 18. *Performance comparison of* V_2O_5-LSG||$LiMn_2O_4$ to previously reported systems in the literature. *(a) A capacity comparison based on total electrode mass of* V_2O_5-LSG||$LiMn_2O_4$ *to those of other aqueous Li-ion batteries reported in the literature.*[5,11,27–30] *(b) A Ragone plot comparing power and energy densities based on total electrode mass of* V_2O_5-LSG||$LiMn_2O_4$ *to those of other aqueous Li-ion batteries reported in the literature.*

Supporting Information

Experimental

Synthesis of V_2O_5-LSG: Graphite oxide (GO) was synthesized via a modified Hummer's method.[32] In a typical synthesis, 160 mg of freeze-fried GO powder was diluted with the addition of 5.8 mL of DI water and dispersed by 2-minute tip sonication. 40 mg of VCl_3 (Fisher Scientific) was dissolved in 4.2 mL of DI water and bath sonicated for 2 hrs. Next, the VCl_3 solution was uniformly added to the GO suspension within 1 h via a syringe pump while stirring. The resulting mixture was then drop-cast onto graphite paper (Panasonic) at a density of 200 μL cm^{-2} and left to dry under ambient conditions. Next, the dried film was laser-scribed using a 40 W Full Spectrum Laser Muse 2D Vision Desktop CO_2 Laser Cutter with a 12% power setting, and electrodes were cut out of the film using a 10 mm hole punch. Finally, the electrodes were placed in a furnace which was set to 60 °C for 1 h, ramped up to 300 °C at 2 °C/min and then left at 300 °C for 0.5, 1 or 2 h. The as-made V_2O_5-LSG electrodes were weighed using a micro-balance and the electrode mass was determined to be 1.4 – 1.6 mg.

Materials characterization: Scanning electron microscopy (SEM) images of the V_2O_5-*L*SG composite were collected using a JEOL JSM-67 Field Emission Scanning Electron Microscope. Transmission electron microscopy (TEM) was performed on a Tecnai G2 T20 iCorr TEM (FEI Inc.). X-ray powder diffraction (XRD) was performed using a Panalytical X'Pert Pro X-ray powder diffractometer using Cu Kα radiation with a wavelength of 0.154 nm on a SiO_2 crystal zero-background plate. In order to eliminate the coinciding signals from graphite paper, glass slides were used as the substrate instead and the active materials were scratched off to maximize the signals. The unassigned small peaks in the spectra are from SiO_2 impurities. The X-ray

photoelectron spectroscopy (XPS) spectra were acquired using a Kratos Axis Ultra DLD spectrometer equipped with a monochromatic Al Kα X-ray source. The mass of the electrode was measured by a Mettler Toledo MX5 microbalance with 0.001 mg sensitivity. Raman spectroscopy was carried out using a Reinshaw inVia confocal Raman microscope with a 633 nm laser.

Fabrication of $LiMn_2O_4$ and *rGO/V_2O_5*: The active material, $LiMn_2O_4$ (MTI) or V_2O_5 (Sigma-Aldrich) was mixed with conductive carbon black or rGO, and PVDF binder, in the ratio 85:10:5. The slurry was cast on a graphite paper substrate using a doctor-blade and then punched into 10 mm discs. The resulting electrode mass was determined to be 1.4 – 1.6 mg.

Electrochemical testing: There-electrode measurements including cyclic voltammetry (CV), galvanostatic charge-discharge (GCD) and electrochemical impedance spectroscopy (EIS) measurements were carried out using a Biologic VMP3 electrochemical workstation (VMP3b-10, USA Science Instrument). For three-electrode experiments, graphite paper and an Ag/AgCl electrode were used as the counter and reference electrodes, respectively. The electrolyte is 21 M lithium bis(trifluoromethane)sulfonimide (LiTFSI) unless stated otherwise. Coin cell tests were carried with an approximately equal mass of cathode and anode using an MTI battery cycler.

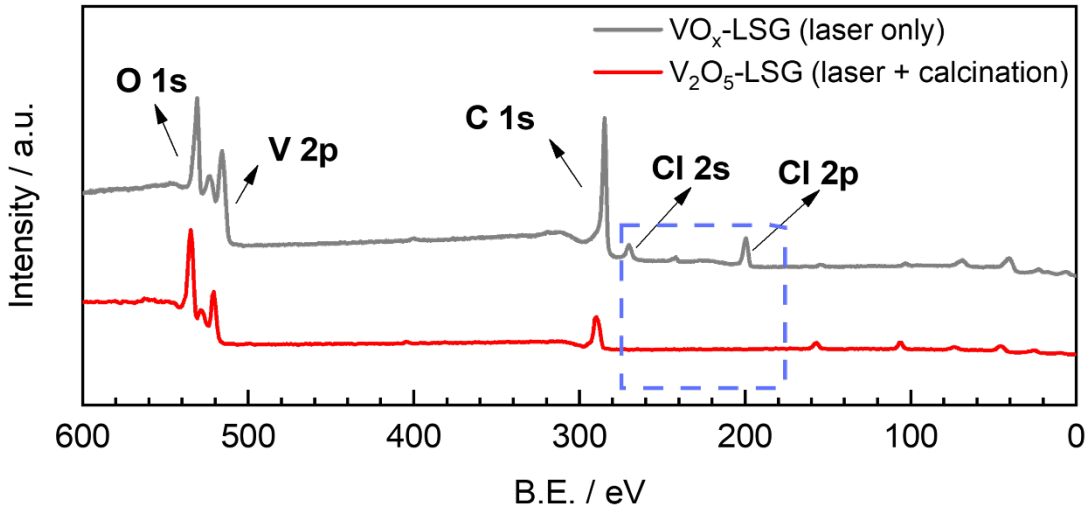

Figure S4-24. XPS survey spectra of V_2O_5-LSG and VO_x-LSG.

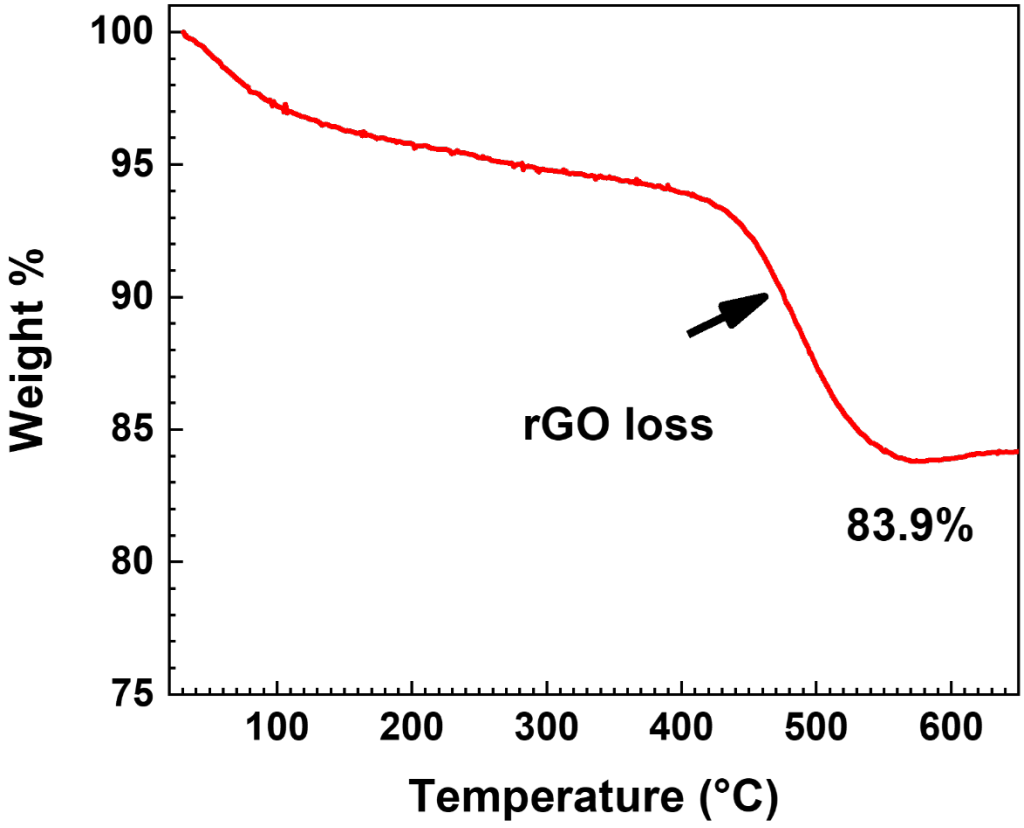

Figure S4-25. Thermogravimetric analysis of V_2O_5-LSG.

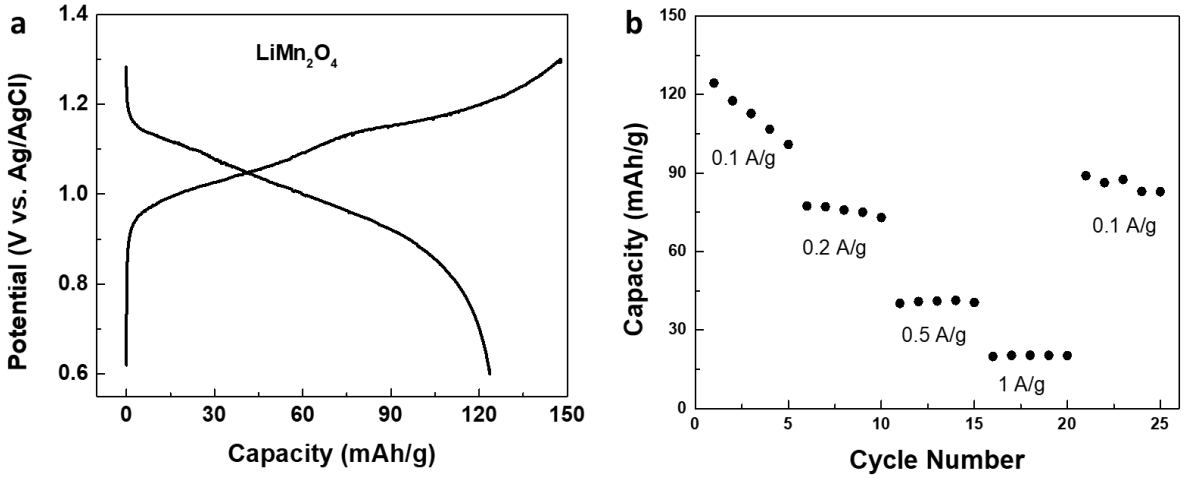

Figure S4-26. (a) Voltage profile and (b) rate performance of a $LiMn_2O_4$ cathode.

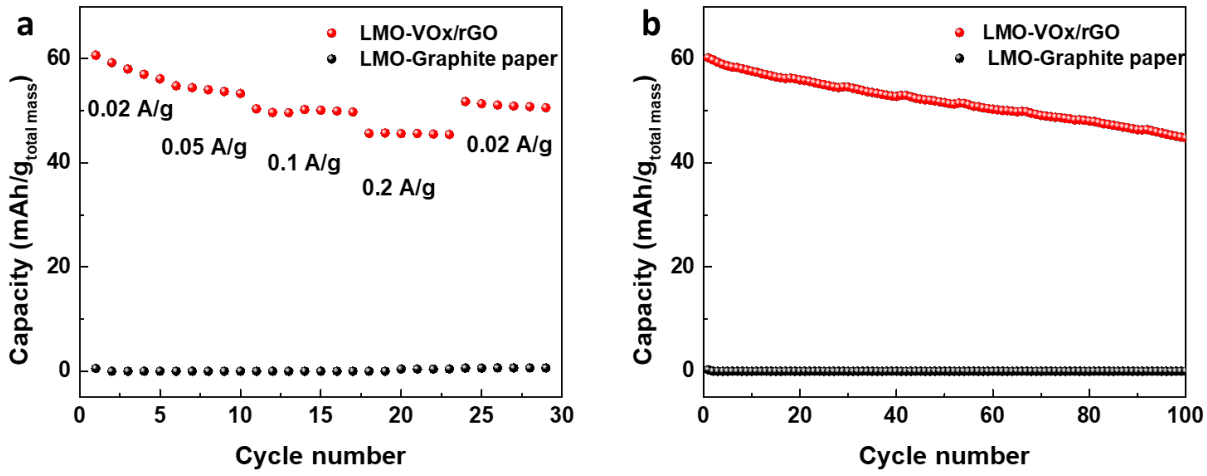

Figure S4-27. (a) Voltage profile and (b) rate performance of a graphite paper||$LiMn_2O_4$ cell.

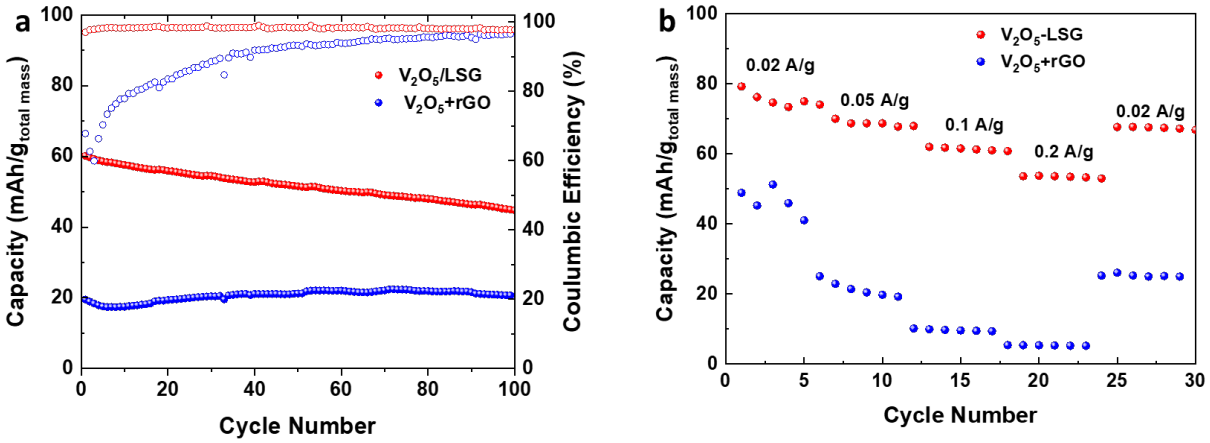

Figure S4-28. (a) Voltage profile and (b) rate performance of a V_2O_5+rGO||$LiMn_2O_4$ cell.

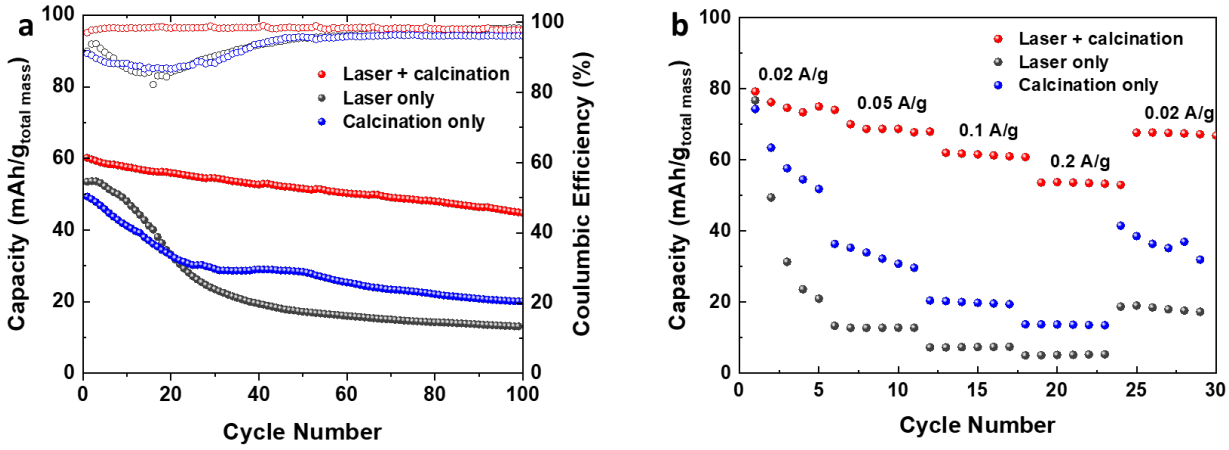

Figure S4-29. (a) Voltage profile and (b) rate performance of calcination only and laser only anodes paired with an $LiMn_2O_4$ cathode.

Chapter 5. Outlooks and Future Work

It was demonstrated in **Chapters 2-4** that the simple synthesis via CO_2 laser scribing can give electrodes with superior electrochemical performance and favorable charge transfer kinetics. By this kinetically controlled process, multivalent vanadium oxides can be preferentially formed from the chloride precursor, allowing a multielectron redox couple. In this way, the thin-film electrodes can achieve high specific capacitance, enabling the supercapacitor system to reach energy densities that are close to battery level, as seen in **Chapter 2**. Moreover, with an additional calcination step to ensure the complete conversion to vanadium oxides and to increase the active material loading, the pseudocapacitive materials can be adapted to battery chemistry. While the predominantly surface-controlled charge transfer mechanism remained, pronounced Faradaic features were observed, resulting in not only excellent fast charging capability but also high specific capacity, as described in **Chapters 3-4**.

Although the previous chapters provide successful examples of integrating laser-scribed vanadium oxides/graphene composite electrodes into different energy storage systems, the following challenges still need to be addressed:

1) Due to the limited penetration of the CO_2 laser, relatively low mass loadings have been achieved even with the aid of calcination, hindering the development of electrodes with commercial-level areal mass loading or freestanding electrodes.
2) Despite the compatible electrochemical potential with zinc-, sodium- and magnesium-ion systems, vanadium compounds generally limit the voltage window of LIBs due to their lower electrochemical potential in comparison to other cathode materials.

3) Although laser-scribing gives a fast and facile route to nanocomposites, there is little control over the morphology and phase of the product owing to the chaotic nature of the process.

Considering the challenges above, the following strategies can be experimented with as possible solutions. Previously former lab members reported other approaches to make freestanding nanostructured rGO scaffold via freeze-casting[1] and flash conversion.[2] Combining the two concepts, a mixture of GO (or partially reduced GO) and a transition metal compound precursor can be freeze-dried first, and the powder can subsequently undergo photothermal treatment. This strategy was experimented with the VCl_3 precursor, and it was discovered that the higher-power CO_2 laser was required for the conversion to vanadium oxides. However, the resulting powder product only possessed the high specific capacity as seen with the film electrode but lacked the rate capability. VCl_3 is highly hygroscopic and rapidly separates from GO upon freezing in liquid nitrogen; thus, a precursor compound with suitable physical and chemical properties should be found to further develop this strategy. The precursor compound is not limited to vanadium compounds and can be salts of other common transition metals such as Mn, Co, Ni, Ti, Mo, etc. The high yield and increased areal mass loading can improve the practicality of the electrode materials. Furthermore, in order to control the phase of the final transition metal product, a preliminary solvothermal step can be introduced. Many synthetic approaches in the literature are two-step processes where the final products are made from controlled intermediates,[3–9] and previous work showed that laser-scribing can achieve similar chemical conversions as solvothermal methods,[10] therefore, laser-scribing an intermediate mixture made from a controlled

synthesis could take advantage of both types of processes and result in next-generation high-performance electrode materials.

References

(1) Shao, Y.; El-Kady, M. F.; Lin, C.-W.; Zhu, G.; Marsh, K. L.; Hwang, J. Y.; Zhang, Q.; Li, Y.; Wang, H.; Kaner, R. B. 3D Freeze-Casting of Cellular Graphene Films for Ultrahigh-Power-Density Supercapacitors. *Advanced Materials* **2016**, *28* (31), 6719–6726. https://doi.org/10.1002/adma.201506157.

(2) Wang, L. J.; El-Kady, M. F.; Dubin, S.; Hwang, J. Y.; Shao, Y.; Marsh, K.; McVerry, B.; Kowal, M. D.; Mousavi, M. F.; Kaner, R. B. Flash Converted Graphene for Ultra-High Power Supercapacitors. *Adv Energy Mater* **2015**, *5* (18), 1500786. https://doi.org/10.1002/aenm.201500786.

(3) Liu, B.-T.; Shi, X.-M.; Lang, X.-Y.; Gu, L.; Wen, Z.; Zhao, M.; Jiang, Q. Extraordinary Pseudocapacitive Energy Storage Triggered by Phase Transformation in Hierarchical Vanadium Oxides. *Nat Commun* **2018**, *9* (1), 1375. https://doi.org/10.1038/s41467-018-03700-3.

(4) Wu, Y.; Gao, G.; Wu, G. Self-Assembled Three-Dimensional Hierarchical Porous V 2 O 5 /Graphene Hybrid Aerogels for Supercapacitors with High Energy Density and Long Cycle Life. *J Mater Chem A Mater* **2015**, *3* (5), 1828–1832. https://doi.org/10.1039/C4TA05537C.

(5) Perera, S. D.; Patel, B.; Nijem, N.; Roodenko, K.; Seitz, O.; Ferraris, J. P.; Chabal, Y. J.; Balkus, K. J. Vanadium Oxide Nanowire-Carbon Nanotube Binder-Free Flexible Electrodes for Supercapacitors. *Adv Energy Mater* **2011**, *1* (5), 936–945. https://doi.org/10.1002/aenm.201100221.

(6) Perera, S. D.; Rudolph, M.; Mariano, R. G.; Nijem, N.; Ferraris, J. P.; Chabal, Y. J.; Balkus, K. J. Manganese Oxide Nanorod–Graphene/Vanadium Oxide Nanowire–Graphene Binder-Free Paper Electrodes for Metal Oxide Hybrid Supercapacitors. *Nano Energy* **2013**, *2* (5), 966–975. https://doi.org/10.1016/j.nanoen.2013.03.018.

(7) Pang, Q.; Sun, C.; Yu, Y.; Zhao, K.; Zhang, Z.; Voyles, P. M.; Chen, G.; Wei, Y.; Wang, X. H2V3O8 Nanowire/Graphene Electrodes for Aqueous Rechargeable Zinc Ion Batteries with High Rate Capability and Large Capacity. *Adv Energy Mater* **2018**, *8* (19), 1800144. https://doi.org/10.1002/aenm.201800144.

(8) Lu, X.; Yu, M.; Zhai, T.; Wang, G.; Xie, S.; Liu, T.; Liang, C.; Tong, Y.; Li, Y. High Energy Density Asymmetric Quasi-Solid-State Supercapacitor Based on Porous Vanadium Nitride Nanowire Anode. *Nano Lett* **2013**, *13* (6), 2628–2633. https://doi.org/10.1021/nl400760a.

(9) Chen, M.; Zhang, Y.; Liu, Y.; Wang, Q.; Zheng, J.; Meng, C. Three-Dimensional Network of Vanadium Oxyhydroxide Nanowires Hybridize with Carbonaceous Materials with Enhanced Electrochemical Performance for Supercapacitor. *ACS Appl Energy Mater* **2018**, *1* (10), acsaem.8b01109. https://doi.org/10.1021/acsaem.8b01109.

(10) Chang, X.; El-Kady, M. F.; Huang, A.; Lin, C.; Aguilar, S.; Anderson, M.; Zhu, J. Z. J.; Kaner, R. B. 3D Graphene Network with Covalently Grafted Aniline Tetramer for Ultralong-Life Supercapacitors. *Adv Funct Mater* **2021**, *31* (32), 2102397. https://doi.org/10.1002/adfm.202102397.